Investigation of Molecule Adsorption on *h*-BN Nanomesh: Water and Phthalocyanine

---

Dissertation

zur

Erlangung der naturwissenschaftlichen Doktorwürde
(Dr. sc. nat.)

vorgelegt der

Mathematisch-naturwissenschaftlichen Fakultät

der

Universität Zürich

von

Yun Ding

aus

China

Promotionskomitee

Prof. Dr. Jürg Hutter (Vorsitz und Leitung)
Prof. Dr. Thomas Greber

Zürich, 2012

Abstract

The hexagonal boron nitride nanomesh is a periodic structure with a corrugated BN layer on a Rh(111) surface. Due to the lattice mismatch, a 2 nm diameter depression is formed and called the pore of the nanomesh, while the other higher region connecting the pores are called the wire. By means of density functional theory, the structural and electronic properties of the nanomesh are studied, and our model could reproduce the characteristic pore and wire regions, and also other electronic properties, like STM images and work function modulations.

Further, the adsorption behavior of water and phthalocyanine are investigated intensively to help better understand the experimental findings and the trapping effect of the nanomesh. In experiment, when small amounts of water are dosed to the bare nanomesh, three protrusion images could be obtained in nanomesh pores, with a distance around 4.6 Å between each protrusion. Our studies indicate that the most probable structure would be cyclic water hexamer, as the water molecules with the H pointing towards the vacuum are invisible to the STM tip.

By increasing the water dosage, so called nano-ice clusters fill the entire pores and the STM scan across the pore indicates a bilayer structure with the distance between molecules in the same layer of 4.6 Å. Based on experimental findings, possible arrangements of water molecules are proposed and are first studied on a flat BN surface. However, the most probable structure could not be distinguished simply from the binding energy. By minimizing the in plane dipole moment, the most probable structure is suggested, in which all six water molecules in one hexagon have completely different orientations and mirror symmetry. Moreover, the STM image of 38 water molecules from such structure adsorbed in the pore of the full nanomesh is consistent with the experimental one.

When organic molecules, e.g. hydrogen phthalocyanine and copper phthalocyanine are adsorbed, they show an off-center adsorption pattern along the [21] direction. Different adsorption sites are sampled with the help of DFT and the energy contribution indicates that the van der Waals dispersion correction is highly important for this kind of weak interaction system.

Zusammenfassung

Gitterstrukturen auf der Nanometerskala gebildet von hexagonalen Bornitrid lagen auf Rh(111) Oberflächen werden 'Nanomesh' genannt. Die Unterschiede in den Gittervektoren der beiden Materialien führt zu 2 nm grossen Vertiefungen, die sogenante Pore des Nanomeshes, und zu höherliegenden Regionen zwischen den Poren. Mittels Dichtefunktionaltheorie wurden die Struktur und elektronischen Eigenschaften des Nanomeshes studiert. Unser Modell ist in der Lage die charakteristischen Poren sowie andere elektronischen Eigenschaften wie STM Bilder und Modulationen der Austrittsarbeit korrekt zu reproduzieren.

Die Adsorption von Wasser- und Phthalocyaninmolekülen wurden intensiv untersucht um ein besseres Verständnis experimenteller Resultate zum Templateffekt des Nanomeshes zu erreichen. Werden kleine Mengen von Wasser auf das Nanomesh aufgebracht, so erscheinen drei helle Punkte auf den STM Bildern. Die Punkte befinden sich ca. 4.6 Åauseinander. Unsere Untersuchungen weisen darauf hin, dass es sich dabei um zyklische Strukturen aus sechs Wassermolekülen handelt. Drei der Wassermoleküle, deren freies Wasserstoffatom vom Nanomesh wegdeutet, ist dabei im STM Bild nicht sichtbar.

Wird die Wasserdosierung erhöht, bilden sich Eiscluster die die ganze Pore ausfüllen. STM Untersuchungen weisen darauf hin, dass es sich dabei um Doppellagenstrukturen handelt, wobei die Distanz zwischen Molekülen in einer Lage 4.6 Åbeträgt. Basierend auf diesen Experimenten wurden verschiedene Strukturen vorgeschlagen und zuerst auf einer freistehenden BN Lage untersucht. Es war allerdings nicht möglich die verschiedenen Modelle anhand ihrer Bindungsenergie zu unterscheiden. Durch die Minimierung des Dipolmomentes parallel zur Ebene konnte eine mögliche Struktur gefunden werden, die keine Symmetrien aufweist und deren Anordnung der Wassermoleküle innerhalb der Sechsringe nicht mehr regelmässig ist. Die so vorgeschlagene Struktur von 38 Wassermolekülen führt zu berechneten STM Bildern die mit den experimentellen übereinstimmen.

Organische Moleküle adsorbiert auf dem Nanomesh richten sich entlang der [21] Richtung aus. Verschiedene Adsorptionsplätze wurden mit der Hilfe der Dichtefunktionaltheorie untersucht und es konnte gezeigt werden, dass die schwache Bindung zum Substrat von van der Waals Kräften dominiert wird.

Acknowledgement

First of all, I sincerely thank Professor Jürg Hutter for giving me this chance to work in his group. He has been helping me, guiding me and supervising me for the past four years.

I would also like to thank my colleague Dr Marcella Iannuzzi as we work closely on my PhD project. Moreover she's always there offering help, revising my manuscripts and preparing the code for my calculations.

Many thanks to our experimental collaborators, Dr. Haifeng Ma, Professor Thomas Greber and Professor Jürg Osterwalder from Physics Institute. They work really hard on the water and nano-ice systems and we had fruitful discussions and results. Also thanks go to Dr. Oliver Gröning, Dr. Roland Widmer, and Dr. Thomas Dienel from EPMA for the experimental support on the phthalocyanine system.

I would also like to thank Dr. Ari P Seitsonen, Dr. Jaime Gomez-Diaz and other group members for their help on my project and providing such a wonderful atmosphere in the group. It's really a pleasure to work here. We lost Jaime in a tragic mountain accident, our deepest condolences go to his family and friends.

Thanks to graduate school of chemical and molecular sciences, I won't be here without this program. They always organize retreat and other activities, besides, also provide financial supports for members.

Finally, specially thanks to my parents and all the friends for their continuous supports during the whole time.

Publication

1. H. F. Ma, T. Brugger, S. Berner, Y. Ding, M. Iannuzzi, J. Hutter, J. Osterwalder and T. Greber, Nano-ice on Boron Nitride Nanomesh: Accessing Proton Disorder, ChemPhysChem 11, 399-403 (2010)

2. Y. Ding, M. Iannuzzi and J. Hutter, Investigation of h-BN/Rh(111) Nanomesh Interacting with Water and Atomic Hydrogen, Chimia 65, 256-259 (2011)

3. Y. Ding, I. Marcella and J. Hutter, Investigation of Boron Nitride Nanomesh Interacting with Water, Journal of Physical Chemistry C 115, 13685-13692 (2011)

4. Y. Ding, I. Marcella and J. Hutter, Nano-ice Models for the Water Aggregates Observed on the *h*-BN/Rh(111) Nanomesh, Submitted

5. H. F. Ma, Y. Ding, M. Iannuzzi, T. Brugger, S. Berner, J. Hutter, J. Osterwalder, T. Greber, Chiral Distortion of Confined Ice Hexamers, Submitted

Contents

Chapter 1

Introduction

Boron nitride (BN) is an isoelectronic structure compared to carbon pairs, which presents similarity in both structures and properties. Similar to carbon nanostructures, like nanotubes[1, 2, 3, 4] formed by the hexagonal carbon lattice and C_{60}[5], analogous BN nanostructures, such as multi-wall[6] or single-wall[7] nanotubes and BN concentric-shell cluster[8] are also reported. With the support of transition metal surfaces, single hexagonal boron nitride (h-BN) layer could also be achieved [9, 10, 11, 12, 13, 14, 15, 16, 17] by thermal decomposition of borazine ($B_3N_3H_6$) at high temperature. Due to the lattice mismatch between the h-BN and metal surface, corrugated BN lattice could be observed and is most pronounced on Rh(111)[11] and Ru(0001) surface[13]. Wave-like nanostructure is also observed when h-BN is formed on Fe(110) surface[18]. In the thesis, we mainly focus on the h-BN epitaxially growing on Rh(111) surface. Where N atoms are located on top of Rh atoms, stronger electronic interaction is possible and the BN overlayer tends to stay closer to the metal, at about 2.2 Å[19]. Elsewhere, the interaction is weak and the overlayer remain farther, at about 3.1 Å from the substrate[19]. The BN height variation creates depressions of 2 nm of diameter[11, 20], which are called pores, while the weakly bound regions form a connected network, called wire. The resulting superstructure has a periodicity of 3.2 nm and is called nanomesh (NM).

In h-BN/Rh(111) nanomesh, pores are equally spaced and separated. Molecules like C_{60} have been used to decorate the nanomesh surface [11], and they tend to be trapped in the pore of the nanomesh. In order to study the trapping effect of the pore together with the self-assembly of molecules with the help of the nanomesh template, different materials, like liquid water[21, 22], hydrogen phthalocyanine (H_2Pc) and copper phthalocyanine (CuPc)[23] have been used to deposit onto the bare nanomesh. The studies presented in this thesis aim at a better understanding of the interaction of molecules such

as water, H_2Pc and CuPc with the nanomesh. In particular, the role of the nanomesh in determine the adsorption site and the orientation of the molecule is investigated in detail, and possible effects on self-assembly patterns are considered. The systems reported in this thesis have been also subject to experimental studies based on scanning tunneling microscopy (STM) and other surface analysis techniques[21, 22, 23]. In the case of water adsorbed on the nanomesh, it has been observed that the resulting structures depend on the amount of water deposited on the substrate. More precisely, with little water deposition, one protrusion or three protrusions could be seen in the nanomesh pore[22]. Density functional theory (DFT) calculations, indicate that the three protrusions are most probably formed by cyclic water hexamer[19, 24]. By increasing the water dosage, all the pores could be filled with bilayer nano-ice clusters[21]. We could also suggest the most probable structure for the nano-ice cluster based on different water lattice models and their correspondent dipole moment. For the case of H_2Pc and CuPc, we refer to experimental work[23] (not yet published) showing that they prefer the off-center adsorption site along the [21] direction of the nanomesh. DFT calculations could give pictures consistent with experiment. The essential for this kind of system is to use efficient DFT tools due to the demanding computational cost, and also the van der Waals (vdW) correction is necessary because of the weak interaction between the adsorbate and the substrate.

The thesis is organized in eight chapters. After this brief introduction, chapter 2 reports some more detail on the experimental work on the systems addressed in this thesis, i.e, bare *h*-BN/Rh(111), water on *h*-BN/Rh(111), nano-ice on *h*-BN/Rh(111), and finally H_2Pc and CuPc on it. Chapter 3 is dedicated to the description of the computational methods employed for the investigation of these systems. The 4th chapter describes the interaction of water with free-standing BN and also graphene, which is fundamental to understand the difference when the substrate is *h*-BN/Rh(111) nanomesh. The last three chapters contain the detailed descriptions of the investigated molecule/nanomesh interfaces. In this part of the work, connection to the experimental results is constantly provided. The final chapter reports conclusions and outlook.

Chapter 2

Hexagonal Boron Nitride Nanomesh

h-BN is similar to graphite in bonding and structure. Each boron atom is bound to three nitrogen atoms and vice versa. Moreover, each BN pair has the same number of electrons as the carbon pair and three BN pairs form the hexagonal BN ring. In experiments, it has been found that large supercell structures of *h*-BN on transition metals could be formed after decomposition of borazine ($B_3N_3H_6$) to a clean metal surface at high temperature in ultra-high vacuum. In the superstructure, a single layer BN mesh is weakly bound to the metal surface and the vertical corrugation is related to the extend of the lattice mismatch between the *h*-BN and the metal surface. Successful formations of the superstructure have already been reported for Cu(111)[10], Pt(111)[12, 14], Pd(111)[25], Pd(110)[26], Ni(111)[9, 27], Ru(0001)[28, 17] and Rh(111)[11, 16] surfaces. Among these, only the *h*-BN/Ni(111) and *h*-BN/Cu(111) show 1×1 commensurate structures. In this chapter, a summary of the most important features of *h*-BN/Rh(111) nanomesh is reported, as resulting from previous experimental and theoretical work. Besides, the experiments on water/*h*-BN/Rh(111) and Pc/*h*-BN/Rh(111) which inspire our theoretical investigations are also briefly described.

2.1 *h*-BN/Rh(111) nanomesh

The *h*-BN/Rh(111) nanomesh is first reported by the scientists of Physics Institute at the University of Zurich (UZH) in 2004[11]. They noticed that a highly regular structure is formed by self-assembly after decomposition of borazine ($B_3N_3H_6$) to a clean Rh(111) surface at high temperature under the ultrahigh vacuum condition. Low-energy electron diffraction (LEED) [11]

experiment revealed that the periodicity of the supercell is around 3.2 Å, which corresponds to 13 × 13 BN unit cells on 12 × 12 Rh units. The periodicity of the superstructure is also confirmed by surface X-ray diffraction experiments[20]. The first interpretation of these results proposed a double layer BN with holes, where the inner BN layer lies flatly above the metal, at the same time, the outer layer follows the inner one and forms a corrugated sheet. Only later, with the help of DFT calculations, it was concluded that the superstructure was formed by a single, corrugated BN layer[29]. Further low-temperature STM experiments [20] confirmed this model. The single layer of hexagonal BN shows a regular distribution of 2 nm diameter pores, separated by regions where the BN layer is less tightly bound to Rh(111) and

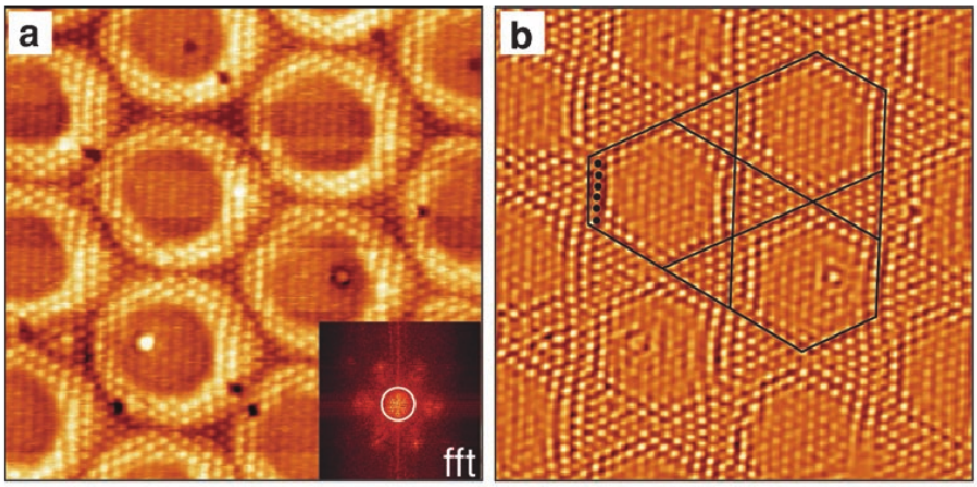

Figure 2.1: **a**. Low-temperature STM image of *h*-BN/Rh(111) nanomesh at 77 K and only N atoms are imaged. **b**. Image of **a** after filtrating the Fourier coefficients in order to remove the 3.2 nm periodicity and emphasize the corrugation. The hexagon defines the shape of the rim, while the triangle regions belong to the wire. The Figure is taken from ref. [20]

called the "wires" (see in Figure 2.1). Previous DFT studies[29, 30] have also shown that attractions only exist between B and Rh atoms, while there are only repulsions between N and Rh atoms, which is weakest when N is near the top site (i.e. above a Rh atom of the outermost layer). Hence, the BN surface is slightly buckled with B atoms a little bit closer to the Rh(111) surface than N atoms. However, our studies shown that effective binding to the metal turns out to be possible only when N sits approximately in a top-site, while three nearest B atoms occupy either a face-centered cubic (fcc) site (i.e., sitting on top of a Rh atom of the third layer) or a hexagonal close-packed

(hcp) site (i.e., sitting on top of a Rh atom of the second layer). We call this arrangements of BN on Rh (N-top, B-fcc) registry, and (N-top, B-hcp) registry. In all other possible registries, the BN overlayer is not chemically binding to the metallic substrate, and the dominant interactions are dispersion forces or vdW contributions. Since these forces are weaker, in these loosely interacting regions, the BN overlayer tends to stay at larger distances from the metal. Due to the lattice mismatch between BN and Rh, only a small portion of BN layer could satisfy the most stable N-top, B-(fcc,hcp) adsorption site, which corresponds to the pore of the nanomesh. A clear suggestion of the different type of N-Rh interactions is the characteristic σ band splitting observed by normal emission ultraviolet photoelectron spectroscopy (UPS) experiments[11]. In particular, in the spectrum obtained from BN on Rh(111), the splitting of 1 eV is attributed to the two types of N atoms, those interacting strongly with the metal and those forming the wires, whose electronic structure is barely affected by the presence of the metal. On the contrary, the spectrum obtained from BN on Ni(111) does not present any splitting. Indeed, DFT calculations suggest that all N atoms are on top of Ni atoms[31], in other words, all N atoms are in the same environment. The local density of states (LDOS) calculations for the N atoms in different regions of the h-BN/Rh(111) nanomesh show a clear shift of the peaks[29, 30] and this is consistent with the σ band splitting observed in the experiments.

2.2 Molecule Trapping

The resulting mesh structure turns out to be very stable in gas phase[32], and clear mesh structures were also shown in the experimental STM images after immersing the nanomesh sample into water[20], and 0.1 M $HClO_4$[33] separately, which suggests the nanomesh could also be stable in solvent environment. Moreover, it has been observed in experiments that C_{60}[11] and Naphthalocycanine[20] could be deposited and stabilized in the pore, thus making the nanomesh an interesting candidate as template for self-assembly of ordered and distant two dimensional molecular lattices. It has also been observed that the local work function above the nanomesh changes following the corrugation of the BN overlayer. A few angstroms above the atoms forming the pore of the nanomesh, the work function is about 310 meV lower than above the atoms of the wire[34]. This modulation is expected to have an influence on the behavior of adsorbed molecules. In this work, we consider in particular the interaction of the nanomesh with water and Pc molecule.

2.2.1 Small Water Cluster

In the experiments performed by the scientists in Physics Institute at UZH, different amount of water molecules have been dosed to the bare nanomesh. Because of the corrugation of the nanomesh, water molecules could be trapped in the 2 nm pores and show a two dimensional structure. In recent STM experiments[22], performed after dosing 0.001 Langmuir (L) water to the empty boron nitride nanomesh at 34K, single and triple protrusions, appearing as bright spots, could be observed as predominant species in some of the pores (shown in Figure 2.2). These images seem to be associated to trapped water molecules, most probably organized in small two dimensional clusters. Several hints indicate that the number of water molecules forming these aggregates exceeds the number of visible protrusions. Single protrusions show a diffusion behavior; they may split into double protrusions and back into single protrusions, which indicates that more than one water molecule is present in the pore. Moreover, the analysis of the triple protrusion images revealed that the average distance between these spots is around 4.6 Å, which is close to the distance of second neighbor water molecules in ice clus-

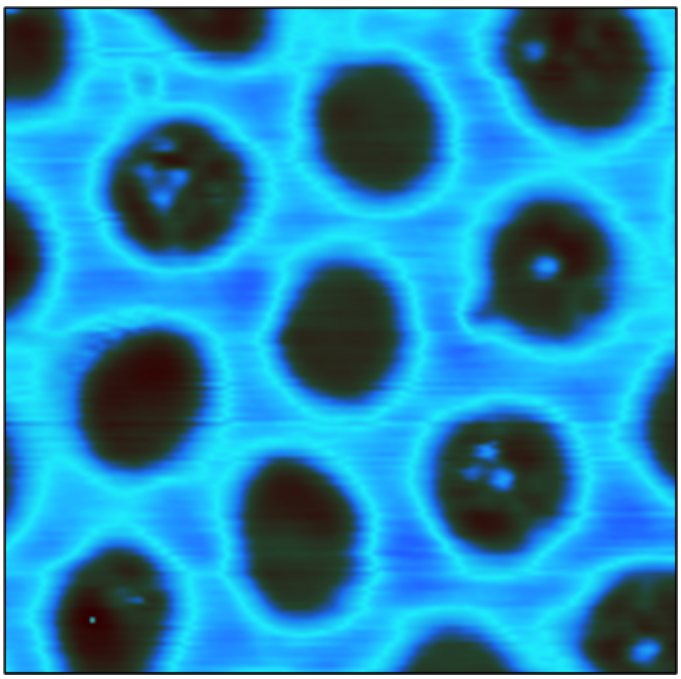

Figure 2.2: STM image of the *h*-BN/Rh(111) nanomesh after deposition of 0.001 L water at 34 K. Single or Triple protrusions could be observed in some of the pores[22]. The Figure is courtesy of Dr. Haifeng Ma.

ters. However, the resolution of the collected images does not allow for clear identification of the structures and of the dynamics (aggregation processes, diffusivity) of these water clusters. The experimental evidence tells us that water clusters can be adsorbed in the pore, and they preferentially organize themselves in the structure producing the three protrusions. On the other hand, the fact that on the wire it is much less probable to resolve clear spots showing the presence of adsorbed water molecules, seems to indicate that here the water aggregates are not stable or can easily move and, therefore, cannot be detected by the STM.

2.2.2 Nano-ice cluster

Besides the small aggregates described above, experiments[21] also show that by increasing the amount of water deposition to about 2 L on the bare nanomesh at 52K, larger aggregates called nano-ice clusters are formed and fill the entire pore. As in the previous case, STM cannot resolve any ordered structure of adsorbates on the wire (as show in Figure 2.3). The STM height profile of the nanomesh recorded across the pore after the deposition of 1 L water (Figure 2.3c) compared to the same profile taken from the bare nanomesh (Figure 2.3b) indicates that the aggregates form a honeycomb like lattice. The molecules appear as distributed over two sub-lattices with a height difference of $\sim$15 pm. The lateral distance between the water molecules in the same layer is about 4.6 Å, which once more corresponds to the second neighbor distance in ice clusters. On the other hand, the height profile recorded around the pore (hexagonal line in Figure 2.3b and c) didn't give any evidence indicating the existence of the ordered water structure on the wire. However, the height fluctuations of the STM tip are much larger on the wetted than on the bare nanomesh, suggesting the presence of a low density water phase on the wire, with fast moving molecules. Similar two dimensional water layers are also reported on graphene/Pt(111) substrate[35], and in both cases, the substrates (h-BN and graphene) are sp^2 hybridized.

For the above mentioned two different preparations of the water deposition, different nano-ice orientations rotated by 11$\pm$3° and -24$\pm$3° with respect to the direction of two nearby pores[21] are observed and this indicates that the interaction between the ice clusters are stronger than the binding interaction with the nanomesh substrate (lock-in energy). The average number of protrusions for the top layer water molecules after analysis of 32 pores was found to be 20$\pm$5 per pore[21]. As two layers are involved in the formation of the nano-ice structure, around 40 water molecules are expected in each pore.

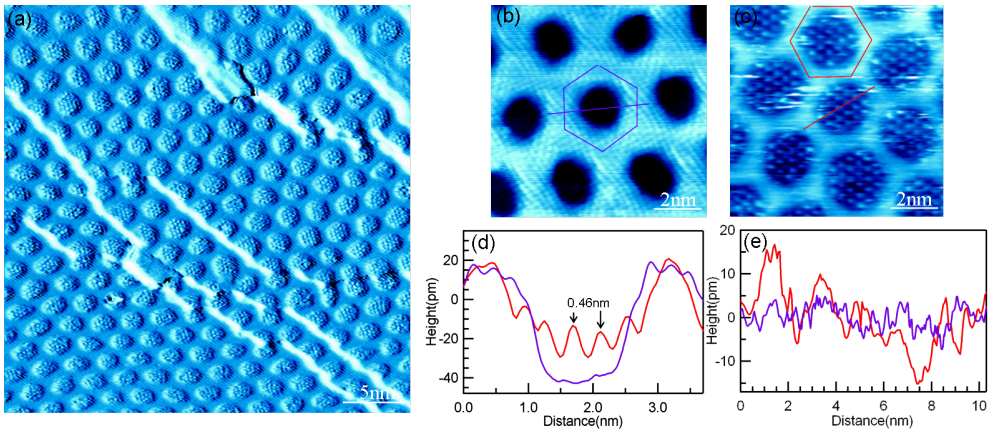

Figure 2.3: (**a**). STM image of 2 L water molecules adsorbed on the nanomesh at 52 K. (**b**). Bare Nanomesh.(**c**). STM image of 1 L water deposition at 52 K. (**d**,**e**). Height comparison across (**d**) and around (**e**) the hole. Blue line is for the bare nanomesh (**b**) and red line is for the nanomesh after 1 L water deposition (**c**). The Figure is courtesy of Dr. Haifeng Ma.

2.2.3 Phthalocyanine

Pc molecule is a large conjugated molecule similar to porphyrin. Transition metal ions, like copper, nickel and iron ions, or simply two hydrogen atoms could be hosted in the molecular center. The diameter of Pc molecule is around 1.5 nm, which fits well in the pore of the nanomesh (2 nm diameter). The low-temperature STM experiments performed by the surface scientists of EMPA show that both H_2Pc and CuPc can adsorb in the nanomesh pore, with similar adsorption pattern. The imaging of such systems turns out to be quite difficult due to the high mobility of the molecules. For CuPc stable images are obtained only at 5 K. The lighter H_2Pc is more mobile and even harder to image. In both cases, the preferred adsorption site is along the [21] direction of the nanomesh, with the center of the molecule shifted by $\sim$5 Å with respect to the center of the pore (See in Figure 2.4). Another STM image for CuPc at 77 K shows two molecules in the pore at the same time, however, actually there's only one CuPc adsorbed and the double-cross image comes from the movement of the molecule in these two adsorption site and it looks like the molecule only moves along the [21] direction without any rotation. Previous experiments[36, 37, 38] involving metal Pc (MPc) or H_2Pc adsorbed on transition metal surface also indicate that MPc molecules tend to adsorb on the surface with one of its molecular axis along the close packing direction of the substrate. In this case, the other molecular axis is consistent with the [21] adsorption of CuPc on nanomesh surface. DFT

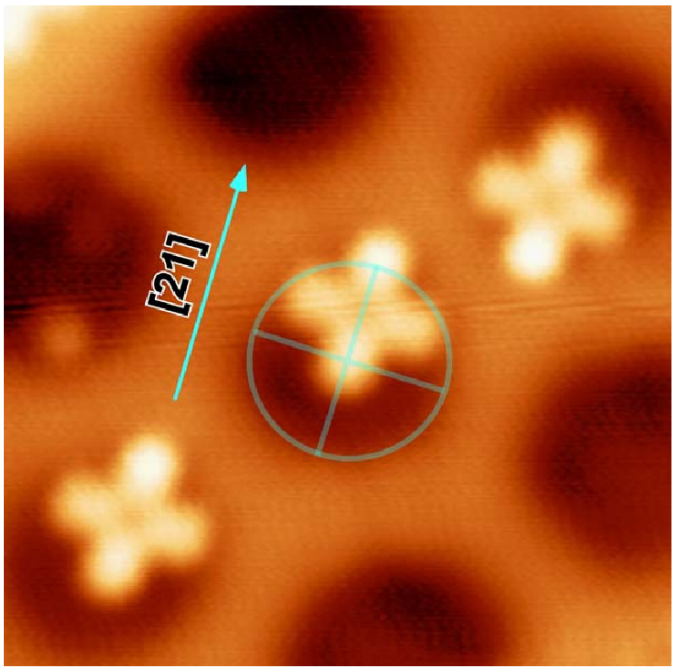

Figure 2.4: STM image of CuPc adsorbed along the [21] direction of the nanomesh imaged at 5 K. The Figure is courtesy of Dr. Oliver Gröning.

calculations [39] of CoPc adsorbed on Cu(111) surface also indicate that the two isoindole rings perpendicular to the close packing direction of the metal substrate interact stronger with Cu(111) surface compared to the other two isoindole rings. So it's quite possible that the specific orientation direction of CuPc or H_2Pc molecule on nanomesh is induced by the symmetry of the substrate.

Chapter 3

Theory

3.1 Schrödinger Equation

In quantum mechanics, the most important thing is to solve the Schrödinger equation. For the time-dependent Schrödinger equation, it has the form:

$$i\hbar\frac{\partial\Psi}{\partial t} = \hat{H}\Psi \tag{3.1}$$

where $\hat{H}$ is the Hamilton operator of the system. To solve this equation more conveniently, we could separate the equation into two parts: one is related to the time evolution, $exp(\frac{E}{i\hbar}t)$, and the other part is a stationary part, only related to the coordinates, $\psi(\mathbf{r})$. So the wave function $\Psi(\mathbf{r},t)$ would be written in this way:

$$\Psi(\mathbf{r},t) = \psi(\mathbf{r})exp(\frac{E}{i\hbar}t) \tag{3.2}$$

inserting it into the Schrödinger equation (3.1), we could get:

$$\hat{H}\psi = E\psi \tag{3.3}$$

and this is the time-independent Schrödinger equation, where E is the energy of the stationary state. For a system containing N nuclei and m electrons, the positions of the nuclei are in the coordinates set of $\{\mathbf{R}_A\}$ with mass of $\{\mathrm{M}_A\}$ and charge $\{Z_A e\}$, while the position of the electrons are in the coordinates set of $\{\mathbf{r}_i\}$ with the same mass m and charge $-e$. The Hamilton operator $\hat{H}$ is:

$$\hat{H} = \hat{T}_N + \hat{T}_{el} + \hat{V}_{Ne} + \hat{V}_{ee} + \hat{V}_{NN} \tag{3.4}$$

where $\hat{T}_N$ and $\hat{T}_{el}$ is the kinetic energy of nuclei and electrons separately, $\hat{V}_{Ne}$, $\hat{V}_{ee}$ and $\hat{V}_{NN}$ are the Coulomb potential energy for the interactions between

nuclei and electron, electron themselves and nuclei themselves. For these five terms, they have the following forms:

$$\hat{T}_N = -\sum_A^N \frac{\hbar^2}{2M_A} \nabla_A^2 \tag{3.5}$$

$$\hat{T}_{el} = -\frac{\hbar^2}{2m} \sum_i^m \nabla_i^2 \tag{3.6}$$

$$\hat{V}_{Ne}(\mathbf{r}, \mathbf{R}) = -\sum_A^N \sum_i^m Z_A \frac{e^2}{|\mathbf{R}_A - \mathbf{r}_i|} \tag{3.7}$$

$$\hat{V}_{ee}(\mathbf{r}) = \sum_{i<j}^m \frac{e^2}{|\mathbf{r}_i - \mathbf{r}_j|} \tag{3.8}$$

$$\hat{V}_{NN}(\mathbf{R}) = \sum_{A<B}^N Z_A Z_B \frac{e^2}{|\mathbf{R}_A - \mathbf{R}_B|} \tag{3.9}$$

3.2 Born-Oppenheimer Approximation

Since the electrons are much lighter and hence move much faster than the nuclei, instead of solving the time-independent Schrödinger equation for the electrons and nuclei at the same time, we could consider the nuclei position $\{\mathbf{R}\}$ to be fixed, therfore, we only have to solve the Schrödinger equation for the electrons in the static electric field of the nuclei.
The electronic Schrödinger equation is:

$$\hat{H}_{el}(\mathbf{r}; \mathbf{R}) \Psi_{el}(\mathbf{r}; \mathbf{R}) = E_{el}(\mathbf{R}) \Psi_{el}(\mathbf{r}; \mathbf{R}) \tag{3.10}$$

and the Hamilton

$$\hat{H}_{el}(\mathbf{r}; \mathbf{R}) = \hat{T}_{el}(\mathbf{r}) + \hat{V}_{Ne}(\mathbf{r}, \mathbf{R}) + \hat{V}_{ee}(\mathbf{r}) \tag{3.11}$$

Here, the kinetic operator for the nuclei $\hat{H}_N(\mathbf{R})$ is considered to be 0, and the potential energy term for the nuclei $\hat{V}_{NN}(\mathbf{R})$ is neglected as it does not work on the electrons. Thanks to Born-Oppenheimer Approximation, now we only need to focus on solving the electronic Schröndinger equation.

3.3 Density Functional Theory

Density functional theory (DFT) is one of the most popular methods in treating electronic many-body systems in quantum mechanical way within the Born-Oppenheimer approximation, especially for large molecules and condensed phase systems due to its relatively low computational cost and high accuracy. Instead of solving Schrödinger equations directly in order to get the wavefunctions, P. Hohenberg and W. Kohn proved that for nondegenerate ground state, the ground state properties (i.e. wavefunctions, ground state energy, etc.) are uniquely determined by electron density $n(\mathbf{r})$[40].

3.3.1 Hohenberg-Kohn Theorems

Theorem 1: The external potential $v_{ext}(\mathbf{r})$ is uniquely correspondent to the electron density $n(\mathbf{r})$, apart from a trivial constant.

The Hamiltonian and the total energy have the respective form

$$\hat{H} = \hat{T}_{el} + \hat{V}_{ext} + \hat{V}_{ee}, \tag{3.12}$$

$$E[n(\mathbf{r})] =< \Psi[n(\mathbf{r})]|\hat{H}|\Psi[n(\mathbf{r})] > . \tag{3.13}$$

Hence, for a known electron density $n(\mathbf{r})$, the external potential which comes from the nuclei is determined, thus the Hamiltonian of the system is fixed. In this way, the total energy and other properties are also uniquely determined.

Theorem 2: The ground state energy is minimized by ground state electron density n_0, i.e. $E(n) \geq E(n_0)$.

The total energy of the N-electron many-body system in atomic units is

$$E = \int v_{ext}(\mathbf{r})n(\mathbf{r})d\mathbf{r} + F[n(\mathbf{r})], \tag{3.14}$$

where $\int v_{ext}(\mathbf{r})n(\mathbf{r})d\mathbf{r}$ is the interaction of the external potential acting on the electrons, and $F[n(\mathbf{r})]$ is the sum of the kinetic energy $T[n(\mathbf{r})]$ and the electron-electron interaction energy $V_{ee}[n(\mathbf{r})]$.

So for $F[n(\mathbf{r})]$, we could write down the classical Coulomb repulsion energy $J[n(\mathbf{r})]$.

$$F[n(\mathbf{r})] = J[n(\mathbf{r})] + G[n(\mathbf{r})] \tag{3.15}$$

Here, both $F[n(\mathbf{r})]$ and $G[n(\mathbf{r})]$ are universal functionals of the electron density. For $G[n(\mathbf{r})]$, it includes not only the kinetic energy, but also the nonclassical correction to electron repulsions.

$$J[n(\mathbf{r})] = \frac{1}{2}\iint \frac{n(\mathbf{r})n(\mathbf{r}')}{|\mathbf{r}-\mathbf{r}'|}d\mathbf{r}d\mathbf{r}' \tag{3.16}$$

$$E = \int v_{ext}(\mathbf{r})n(\mathbf{r})d\mathbf{r} + \frac{1}{2}\iint \frac{n(\mathbf{r})n(\mathbf{r}')}{|\mathbf{r}-\mathbf{r}'|}d\mathbf{r}d\mathbf{r}' + G[n(\mathbf{r})]. \tag{3.17}$$

According to the variational principle, the ground state is the state with the lowest energy E_0, thus in DFT, the ground state could be obtained by minimizing the energy of the trial potential n'.

$$E_0 = \mathrm{Min}_{n'}\{E(n')\} \tag{3.18}$$

Although the Hohenberg-Kohn theorems proved that the Schrödinger equation could be solved from a different way, in other words, from the electron density, it's still not feasible to carry out calculations in practice as no explicit formula for $G(n)$ is available. Efforts have been made for approximations of $G(n)$, but still, the accuracy is not good enough. Almost after one year, W. Kohn and L. J. Sham further improved DFT by proposing a fictitious non-interacting electron system[41], and after that, DFT calculations could be performed straightforward.

3.3.2 Kohn-Sham Theory

As we have already seen in equation 3.17, the problematic part here for calculation is the functional $G[n(\mathbf{r})]$ of electron density $n(\mathbf{r})$, which contains both the kinetic interaction and non-classical correction to electron-electron repulsions. In Kohn-Sham theory, they introduced a non-interacting reference system with the same number of electrons and same density, moreover, the kinetic energy of the real system is expressed based on the non-interacting system, while the exchange and correlation effects of the interacting system are all considered in E_{xc}.

$$E = T_s[n(\mathbf{r})] + J[n(\mathbf{r})] + \int v_{ext}(\mathbf{r})n(\mathbf{r})d\mathbf{r} + E_{xc}[n(\mathbf{r})] \tag{3.19}$$

$$E_{xc}[n(\mathbf{r})] = \{V_{ee}[n(\mathbf{r})] - J[n(\mathbf{r})]\} + \{T[n(\mathbf{r})] - T_s[n(\mathbf{r})]\} \tag{3.20}$$

In which, the T and T_s are the kinetic energy of interacting and non-interacting system respectively, and V_{ee} is the interaction between the electrons. According to the variational principle, for the ground state,

$$\delta E[n(\mathbf{r})] = 0. \tag{3.21}$$

And as the number of electrons in the system keeps constant, we have

$$\int n(\mathbf{r})d\mathbf{r} = N. \tag{3.22}$$

Thus, we could introduce the Lagrange multiplier, to solve equation 3.21 at the constraint condition of equation 3.22, it would be equivalent to solve the following equation:

$$\delta(E[n(\mathbf{r})] - \mu(\int n(\mathbf{r})d\mathbf{r} - N)) = 0 \tag{3.23}$$

So, we got the Euler-Lagrange equation

$$\mu = v_{ext}(\mathbf{r}) + v_J(\mathbf{r}) + v_{xc}(\mathbf{r}) + \frac{\delta T_s}{\delta n(\mathbf{r})}. \tag{3.24}$$

μ is the chemical potential of the system. And

$$v_J(r) = \frac{\delta J[n(\mathbf{r})]}{\delta n(\mathbf{r})} = \int \frac{n(\mathbf{r}')}{|\mathbf{r} - \mathbf{r}'|} d\mathbf{r}', \tag{3.25}$$

$$v_{xc}(\mathbf{r}) = \frac{\delta E_{xc}}{\delta n(\mathbf{r})}. \tag{3.26}$$

We could consider the sum of these potentials as an effective Kohn-Sham potential, thus the many-body problem could be treated separately as one-electron problems, and we only need to solve the one-electron Schrödinger equation respectively.

$$v_{eff}^{KS}(\mathbf{r}) = v_{ext}(\mathbf{r}) + v_J(\mathbf{r}) + v_{xc}(\mathbf{r}) \tag{3.27}$$

$$\left\{ -\frac{1}{2} \bigtriangledown^2 + v_{eff}^{KS} \right\} \psi_i(\mathbf{r}) = \epsilon_i(\mathbf{r}) \psi_i(\mathbf{r}) \tag{3.28}$$

The electron density

$$n(\mathbf{r}) = \sum_i |\psi_i^2(\mathbf{r})| \tag{3.29}$$

Also the energy is given by

$$E = \sum_i^N \epsilon_i - J + E_{xc} - \int n(\mathbf{r}) v_{xc}[n(\mathbf{r})] d\mathbf{r} \tag{3.30}$$

In this way, the calculations could be solved self-consistently, with a trial density $n(\mathbf{r})$, one could get the effective Kohn-Sham potential, and then could be used in solving the one-electron Schrödinger equations, after that, a new density is obtained from the wave functions. The KS-theory is exact in principle, but the exact form for the exchange and correlation correction is unknown. Hence, different approximations for E_{xc} are proposed.

3.3.3 Local Density Approximation

In local density approximation (LDA), the charge density is treated locally and considered as a homogeneous electron gas, so

$$E_{xc}^{LDA}[n(\mathbf{r})] = \int n(\mathbf{r})\epsilon_{xc}[n(\mathbf{r})]d\mathbf{r}, \tag{3.31}$$

which is only exact for slowly varying density or high density situations. $\epsilon_{xc}(n)$ is the exchange and correlation energy per electron. Therefore, we have the exchange and correlation potential:

$$v_{xc}^{LDA}(\mathbf{r}) = \epsilon_{xc}[n(\mathbf{r})] + n(\mathbf{r})\frac{\delta\epsilon_{xc}[n(\mathbf{r})]}{\delta n(\mathbf{r})} \tag{3.32}$$

In practical, the E_{xc} is generally treated separately into the exchange part E_x and the correlation part E_c, in other words,

$$E_{xc}^{LDA}[n(\mathbf{r})] = E_x[n(\mathbf{r})] + E_c[n(\mathbf{r})] \tag{3.33}$$

Based on the homogeneous electron gas model, the analytical form for the exchange correction could be achieved from the Dirac exchange-energy functional.

$$E_x^{LDA}[n(\mathbf{r})] = -\frac{3}{4}(\frac{3}{\pi})^{1/3}\int n(\mathbf{r})^{4/3}d\mathbf{r} \tag{3.34}$$

The exact analytical form for the correlation correction is still unknown, but several correlation functionals, like Perdew-Zunger (PZ81), Perdew-Wang (PW92), etc. are available using different analytical expressions for $E_x[n(\mathbf{r})]$. The exchange energy for atoms and molecules are normally underestimated by about 10% in LDA[42], but it's compensated by the overestimation of the correlation energy.

3.3.4 Generalized Gradient Approximation

Since the local density approximation is local and it fails for the system with rapid change in electron density, the generalized gradient approximation (GGA) is proposed, where the gradient of the density is introduced and the exchange and correlation energy depends on both electron density and the gradient.

$$E_{xc}^{GGA}[n(\mathbf{r})] = \int f_{xc}[n(\mathbf{r}), \bigtriangledown n(\mathbf{r})]d\mathbf{r}. \tag{3.35}$$

The equation for the exchange and correlation potential is

$$v_{xc}(\mathbf{r}) = \frac{\delta f_{xc}}{\delta n(\mathbf{r})} - \sum_{i=1}^{3}\frac{\partial}{\partial r_i}[\frac{\delta f_{xc}}{\delta(\bigtriangledown_i n(\mathbf{r}))}] \tag{3.36}$$

For GGA, the exchange and correlation parts could also be treated separately, and quite a lot of functionals are available for the exchange correction, correlation correction, or both, like Becke 1988 for the exchange correction, the quite popular Perdew-Burke-Ernzerhof (PBE) functional[43] for condensed system.

The PBE correlation functional is constructed in the following form:

$$E_c^{GGA} = \int n(\mathbf{r})[\epsilon_c(\mathbf{r_s}) + H(\mathbf{r_s}, t)]d\mathbf{r}, \tag{3.37}$$

where $\mathbf{r_s}$ is the local Seitz radius, with

$$\mathbf{r_s} = \left(\frac{3}{4\pi n(\mathbf{r})}\right)^{\frac{1}{3}}. \tag{3.38}$$

Moreover,

$$t = \frac{|\bigtriangledown n(\mathbf{r})|}{2n(\mathbf{r})k_s}, \tag{3.39}$$

is the dimensionless density gradient, with

$$\mathbf{k_s} = \sqrt{\frac{4(3n(\mathbf{r}))^{\frac{1}{3}}}{\pi^{\frac{1}{3}}}}. \tag{3.40}$$

The gradient contribution H could be in the analytical form

$$H(\mathbf{r_s}, t) = \gamma \ln\left\{1 + \frac{\beta}{\gamma}t^2\left[\frac{1 + At^2}{1 + At^2 + A^2t^4}\right]\right\}, \tag{3.41}$$

with

$$A = \frac{\beta}{\gamma}\left[e^{-\epsilon_c/\gamma} - 1\right]^{-1}. \tag{3.42}$$

β and γ are parameters with the value of 0.066725 and 0.031091, respectively.

The exchange part is also proposed,

$$E_x^{GGA} = \int n(\mathbf{r})\epsilon_x(n(\mathbf{r}))F_x(s)d\mathbf{r}, \tag{3.43}$$

with

$$\epsilon_x(n(\mathbf{r})) = -\frac{3}{4}\left(\frac{3n(\mathbf{r})}{\pi^4}\right)^{1/3}, \tag{3.44}$$

and

$$F_x(s) = 1 + \kappa - \kappa/(1 + \mu s^2/\kappa), \tag{3.45}$$

where s is another dimensionless density gradient, $s = r_s^{1/2} t \left(\frac{16}{3\pi^2}\right)^{1/3}$, and μ, κ are the other two parameters, with $\mu = 0.21951$, $\kappa = 0.804$.

Later Y. Zhang and W. Yang pointed out that with the value of 1.245 instead of 0.804 for κ, they could achieve better atomic total energies and molecule atomization energies compared to original PBE, and this functional is named revPBE[44].

3.4 Dispersion Correction

It is commonly known that one of the disadvantage of the KS-DFT is the lack of the description of the long-range correlations, i.e. the vdW interaction, which is quite important for the weak interaction systems, like the molecule adsorption on the interface, stacking of the nucleobase in the DNA, ligand binding in the proteins. Lots of efforts have been carried out to solve this problem with different methodologies. One of the most promising method is to develop the new density functional including the vdW interaction, like the Langreth-Lundqvist density functional[45, 46, 47]. The other one is simply adding an extra empirical $C_6 R_{ij}^{-6}$ term to the DFT calculations, for example, the Grimme's DFT-D dispersion correction[48, 49]. Two generations of the Grimme's dispersion correction, called DFT-D2[48] and DFT-D3[49] will be introduced here, and both of them are implemented in CP2K package and employed in the calculations described in the following chapters.

3.4.1 Grimme's DFT-D2 Correction

In the DFT-D method, the total energy of the system is described by adding the empirical dispersion correction energy to the energy calculated by KS-DFT.

$$E_{DFT-D} = E_{KS-DFT} + E_{disp} \tag{3.46}$$

$$E_{disp} = -s_6 \sum_{i=1}^{N} \sum_{j \neq i}^{N} \frac{C_6^{ij}}{R_{ij}^6} f_{damp}(R_{ij}) \tag{3.47}$$

$$f_{damp}(R_{ij}) = \frac{1}{1 + e^{-d(R_{ij}/R_r - 1)}} \tag{3.48}$$

Here, s_6 is the global scaling factor for different density functionals. The values of 1.0 and 0.75 are used for revPBE and PBE, respectively. N is the number of atoms in the system, thus all the pair interactions are included. C_6^{ij} is the C_6 coefficient for the atom pair i, j, and it is taken from the

geometric mean of the C_6^i and C_6^j, i.e. $C_6^{ij} = \sqrt{C_6^i C_6^j}$. R_{ij} is the distance between atom i and atom j. The damping function in equation 3.48 is used to describe the dispersion correction, in which d is chosen to be 20, and R_r is the sum of the vdW radii.

The commonly used S22[50] sets containing 22 sets of non-covalent interacting bimolecular systems are employed to test the efficiency of this dispersion correct. As we are not interested in the interaction between different nucleobases, four sets are removed, resulting only 18 bimolecular sets (see in Table 3.1). Only single-point energy calculations are performed with PBE exchange and correlation functional. Then the binding energies are compared to the estimated CCSD(T) calculations at the basis set limit[51]. Also the contribution of the dispersion correction are listed in Table 3.1. With the dispersion correction, most of the binding energies are overestimated, especially for the case of $(CH4)_2$, Ethene/ethane and $(NH3)_2$, which are overestimated by ∼30%. This might be improved by using another density functional. Moreover, the dispersion correction is necessary in order to get a reasonable binding energy, especially for the benzene dimer (C_{2h}, C_{2v}, T-shape), which is a well-known $\pi - \pi$ interaction system and with the dispersion correction, the energy overestimation is less than 10% while the dispersion correction contributes 226%,122%, and 87% of binding energy, respectively.

3.4.2 Grimme's DFT-D3 Correction

The total energy with DFT-D3 correction is the same as in DFT-D2 (see equation 3.46), but here for the dispersion correction energy E_{disp}, both two-body and three-body terms are considered, while only two-body term is considered in DFT-D2.

$$E_{disp} = E^{(2)} + E^{(3)} \tag{3.49}$$

The two body term is give by

$$E^{(2)} = -\sum_{ij}\sum_{n=6,8} s_n \frac{C_n^{ij}}{R_{ij}^n} f_{damp,n}(R_{ij}). \tag{3.50}$$

The meaning of each term is the same as in DFT-D2. However, instead of only considering the C_6 term, the C_8 term is also considered. Moreover, only the global scaling factor s_8 is scaled for different density functional, while the s_6 value is fixed in order to achieve the asymptotical property. The damping function is defined as follow:

$$f_{damp,n}(R_{ij}) = \frac{1}{1 + 6(R_{ij}/(s_{r,n}R_0^{ij}))^{-\alpha^n}} (n = 6, 8) \tag{3.51}$$

Table 3.1: Binding Energies Calculated at PBE-D/TZV2PX Level with Dispersion Contributions for 18 Non-covalent Bimolecular Systems (all in eV).

	$\Delta E_{binding}$		ΔE_{disp}
	Est. CCSD(T)[a]	PBE-D	
$(NH_3)_2$	-0.137	-0.176	-0.060
$(H_2O)_2$	-0.218	-0.244	-0.033
Formic acid dimer(C_{2h})	-0.807	-0.878	-0.109
Formamide dimer (C_{2h})	-0.692	-0.741	-0.115
2-pyridoxine/2-aminopyridine	-0.724	-0.805	-0.172
$(CH_4)_2(D_{3d})$	-0.023	-0.031	-0.036
$(C_2H_4)_2(D_{2d})$	-0.065	-0.085	-0.093
Benzene/$CH_4(C_3)$	-0.065	-0.078	-0.095
Benzene dimer(C_{2h})	-0.118	-0.110	-0.248
Pyrazine dimer (C_s)	-0.192	-0.177	-0.269
Indole/benzene	-0.226	-0.189	-0.370
Ethene/ethane(C_{2v})	-0.066	-0.087	-0.043
Benzene/$H_2O(C_s)$	-0.142	-0.169	-0.101
Benzene/$NH_3(C_s)$	-0.102	-0.120	-0.099
Benzene/HCN(C_s)	-0.193	-0.226	-0.134
Benzene dimer (C_{2v})	-0.119	-0.130	-0.158
Indole/benzene (T-shape)	-0.248	-0.265	-0.230
Phenol dimer	-0.306	-0.309	-0.177

[a] The values are taken from Ref. [51], and converted to eV afterwards.

where $s_{r,n}$ is the local scaling factor depending on the order, and R_0^{ij} is the cutoff radii which could be calculated with DFT. The $s_{r,6}$ is a second empirical parameter needed for DFT-D3 depending on different density functionals, while $s_{r,8}$ if fixed. The exponent term α^n is set to 14 for n=6, and to 16 for n=8. For the three-body term,

$$E^{(3)} = -\sum_{ijk} f_{d,(3)}(\overline{r}_{ijk} E^{ijk}). \tag{3.52}$$

It sums up all the possible triple atom groups ijk in the system, and the damping function is the same as equation 3.51 with s_r=4/3 and α=16. A C_9 term is also considered in calculating E^{ABC}, with $C_9^{ABC} \approx -\sqrt{C_6^{AB} C_6^{AC} C_6^{BC}}$, and C_6^{AB} is related to the coordination number of atom A and B respectively.

3.5 Scanning Tunneling Microscope

The scanning tunneling microscope is one of the most widely used instrument in surface science, which could give surface images at atomic resolution. It was first invented by Gerd Binnig and Heinrich Rohrer in 1981[52], and because of this, the Nobel Prize in Physics was awarded to them in 1986. In STM, it consists a scanning tip, which could scan in xy plane and record the corresponding height in z direction. Moreover, a voltage is applied between the tip and the scanned surface, therefore, electrons could tunnel through the vacuum space between them and the tunneling current is generated. In experiment, if the isocurrent surface is mapped, the tip height is adjusted in order to keep the current constant.

3.5.1 Tersoff-Hamann Approximation

J. Tersoff and D. R. Hamann[53, 54] proposed a theoretical model for STM, where the tip is considered as a locally spherical potential well. So, based on first-order perturbation theory, the tunneling current is given by

$$I = \frac{2\pi e}{\hbar} \sum_{\mu\nu} f(E_\mu)[1 - f(E_\nu + eV)]|M_{\mu\nu}|^2 \delta(E_\mu - E_\nu), \tag{3.53}$$

where $f(E)$ is the Fermi function, V is the applied voltage between the tip and the scanned surface, $M_{\mu\nu}$ is the tunneling matrix element between the tip state $\psi(\mu)$ and the scanned surface state $\psi(\nu)$. And E_μ is the energy of tip state $\psi(\mu)$ without tunneling. After taking consideration of the limits of small voltage and temperature in the experiment, expanding the surface state $\psi(\nu)$, and expanding the tip state $\psi(\mu)$ based on the locally spherical potential well model, we could get the following equation for the tunneling current:

$$I = 32\pi^3 \hbar^{-1} e^2 V D_t(E_F) R^2 k^{-4} e^{2kR\sqrt{\phi}} \times \sum_{\nu} |\psi_\nu|^2 \delta(E_\nu - E_F), \tag{3.54}$$

where D_t is the density of states of the tip, R is the curvature of the spherical tip, ϕ is the work function, and $k = \sqrt{2m}/\hbar$ with m represents the mass of electron.

In our simulation, we consider the states at Fermi energy within the bias V_b (in eV, the value also corresponds to the applied voltage in the experiment), as the term $\sum_\nu |\psi_\nu(\mathbf{r}_0)|^2 \delta(E_\nu - E_F)$ in equation 3.54 represents the surface local density of states (LDOS) at Fermi energy, which is proportional to the total valence electron density in free-electron metals. Thus,

$$I \propto n_b(z) e^{2kR\sqrt{\phi}}, \tag{3.55}$$

where $n_b(z)$ is the charge density of the states within V_b from the Fermi energy, z is the height of the tip. Hence, in order to model the isocurrent STM image from experiment, we only have to keep $n_b(z)e^{2kR\sqrt{\phi}}$ at constant value for different positions in xy plane.

3.6 Maximally-localized Wannier Function

For solid state systems, generally the calculations are performed in reciprocal space, and the system could be described by a set of Bloch states $\psi_{n\mathbf{k}}(\mathbf{r})$, where n and $\mathbf{k}$ are the quantum numbers for the band index and wave vector, respectively. However, these are not associated to the real space structure directly. Thereby, the Wannier functions are introduced to describe the system in real space, and different schemes are available to construct them. The Wannier functions could be localized according to the Marzari-Vanderbilt (MV) scheme[55] and is called the maximally-localized Wannier Function (MLWF). They are constructed in real space from the Bloch bands $\psi_{n\mathbf{k}}(\mathbf{r})$ generated from k-space as following:

$$|w_{n\mathbf{R}}\rangle = \frac{V}{(2\pi)^3} \int_{BZ} [\sum_{m=1}^{N} U_{mn}^{(\mathbf{k})} |\psi_{m\mathbf{k}}\rangle] e^{-i\mathbf{k}\cdot\mathbf{R}} d\mathbf{k}. \tag{3.56}$$

Here, $\mathbf{R}$ is the lattice vector in real space. $U^{(\mathbf{k})}$ is a unitary matrix and it is integrated over the entire Brillouin zone (BZ). The different choice of the unitary matrix $U^{(\mathbf{k})}$ could result in different Wannier functions. Thus, in the MV scheme, the specific $U^{(\mathbf{k})}$ is chosen in order to minimize the total of the quadratic spreads (Ω in equation 3.57) of the Wannier functions.

$$\Omega = \sum_{n}^{N} [\langle r^2 \rangle_n - \langle r \rangle_n^2] \tag{3.57}$$

With the help of the MLWF, the center of the function, i.e. the Wannier center could be localized, and it represents the position of the localized electron pairs of the chemical bonds, or the atomic lone pair. In this case, all the atoms are positive charged, as they lose all the outermost electrons, so the charge would be equal to the number of the outer shell electrons (for example, +6 for O atom, +1 for H atom), while for the Wannier centers, they're all negatively charged by two electrons. Hence, the molecular dipole moment could be obtained from the position and charge of atoms plus Wannier centers in the system.

Chapter 4

Water Cluster Adsorption on Single BN or C Layer

Water is ubiquitous in the world and shows a lot of anomalous properties. Small water clusters including only several water molecules are studied intensively in both experiment[56, 57, 58, 59, 60, 61, 62, 63, 64] and theory[65, 66, 67, 68, 69, 70, 71, 72, 73, 74]. In this chapter, motivated by the adsorption experiment of small water clusters on the bare nanomesh, the adsorption behavior of small water clusters (from water monomer to different isomers of water hexamer) is studies on a free-standing boron nitride (BN) layer, and due to the similarity between BN and graphene, as both of them are all sp^2 hybridized and form this honey-comb like structures, the adsorption of water cluster is also investigated on graphene.

4.1 Method

All calculations are performed with the CP2K package[75], using a hybrid Gaussian and plane waves (GPW) scheme [76]. The Perdew-Burke-Ernzerhof (PBE) functional[43] is used for both exchange and correlation correction in DFT. Besides, Grimme's D2 vdW dispersion correction potential[48] is added to the pure DFT calculation. The energy cutoff is set to 280 Ry for the plane wave expansion of the density. The Goedecker-Teter-Hutter(GTH) pseudopotentials[77, 78, 79] are employed to represent the atomic core. Triple zeta molopt basis sets[80] are used for C, O and H, while short range double zeta molopt basis sets are used for B and N. The Broyden-Fletcher-Goldfarb-Shanno (BFGS) method[81, 82, 83, 84] is used for the geometry optimization, while the robust orbital transformation (OT) method[85] with the direct inversion in the iterative subspace (DIIS)[86] minimizer is employed for the

wavefunction optimization. The system is periodic in xy directions and a sufficient vacuum of about 15 Å is added in z direction.

An 8×8 single flat layer of BN or graphene is initially used for the geometry optimization. The typical adsorption sites considered here are on top of the atoms (B, N, or C, and they are denoted as topB, topN, or topC, respectively), on top of the center of the BN or CC bond (denoted as tbond), and on top of the center of the hexagonal ring (denoted as tcenter). For water monomer, dimer and trimer, only the global minima structures are considered in the adsorption. While for water tetramer, three different isomers are considered: one water molecule externally attached to the cyclic water trimer with a hydrogen bond (H-bond), cyclic water tetramers with the orientation of the dangling H in udud (u is denoted for dangling H atoms pointing up to the vacuum, and d is denoted for H atoms pointing down to the substrate) and uudd configurations. For pentamer, the cyclic ring configuration and the cage configuration are considered as they are the two lowest energy isomers. For water hexamer, it has several isomers with very close energy value. Hence, more configurations are employed here for water hexamer: the cyclic ring configuration, book configuration, cage configuration, and prism configuration. To compare the binding strength in different adsorption site, two binding properties, i.e. the interaction energy and adsorption energy are evaluated, and unless otherwise addressed, these energies are recorded per water molecule. For interaction energy, it's the energy of the whole system compared to the sum of the optimized free-standing substrate and the water cluster, $E_{\text{int}} = (E_{\text{tot}} - E_{\text{sub}} - E_{(\text{H}_2\text{O})_n})/n$. While the adsorption energy is compared to the free water molecules in gas phase, i.e. $E_{\text{ads}} = (E_{\text{tot}} - E_{\text{sub}} - n \times E_{\text{H}_2\text{O}})/n$.

4.2 Water Monomer

Two adsorption types are considered for water monomer: with O or H adsorbed on the single layer respectively, which would result in eight different adsorption sites for BN layer and six adsorption sites for graphene. With the O atom adsorbed on the BN layer, the two H atoms are pointing outward to the vacuum. For all the four adsorption sites investigated here, the O atom adsorption cannot be stabilized. After geometry optimization, the H atoms flipped down and some binds directly with the substrate through OH$\cdots$N H-bonds. In configuration O_topB, besides flipping, the molecule also rotates so that the OH bonds would point to the nearby N atom comfortably, in this case, two OH$\cdots$N H-bonds are formed at 2.57 and 2.61 Å away. In the O_topN configuration, the O atom is still on top of the N atom after

Table 4.1: Water Monomer: Interaction and Adsorption Energy for Different Adsorption Site

	Energy (eV)		OH$\cdots$O		OH$\cdots$N	
	E_{int}	E_{ads}	n	$\bar{d}$ (Å)	n	$\bar{d}$ (Å)
BN Layer						
O_topB	-0.186	-0.186	0		2	2.59
O_topN	-0.136	-0.136	0		0	
O_tbond	-0.179	-0.179	0		1	2.33
O_tcenter	-0.185	-0.185	0		1	2.49
H_topB	-0.169	-0.169	0		1	2.53
H_topN	-0.154	-0.154	0		1	2.22
H_tbond	-0.167	-0.167	0		1	2.33
H_tcenter	-0.148	-0.148	0		1	2.59
C Layer						
O_topC	-0.137	-0.137	0		0	
O_tbond	-0.137	-0.137	0		0	
O_tcenter	-0.149	-0.149	0		0	
H_topC	-0.112	-0.112	0		0	
H_tbond	-0.109	-0.109	0		0	
H_tcenter	-0.128	-0.128	0		0	

optimization, and no H-bonds are formed, which is the reason why the adsorption energy is almost 0.05 eV lower compared to the other O adsorption sites. When O adsorbed above the center of the BN bond (tbond), after flipping, one H points to the N atom underneath, and an H-bond is formed with the H$\cdots$N distance of 2.33 Å, while the other OH bond is almost parallel to the substrate. In the case of O adsorbed above the center of the BN ring (tcenter), two OH$\cdots$N H-bonds are formed at 2.49 and 2.74 Å. Thereby, we could see that H atoms adsorbed on the BN layer are more preferred, as they could form H-bond with the N atoms in the substrate. The most favorable adsorption site could be the two OH bonds pointing down to the N atoms within the distance of H-bonds, while the position of the O atom could shift a little bit, as we have already seen from the adsorption energies of O_topB and O_tcenter sites. The binding energy is more related to the number of H-bonds formed, while quite different O positions could still give similar adsorption energies.

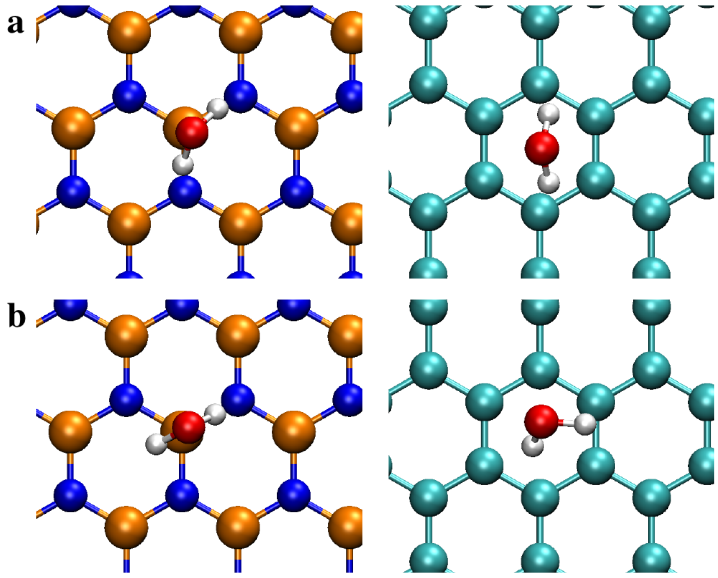

Figure 4.1: Top view of the most binded adsorption sites for water monomer on a BN or C layer. **a**. O_topB on BN, and O_tcenter on C layer, respectively. **b**. H_topB on BN, and H_tcenter on C layer, respectively. The atoms and bonds are represented by ball and stick. The color scheme is as following: red for O, white for H, orange for B, blue for N, and cyan for C, respectively.

For the configurations with H atom initially adsorbed on the BN layer, the H atom is placed directly above the adsorption site with the OH bond almost perpendicular to the BN plane, and the other one is parallel to the substrate. For all the four configurations, the water molecules could be stabilized. In topB configuration, the atop H moves towards the BN ring after optimization, in this case, the O atom is almost on top of B now, at a distance of 3.2 Å. The H atom with the OH bond initially parallel to the BN layer becomes closer to the nearby N and forms a OH$\cdots$N H-bond at 2.53 Å. Although with only one H-bond, the adsorption energy of this configuration is still a little bit stronger compared to other H adsorption sites, which might be due to the attractive contribution between the B and O atoms. For the other three configurations, the water molecule almost stays in the initial orientation, with one OH bond pointing to the BN and another one parallel to the substrate. Just in all three cases, the H atoms pointing down move a little bit closer to the nearby N, and H-bonds are formed.

The O adsorption also could not be stabilized on the graphene substrate, as for all three configurations, the H atoms all flip down after geometry optimization, and the heights of the O are all around 3.2 Å above the graphene, but no rotation of the molecule is observed. Since no H-bond could be formed

between the C and water, the adsorption energy for water on graphene is a little bit weaker compared to the BN layer. With the H adsorbed on the graphene, they're just like in the BN case, all molecules could stay there with the initial orientation.

4.3 Water Dimer

As we have already seen that the adsorption of the H atoms to the substrate is preferred, while the O atoms cannot be stabilized, hereafter, we will only focus on H adsorbed directly on the substrate. In water dimer, one water molecule is donating an H atom to form the internal OH$\cdots$O H-bond. So for the H-bond donor, it has only one dangling H atom, while for the H-bond acceptor, both H atoms are available. In the global minima structure of the water dimer, the dangling H atoms from different water molecules are pointing to opposite directions. Therefore, two types of the adsorption behavior of the H atoms are addressed. One is from the H-bond donor, in this case, only one H will be pointing to the substrate (denoted as duu), and the other one is the H atom from the H-bond acceptor, which could bring two H atoms pointing down (denoted as udd).

In duu case, one H-bond is formed by the H_d atom in all four configurations with a H$\cdots$N distance of 2.82 Å for topB, 2.26 Å for topN, 2.33 Å for tbond and 2.58 Å for tcenter respectively, while the other two H atoms are pointing outwards. During the geometry optimization, the structure of the water dimer could be sustained, indicating that the interaction between the water molecules are stronger than the interaction with the substrate. The adsorption energies are also quite similar for all four adsorption sites (see in Table 4.2), with tcenter configuration slightly stronger. With two hydrogen atoms pointing down (udd cases), we simply took the mirror images of the initial structures in duu, which means, for example, in udd-center, the H_u is above the center of the BN ring. Two H-bonds are formed except for topN adsorption site, and the third H atom from the H-bond donor water molecule is pointing up this time. So the adsorption energy increases a lot, and also the tcenter configuration is the most favored here, with H$\cdots$N distances of 2.45 and 2.50 Å. We have also tested for the most favorable adsorption site ddu-tcenter with all the three free H atoms pointing down (denoted as ddd-center) and expected that in this case three H-bonds could be formed. However, it turns out that this configuration is less favored and only two H-bonds are sustained from the H-bond acceptor water molecule after geometry optimization. The interaction energy and adsorption energy is -0.143 and -0.278 eV, respectively. This could be because the interaction between

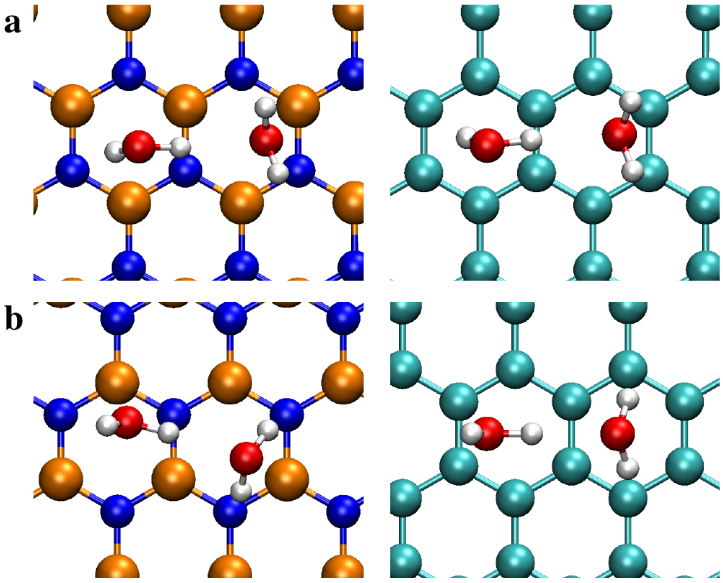

Figure 4.2: Top view of the most binded adsorption sites for water dimer on a BN or C layer. **a**. duu_tcenter on BN, and duu_tcenter on C layer, respectively. **b**. udd_tcenter on BN, and udd_tbond on C layer, respectively.

water dimer and the BN layer is weaker, so the water dimer itself tends to form the structure that is lower in energy. For the adsorption of water dimer on the graphene layer, the situation is quite similar to the adsorption on BN and the water dimer could be stable in all chosen adsorption sites. The adsorption energy here also significantly increases with two H pointing down instead of one H atom. But the same as in water monomer, the binding of water dimer to graphene is slightly weaker compared to BN.

4.4 Water Trimer

The global minima structure of water trimer is cyclic, with each water molecule donating one H atom to form the HO$\cdots$H H-bond and the rest H atoms pointing towards two opposite directions. Thus, after adsorption on a substrate, it would also give duu or udd configurations just as in water dimer. For udd configurations, only one H atom is chosen to be placed on different adsorption sites. In duu adsorption sites, one OH$\cdots$N H-bond is formed only in topN and tbond configurations at the distance of 2.26 and 2.35 Å respectively. The adsorption energies of these two configurations are almost the same, -0.393 and -0.388 eV respectively, which is a little bit lower compared to tcenter or topB configurations, with an adsorption energy of

Table 4.2: Water Dimer: Interaction and Adsorption Energy for Different Adsorption Site

	Energy (eV)		OH$\cdots$O		OH$\cdots$N	
	E_{int}	E_{ads}	n	$\bar{d}$ (Å)	n	$\bar{d}$ (Å)
BN Layer						
duu_topB	-0.096	-0.232	1	1.93	0	
duu_topN	-0.095	-0.230	1	1.93	1	2.26
duu_tbond	-0.096	-0.232	1	1.92	1	2.33
duu_tcenter	-0.105	-0.241	1	1.96	1	2.58
udd_topB	-0.151	-0.287	1	1.87	1	2.41
udd_topN	-0.145	-0.281	1	1.85	0	
udd_tbond	-0.153	-0.288	1	1.87	2	2.53
udd_tcenter	-0.166	-0.302	1	1.86	2	2.48
C Layer						
duu_topC	-0.088	-0.224	1	1.92	0	
duu_tbond	-0.091	-0.226	1	1.92	0	
duu_tcenter	-0.096	-0.232	1	1.93	0	
udd_topC	-0.127	-0.262	1	1.87	0	
udd_tbond	-0.138	-0.274	1	1.87	0	
udd_tcenter	-0.127	-0.263	1	1.85	0	

-0.384 and -0.366 eV respectively. In all optimizations, no flipping of the pointing-up H atoms are observed, thus the structure of the water trimer is sustained.

With two H atoms pointing down, the adsorption energy is improved. In topN configuration, two additional H-bonds are formed between the water trimer and the BN layer, at 2.29 and 2.67 Å. Although only one OH$\cdots$N H-bond is formed in the rest three configurations, the dangling H atom is still pointing straightly to the nearby N atom with the distance a little bit long, of 2.76 and 2.84 Å respectively in tcenter and tbond configurations, which maybe could explain why the tcenter configuration has the lowest binding energy. While for topB configuration, the dangling H atom is still pointing to the B atom, thus it's not surprising that the binding for this one is the weakest. But the adsorption energy is still very close in different adsorption sites due to the weak interaction between the adsorbates and the substrate.

When the water trimer adsorbs on a graphene layer, the binding ener-

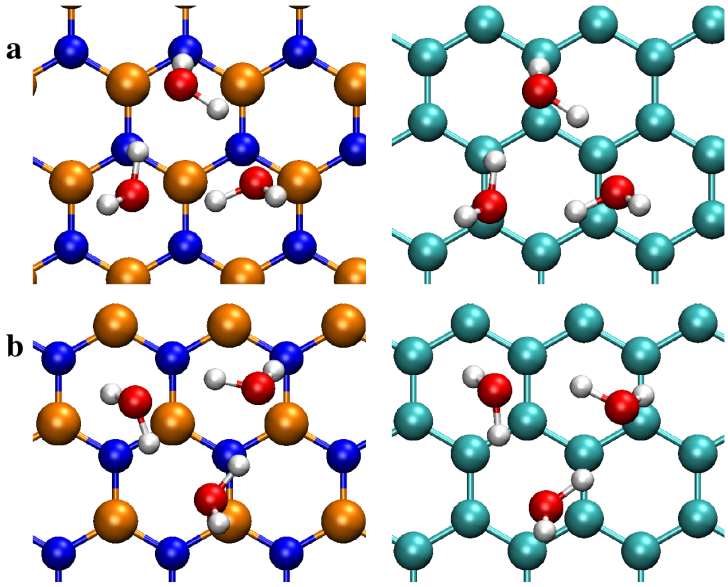

Figure 4.3: Top view of the most binded adsorption sites for water trimer on a BN or C layer. **a**. duu_topN on BN, and duu_topC on C layer, respectively. **b**. udd_tcenter on BN, and udd_tcenter on C layer, respectively.

gies are quite close for all three configurations in duu or udd configurations. Moreover, with two H atoms pointing down, the binding energy improves the most in tcenter configuration, by about 0.02 eV. In duu adsorption, the most favored binding site (topC) is with the pointing-down H above the C atom, with an H-C distance of 2.43 Å, but the binding energy is only about 0.006 eV stronger compared to tbond site. As there's no strong interaction between the water cluster and graphene layer, the water trimer could also be stabilized on other adsorption sites besides what we have investigated here. In udd adsorption, the most favored binding site changes to tcenter site, but the energy difference for all three configurations are less than 0.006 eV. As usual, it's less binded on the graphene layer compared to BN.

4.5 Water Tetramer

In water tetramer, three different isomers are investigated here. First, the udd structure of water trimer is employed and one additional pointing-up water molecule is externally attached to the pointing-down water molecule in the trimer. This additional water molecule also works as the H-bond donor, donating one H atom to the pointing down water molecule. The O atom in this extra water molecule is chosen to be placed on different adsorption

Table 4.3: Water Trimer: Interaction and Adsorption Energy for Different Adsorption Site

	Energy (eV)		OH$\cdots$O		OH$\cdots$N	
	E_{int}	E_{ads}	n	$\bar{d}$ (Å)	n	$\bar{d}$ (Å)
BN Layer						
duu_topB	-0.083	-0.366	3	1.86	0	
duu_topN	-0.110	-0.393	3	1.85	1	2.26
duu_tbond	-0.106	-0.388	3	1.86	1	2.35
duu_tcenter	-0.102	-0.384	3	1.85	0	
udd_topB	-0.106	-0.389	3	1.86	1	2.27
udd_topN	-0.120	-0.403	3	1.86	2	2.48
udd_tbond	-0.122	-0.404	3	1.85	1	2.38
udd_tcenter	-0.128	-0.411	3	1.86	1	2.32
C Layer						
duu_topC	-0.092	-0.375	3	1.85	0	
duu_tbond	-0.086	-0.369	3	1.86	0	
duu_tcenter	-0.084	-0.366	3	1.85	0	
udd_topC	-0.096	-0.379	3	1.85	0	
udd_tbond	-0.099	-0.381	3	1.85	0	
udd_tcenter	-0.102	-0.385	3	1.85	0	

sites. This configuration is denoted as uddu. The other two isomers are the regular cyclic water tetramer, with each water molecule donating one H to form the H-bond with other water molecules. Depending on the orientation of the free H atoms in each water molecule, two different configurations are employed here, called uudd and udud. For these two configurations, one of the pointing-down H atom is placed above the adsorption site. All water tetramer isomers contain four OH$\cdots$O H-bonds. Here, the udud isomer is the one lowest in energy. Obviously, the uddu configuration is not favored by water tetramer, therefore, the adsorption energy of uddu to BN layer is the weakest compared to other isomers.

In topB structure of the uddu isomer, two OH$\cdots$N H-bonds are formed at 2.07 and 2.56 Å. The O atoms of the two pointing-up water molecules are on top of the B, hence, due to the attraction between B and O, and also the H-bonds, this is the most binded structure in uddu water tetramer. Two OH$\cdots$N H-bonds are also formed in tbond and tcenter configurations,

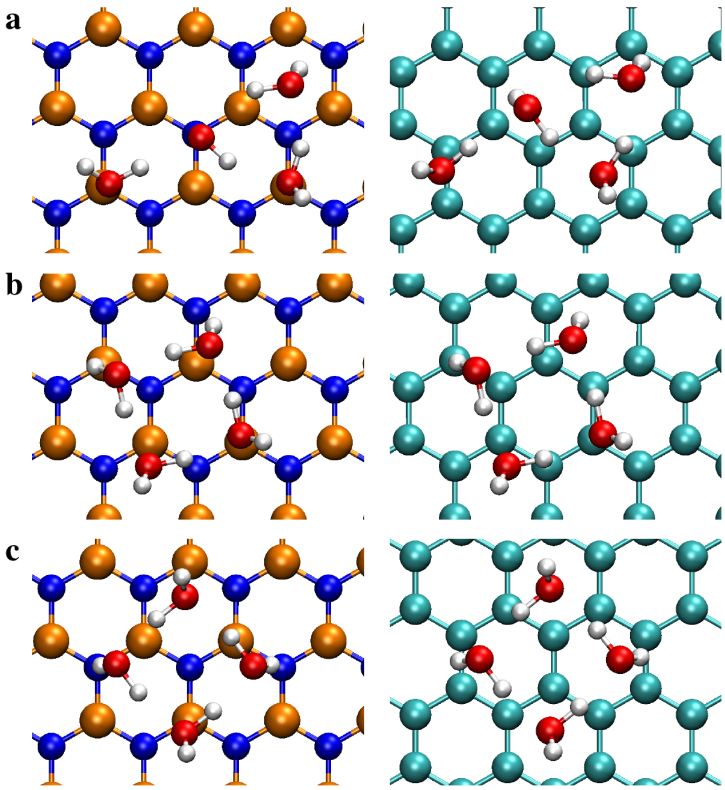

Figure 4.4: Top view of the most binded adsorption sites for water tetramer on a BN or C layer. **a**. uddu_topB on BN, and uddu_tbond on C layer, respectively. **b**. uudd_topB on BN, and uudd_topC on C layer, respectively. **c**. udud_topN on BN, and uddu_tbond on C layer, respectively.

but only one for topN configuration. The adsorption energy improves quite a lot in uudd configurations and the most favored one is still the topB site as both pointing down H atoms could contribute H-bonds. For tbond configuration, also two OH$\cdots$N H-bonds are formed, while only one H-bond for the other two configurations. Udud configuration is the global minima structure of water tetramer, and it also binds strongest compared to uddu or uudd configurations. All the pointing down H could form H-bonds with the nearby N atom in the substrate except for tcenter configuration. After all, the udud-topN configuration is the most stable structure for water tetramer adsorption, with an adsorption energy of -0.488 eV. When adsorbed on graphene layer, the strength of different isomers are similar to those on BN, with the binding of uddu the weakest. Here, the most favored adsorption site is udud_tbond, with an adsorption energy of -0.475 eV, only about 0.01 eV higher compared to udud_topN site on BN (see Table 4.4).

Table 4.4: Water tetramer: Interaction and Adsorption Energy for Different Adsorption Site

	Energy (eV)		OH$\cdots$O		OH$\cdots$N	
	E_{int}	E_{ads}	n	$\bar{d}$ (Å)	n	$\bar{d}$ (Å)
BN Layer						
uddu_topB	-0.115	-0.397	4	1.88	2	2.32
uddu_topN	-0.105	-0.387	4	1.90	1	2.19
uddu_tbond	-0.102	-0.384	4	1.91	2	2.50
uddu_tcenter	-0.102	-0.384	4	1.89	2	2.35
uudd_topB	-0.122	-0.482	4	1.70	2	2.37
uudd_topN	-0.103	-0.464	4	1.72	1	2.26
uudd_tbond	-0.105	-0.466	4	1.70	2	2.48
uudd_tcenter	-0.106	-0.467	4	1.69	1	2.28
udud_topB	-0.109	-0.486	4	1.70	2	2.53
udud_topN	-0.111	-0.488	4	1.70	2	2.29
udud_tbond	-0.106	-0.484	4	1.70	2	2.40
udud_tcenter	-0.105	-0.483	4	1.69	2	2.65
C Layer						
uddu_topC	-0.092	-0.374	4	1.90	0	
uddu_tbond	-0.093	-0.375	4	1.88	0	
uddu_tcenter	-0.087	-0.369	4	1.88	0	
uudd_topC	-0.097	-0.458	4	1.71	0	
uudd_tbond	-0.096	-0.457	4	1.70	0	
uudd_tcenter	-0.096	-0.457	4	1.70	0	
udud_topC	-0.093	-0.470	4	1.70	0	
udud_tbond	-0.098	-0.475	4	1.69	0	
udud_tcenter	-0.091	-0.468	4	1.70	0	

4.6 Water Pentamer

Two different isomers, called the cage and ring configurations are considered here for the adsorption. For the ring isomer, the five water molecules are arranged cyclicly, with each donating one H atom to the next water molecule, and another H atom is freely pointing outward. Here, the adsorbed water pentamer is in the ddudu configuration, in order to form more H-bonds with

the BN substrate. For the cage isomer, first four water molecules are arranged in the dudu configuration as in cyclic water tetramer, but with the pointing up water molecules a little bit higher. Then the fifth water molecule is almost above the center of the tetramer, but in a much higher position. And this water molecule works as both the H-bond donor and acceptor, i.e. it accepts one H from the pointing-up molecule and donates one H to the other pointing-up water molecule. Thus, in the cage isomer, six OH$\cdots$H H-bonds are formed instead of five in the ring isomer. However, only two H atoms could bind directly to the substrate, while three H atoms are pointing down in the ring isomer. As the ring isomer is the most favored water pentamer structure, the binding energies for ring isomer are much stronger than the cage isomer. When the cage isomer is adsorbed on the BN layer, two H-bonds could be formed except for the tcenter configuration, which results in the weaker binding for tcenter site.

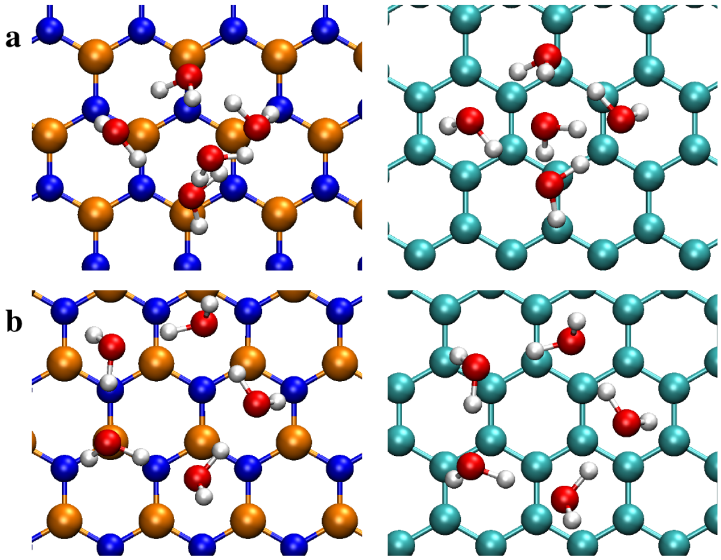

Figure 4.5: Top view of the most binded adsorption sites for water pentamer on a BN or C layer. **a**. cage_topB on BN, and cage_tcenter on C layer, respectively. **b**. ring_topB on BN, and ring_topC on C layer, respectively.

When the ring isomer is adsorbed, three OH$\cdots$N H-bonds are formed in the topB, topN and tcenter configurations, as we expected. This is also why they have very close binding energies. For the tbond configuration, only two H-bonds are formed, which could be attributed to the higher binding energy. Although the third pointing-down H atoms is not so far away from the nearby N, in about 2.75 Å, the OH$\cdots$N angle is not so favored, with a

value of 130.18°. The situation of the water pentamer adsorbed on a graphene sheet is similar to BN, just less binded. The binding energy of the cage isomer

Table 4.5: Water pentamer: Interaction and Adsorption Energy for Different Adsorption Site

	Energy (eV)		OH$\cdots$O		OH$\cdots$N	
	E_{int}	E_{ads}	n	$\bar{d}$ (Å)	n	$\bar{d}$ (Å)
BN Layer						
cage_topB	-0.072	-0.448	6	1.80	2	2.26
cage_topN	-0.068	-0.444	6	1.79	2	2.17
cage_tbond	-0.070	-0.446	6	1.78	2	2.19
cage_tcenter	-0.061	-0.437	6	1.80	1	2.38
ring_topB	-0.113	-0.505	5	1.67	3	2.48
ring_topN	-0.110	-0.502	5	1.67	3	2.47
ring_tbond	-0.100	-0.491	5	1.66	2	2.34
ring_tcenter	-0.112	-0.504	5	1.70	3	2.47
C Layer						
cage_topC	-0.050	-0.426	6	1.79	0	
cage_tbond	-0.050	-0.426	6	1.79	0	
cage_tcenter	-0.051	-0.427	6	1.79	0	
ring_topC	-0.099	-0.491	5	1.66	0	
ring_tbond	-0.094	-0.486	5	1.66	0	
ring_tcenter	-0.094	-0.486	5	1.66	0	

is about 0.02 eV lower compared to the binding on BN. Here, as no H-bond could be formed between the water and graphene, the binding energies are almost identical for all three configuration. For the ring structure, the binding increases by about 0.06 eV, and it is less weaker compared to BN. With ring isomer, the most favored structure becomes the topC adsorption site.

4.7 Water Hexamer

For water hexamer, several isomers have very close energies. Here, we only investigate the adsorption of the ring, cage, book and prism isomers, and for prism isomer, two adsorption configurations are considered besides the different adsorption positions on the BN or graphene layer. In the ring isomer,

it's also a cyclic structure, with each water molecule donating one H atom to neighboring water molecule, while for the dangling H atoms, they are in the dududu configuration. In the cage isomer, similar to pentamer, four water molecules are arranged like the dudu water tetramer structure, with the two pointing up water molecules about 0.9 Å higher and the two pointing down H atoms are adsorbed on the substrate directly. The fifth water molecule is above the center of the two pointing up water molecule, accepting the two dangling H atoms underneath, and donating one H to the sixth water molecule, while the other one is pointing outward. The sixth water molecule works both as the H-bond donor and acceptor, accepting one H from the fifth water molecule, and donating one H to the pointing down water molecule in the lower layer. The arrangement of the water molecules in book isomer is similar to the ring isomer. They are also forming the cyclic H-bonds, but the dangling H of the water molecule in position 6 is donated to water molecule in position 3, hence, one extra H-bond is formed and these two water molecules are about 1.5 Å higher. In the isomer of prism, it consists two layers of water trimers and the molecules in the second layer are right above the first layer molecules, hence, they form this prism-like structure. Here, for each water molecule, three OH$\cdots$O H-bonds are formed. In adsorption, different prism facets consisting three or four water molecules could be placed directly onto the substrate, and is named as prism or pside, respectively.

As both of ring and book shape isomers have three H adsorbed on the BN substrate, the binding energies in these two categories are stronger compared to the other three. Even for the same isomer, the prism shape, the pside adsorption to the BN is more preferred. The most preferred structure here is the book_topN structure, -0.506 eV, with two OH$\cdots$N H-bonds formed at about 2.2 Å. The next most favored is the ring_tcenter structure, only 0.002 eV higher, with three H-bonds formed at 2.36, 2.42 and 2.61 Å. For the adsorption on graphene, just like all the previous water clusters, it's very similar to the adsorption behavior on BN, but slightly weaker. Again, the most favored structure is with the book isomer, at tcenter site, with a binding energy of -0.497 eV. Moreover, the binding of the ring isomer to graphene is also relatively preferred, all with an adsorption energy around -0.49 eV. The optimized structures of the most stable adsorption site for each hexamer isomer on BN or graphene could be seen in Figure 4.6, and the energies are listed in Table 4.6 and 4.7.

Table 4.6: Water Hexamer: Interaction and Adsorption Energy for Different Adsorption Site – BN Layer

	Energy (eV)		OH$\cdots$O		OH$\cdots$N	
	E_{int}	E_{ads}	n	$\bar{d}$ (Å)	n	$\bar{d}$ (Å)
ring_topB	-0.097	-0.496	6	1.65	2	2.45
ring_topN	-0.101	-0.500	6	1.66	2	2.41
ring_tbond	-0.104	-0.503	6	1.66	3	2.45
ring_tcenter	-0.105	-0.504	6	1.66	3	2.46
cage_topB	-0.054	-0.468	8	1.80	2	2.36
cage_topN	-0.052	-0.466	8	1.79	2	2.15
cage_tbond	-0.059	-0.473	8	1.79	2	2.19
cage_tcenter	-0.045	-0.459	8	1.80	2	2.47
book_topB	-0.085	-0.497	7	1.73	2	2.47
book_topN	-0.094	-0.506	7	1.71	2	2.21
book_tbond	-0.079	-0.491	7	1.72	2	2.45
book_tcenter	-0.090	-0.502	7	1.71	2	2.43
prism_topB	-0.046	-0.460	9	1.96	2	2.36
prism_topN	-0.047	-0.461	9	1.87	2	2.33
prism_tbond	-0.046	-0.459	9	1.88	2	2.29
prism_tcenter	-0.051	-0.464	9	1.88	2	2.42
pside_topB	-0.062	-0.475	9	1.86	1	2.57
pside_topN	-0.070	-0.483	9	1.86	2	2.38
pside_tbond	-0.074	-0.487	9	1.86	2	2.34
pside_tcenter	-0.061	-0.475	9	1.86	0	

4.8 Binding Energy of Water Clusters

For the adsorption energies of different water clusters adsorbed on a BN or C layer, actually the binding energy of those water clusters from free water molecules in gas phase plays a very important role, as we could see from the difference between adsorption energy and interaction energy in all the tables (see Tables above). Thus, different DFT functionals, PBE, revised PBE (revPBE), and Becke97D, together with Grimme's D2 dispersion correction are used to evaluate the accuracy of different functionals when employed for the binding energies of water dimer, trimer and the ring shaped cyclic water tetramer, pentamer, and hexamer. One thing needs to be noted here

Table 4.7: Water Hexamer: Interaction and Adsorption Energy for Different Adsorption Site – C Layer

	Energy (eV)		OH$\cdots$O		OH$\cdots$N	
	E_{int}	E_{ads}	n	$\bar{d}$ (Å)	n	$\bar{d}$ (Å)
ring_topC	-0.092	-0.491	6	1.65	0	
ring_tbond	-0.092	-0.491	6	1.65	0	
ring_tcenter	-0.093	-0.492	6	1.65	0	
cage_topC	-0.035	-0.450	8	1.79	0	
cage_tbond	-0.036	-0.450	8	1.79	0	
cage_tcenter	-0.045	-0.459	8	1.80	0	
book_topC	-0.077	-0.489	7	1.72	0	
book_tbond	-0.080	-0.492	7	1.72	0	
book_tcenter	-0.085	-0.497	7	1.71	0	
prism_topC	-0.037	-0.451	9	1.88	0	
prism_tbond	-0.035	-0.449	9	1.88	0	
prism_tcenter	-0.038	-0.451	9	1.88	0	
pside_topC	-0.057	-0.471	9	1.85	0	
pside_tbond	-0.056	-0.469	9	1.85	0	
pside_tcenter	-0.056	-0.469	9	1.86	0	

is that the functional Becke97D is reparameterized by Grimme based on Becke97 in oder to cancel the double counting at intermediate distances when an additional dispersion correction is added[48]. Compared to the results calculated in MP2 at the complete basis set limit[71], PBE-D overestimates the binding of water clusters, and the deviation increases as the number of water molecules increases. The underestimation of revPBE-D reaches the largest in the case of water hexamer, about 0.15 eV weaker compared to the result obtained with MP2 at complete basis set limit[71]. B97D-D has the best fit for MP2 results, but further calculations indicated that larger plane wave cutoff to achieve numerical accuracy, which would increase the computational cost when employed to full nanomesh system. Thus, in all the following work, revPBE exchange and correlation functional instead of B97D are used for the calculations of small molecules adsorbed on the full nanomesh system.

Table 4.8: Binding Energy for Different Water Cluster

	Energy (eV)			
	PBE-D	revPBE-D	B97D-D	MP2/CBS[a]
dimer	-0.252	-0.196	-0.206	-0.216
trimer	-0.829	-0.635	-0.662	-0.686
tetramer	-1.448	-1.155	-1.201	-1.198
pentamer	-1.881	-1.497	-1.548	-1.573
hexamer(cage)	-2.383	-1.849	-1.948	-1.990

[a] The values are taken from Ref. [71], and converted to eV afterwards.

4.9 Conclusion

Different small water clusters (monomer to hexamer) have been investigated when adsorbed on a single layer 8×8 BN or C layer. Because of the similar chemical properties of the substrate, the adsorption behavior of water clusters are quite similar on both BN and C layers. But on BN layer, OH$\cdots$N H-bond could be formed between the pointing-down H atoms and the substrate, thus the binding is stronger compared to that on graphene. Still, this is a rather weak adsorption system, the binding energies between the water molecules themselves are much stronger than the binding to the substrate. Therefore, the water molecules would like to form aggregates when adsorbed on the substrate. The most preferred adsorption site might be where the pointing down H atoms could comfortably form H-bond and the O atoms in the pointing-up water molecules are above the B atoms due to the attractive contribution of both H-bonds and the O-B atom pairs. Further investigation on the binding energy of the water clusters with different exchange and correlation functionals reveal that PBE-D largely overestimate the binding energies, while the revPBE-D slightly underestimate it, and the best fit is B97D-D. But considering the balance between accuracy and computational cost, we will employ revPBE instead of B97D for further calculations.

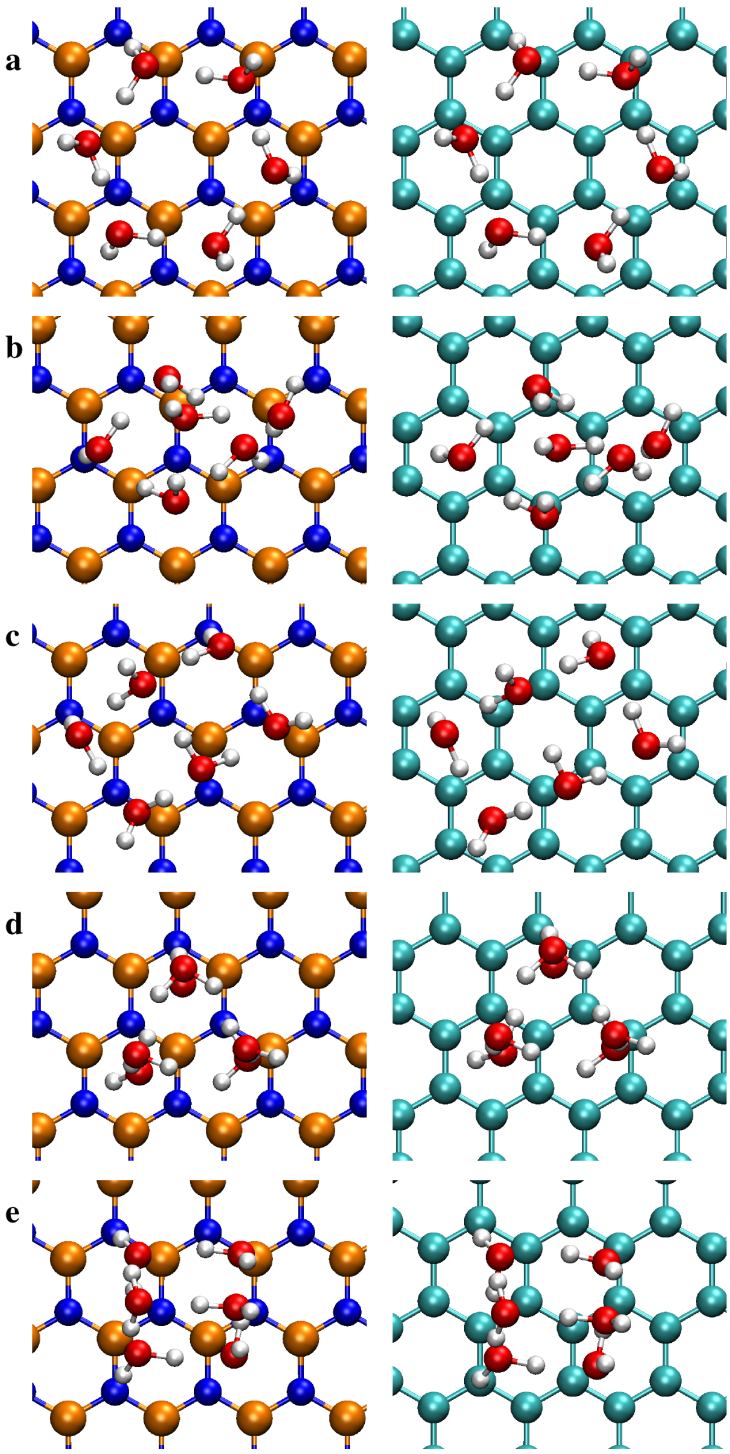

Figure 4.6: Top view of the most binded adsorption sites for water hexamer on a BN or C layer. **a**. ring_tcenter on BN, and ring_tcenter on C layer, respectively. **b**. cage_tbond on BN, and cage_tcenter on C layer, respectively. **c**. book_topN on BN, and book_tcenter on C layer, respectively. **d**. prism_tcenter on BN, and prism_tcenter on C layer, respectively. **e**. pside_tbond on BN, and pside_topC on C layer, respectively.

Chapter 5

Small Water Cluster Deposited in the Pore of the Nanomesh

Recent STM experiments have shown that, by dosing liquid water to the bare h-BN nanomesh on Rh(111), water clusters can be observed in the nanomesh pores. With the present work, we intend to better understand the nature of the interaction of water with the nanomesh, and give indications on the type of structures that have been observed. To this purpose, the corrugated h-BN monolayer on a 12×12 Rh(111) slab is calculated, and its structural and electronic properties are studied in some details. Then the interaction of small water clusters adsorbed on h-BN, with and without the metal, is investigated. The simulation gives insight into the nature of the binding of h-BN to the metal, the role of the corrugation in trapping molecules, and the structure and distribution of the H-bonds formed by the water molecules. Through the simulated STM topography, the optimized structures are compared to the experimental results and the most probable configurations of water aggregates within the pore are identified. The results of our calculations suggest that the water aggregates producing the predominant STM images with three protrusions forming an almost equilateral triangle, with side length of about 0.46 nm, are most likely water hexamers.

5.1 Method

In the chapter, we study by means of density functional theory[41] the structural and electronic properties of h-BN epitaxially grown on Rh(111). A symmetric slab model constituted of a slab of seven 12×12 Rh(111) layers and terminated on both side with one 13×13 h-BN monolayer has been considered to investigate the bare nanomesh. We address more specifically

the binding interactions between metal and h-BN, which are responsible for the variation of the electronic properties between pore and wire. The characterization of the modulation of the work function across the nanomesh, as reported also in experimental works[34], is particularly interesting because it is directly associated to the corrugation and is expected to have an influence on the behavior of adsorbed molecules.

Different water clusters are studied on free-standing h-BN and on the nanomesh, in order to identify the unresolved structures observed in the experiment. The nature of the binding interactions and the stability of the water aggregates trapped in the pore are addressed. The water hexamer is studied with particular care, since it turns out to provide the best match to the STM picture and it is also the most stable aggregate of water molecules, being the building block for the formation of ice clusters. Possible distortions of the hexamer structure as well as its dynamics on the BN monolayer are also taken into account.

All calculations are performed by DFT, using the Gaussian and plane waves formalism[76], as implemented in the CP2K program package[75]. Exchange and correlation are calculated by the revPBE[43, 44] functional, and corrections for the dispersion interactions are added through the Grimme D2[48] formalism. GTH pseudopotentials[77, 78, 79] are used to approximate the interaction of the valence electrons with the atomic cores. In particular, 17 valence electrons are considered for Rh atoms. Double zeta short range basis sets[80] are employed for Rh, B,and N, while triple zeta basis sets are selected to describe O and H. The energy cutoff for the plane waves expansion of the density is set at 500 Ry. The Brillouin zone is sampled only at the Γ point, but still with good accuracy since large simulation cells, containing several hundreds of atoms, are used. For the wavefunction optimization of metallic systems, the Fermi-Dirac smearing of the occupation numbers is applied using 300 K as electronic temperature. Broyden density mixing is used to guarantee smooth convergence within a reasonable number of iterations. Periodic boundary conditions are always applied. The Rh(111) surface is described through a slab model, by adding a sufficient amount of vacuum space (about 20 Å) above the topmost atomic layer, in order to avoid interactions with the periodic images. This simulation setup has been validated on bulk Rh and the Rh(111) surface, obtaining very good agreement with experiment for several parameters, like the lattice parameter (a=3.780 Å), the bulk modulus (258 GPa), the surface energy (0.19 eV/Å), and the surface work function (5.11 eV). [1]

[1]The bulk calculations are performed with a 6 × 6 × 6 cubic box containing 864 Rh atoms. The Rh(111) surface has been modeled by a slab of seven 12 × 12 Rh(111) layers,

The optimized structures are characterized in terms of several structural parameters (corrugation, buckling, bond lengths), the adsorption and the interaction energies, the formation of covalent and hydrogen bonding. The modulation of the electrostatic potential above the surface (i.e. the work function) is of particular interest because it is directly related to the corrugation of the nanomesh and it is expected to affect the adsorption of molecules. By the calculation of charge density differences ($\Delta n(\mathbf{r})$) between the full systems and its constituents (slab and h-BN) at the geometry of the combined system the formation of bonding is monitored. Also the density of states projected on selected subsets of atoms (PDOS), and the description of the electronic structure through MLWF[55] are employed as useful analysis tools to investigate the electronic structure rearrangements induced by binding interactions and polarization. The Tersoff-Hamann approximation[53, 54] for STM simulations is used to reproduce the isocurrent topography above the nanomesh. Given a bias potential V_b (typically a fraction of eV), we determine the isocurrent surface as the set of grid points where

$$n_b(z)e^{2kR\sqrt{\Phi(z)}} = \text{const.} \tag{5.1}$$

In this expression, z is the height above the slab, n_b is the charge density as projected on the states with energies within V_b from the Fermi energy, Φ is the work function, R is an estimate of the tip curvature radius, and $k = \sqrt{2m_e}/\hbar$. The constant value is set to the value of this expression at the center of the mesh at the height z where the projected density is equal to 10^{-6} electrons/a_0^3. By mapping the electrostatic potential on the obtained isocurrent surface, also the experimental dI/dz map can be reproduced and regions with higher or lower work function can be distinguished.

5.2 Bare nanomesh

It has already been shown in previous works[20, 29, 30, 87] that the lattice mismatch between h-BN (a_0=2.5Å) and Rh(111) (a_0=2.688Å) does not allow a one to one epitaxial growth of h-BN. Coincidence superstructures are formed, instead, with large lattice constants, where the unit cell is a 13 × 13 h-BN on 12 × 12 Rh(111). Indeed, the energy payed to stretch the BN bond and match the Rh(111) lattice could not be compensated by the binding to the metal. For free-standing, flat h-BN, we estimate this stretching energy to be more than 0.4 eV per BN pair. On the contrary, the 13 × 13 h-BN on 12 × 12 Rh(111) superstructure corresponds to an overall contraction of the

for a total of 1008 atoms, using the experimental lattice constant, 3.8 Å.

BN bonds, from 1.45 Å to 1.43 Å (1.4%), with an energy cost of only 0.02 eV per pair.

In order to investigate the properties of the nanomesh, we considered model systems of different size. Preliminary calculations have been carried out with small Rh slabs, constituted of seven 6 × 6 Rh(111) layers, terminated by stretched and flat 6 × 6 *h*-BN monolayers on both sides. The lattice parameter for the Rh slabs is set to the experimentally determined value of 3.8 Å. Optimal binding conditions are obtained when N occupies atop sites and B fcc hollow sites. In this case, the *h*-BN monolayer remains flat, at about 2.18 Å over the Rh surface. The interaction with the metal induces the buckling of the BN pairs, with B atoms 0.14 Å closer to the slab surface. The interpretation of the electronic structure through the MLWF representation confirms the presence of binding interaction. For free-standing *h*-BN, three MLWF per BN pair are centered along the BN bonds, while a fourth orbital is associated to the lone pair, whose center is very close to the N. On the metal instead, when N occupies the atop site, the lone pair center is clearly displaced into the interlayer region, thus revealing the polarization of the electronic charge due to the interaction with the metal. As a consequence, the *h*-BN monolayer is positively charged and the work function is 3.7 eV, i.e. 1.4 eV smaller than the work function of clean Rh(111). The binding energy calculated with respect to the stretched, free-standing *h*-BN is -0.6 eV per pair, whereas the adsorption energy, i.e. the energy gain with respect to free-standing *h*-BN at equilibrium, is only -0.14 eV per pair. No binding interaction is observed, instead, when N occupies hollow sites. In the optimized configuration, obtained by laterally constraining the overlayers, *h*-BN remains at more than 2.6 Å from the slab surface. Also the electronic structure of the *h*-BN monolayer is not significantly modified by the presence of the metal, as demonstrated by the fact that all the MLWF associated to BN are centered within the BN plane.

The nanomesh is obtained by employing metallic slabs with seven or four 12 × 12 Rh(111) layers. The largest system with seven Rh layers is a symmetric slab terminated on both sides by a 13 × 13 *h*-BN. The structure optimization is carried out relaxing all the degrees of freedom. This sample contains 1008 Rh atoms and 338 BN pairs, corresponding to 19840 valence electrons and 34996 basis functions. The smaller model with only four layers is surmounted by one monolayer on one side only, while the Rh atoms of the bottom layer, on the opposite side, are kept fixed at the bulk positions. This model is used for most of the calculations including also water molecules (the last two Rh layers are fixed in the water system), because of the reduced computational costs; it consists of 576 Rh atoms and 169 BN pairs, corresponding to 11144 valence electrons and 19370 basis functions. It has

been verified that the nanomesh properties remain mostly unchanged using the smaller system.

The structure optimization is started from a slightly contracted and flat 13 × 13 *h*-BN, in order to match the 12 × 12 Rh(111) box dimensions. The monolayer is initially located at about 2.5 Å from the Rh surface. The initial Moiré structure is characterized by regions where the N atoms occupy atop sites, i.e. directly on top of Rh atoms, and other regions where they occupy hollow sites, i.e. hcp site on top of an atom of the second Rh layer, or fcc site on top of an atom of the third layer.

Through the optimization of the 13 × 13 *h*-BN on 12 × 12 Rh(111), the expected corrugated structure is obtained. Two approximatively flat regions are clearly distinguished; The pore, where the layer is closer to the metal and the N atoms tend to occupy atop sites, and the wire, about 1 Å more distant from the slab. Figure 5.1**a** reproduces a top view of the replicated corrugated *h*-BN, where the atoms are colored according to their height above the slab. The pore lays at about 2.2 Å from Rh(111) and corresponds to about 30% of the monolayer. Bonding interactions between N and Rh are obtained by the re-hybridization of the p lone pairs of N with the d band of Rh. The redistribution of electronic charge is also indicated by the displacement towards the metal of the MLWF centers corresponding to the N lone pairs (see in Figure 5.2**b**). The BN bonds tend to be longer, with average length of 1.46 Å corresponding to a NN distance of 2.53 Å. This elongation favors the effective binding to the metal. For the same reason, the Rh atoms beneath the pore get closer (2.67 Å). The wire lays at about 3.1 Å from Rh and involves more than 50% of the monolayer. The interaction between wire and Rh is weak and dominated by the dispersion contributions, and the boron-nitride electronic charge is not significantly perturbed by the presence of the metal. The average BN bond length here is 1.43 Å or even shorter, to compensate the elongation observed in the pore. The remaining part of the monolayer, 10–15%, forms the intermediate rim that connects pore and wire. The steep change in height, about 1 Å involves only two atomic rows. Figure 5.1**b** is a top view of the N lattice that are colored according to the average length of the three BN bonds, thus providing a colored map of the bond length distribution. The map of the height distribution and the map of bond length distribution display quite similar patterns, thus confirming the direct relationship between N binding to the metal and BN bond stretching.

As already mentioned, the strong binding between metal and BN occurs in the pore region only, where the electronic charge of the nitrogen lone pair is polarized towards the metal. A clear picture of the electronic charge redistribution associated with the binding at the interface is given in Figure 5.2**a**, where the charge density difference $\Delta n(\mathbf{r})$ is displayed. Modification of

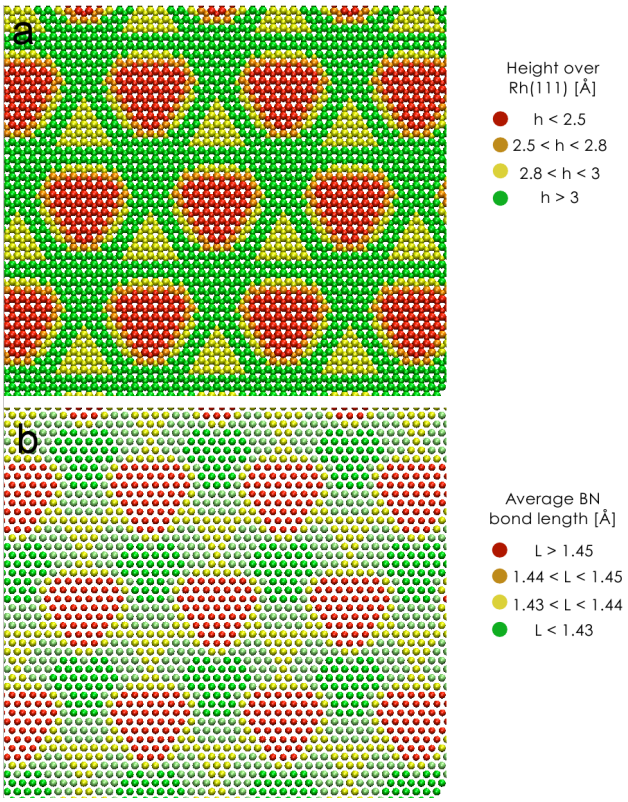

Figure 5.1: **a**. Top view of the replicated corrugated h-BN colored according to the height above the Rh(111) surface. **b**. Top view of the N lattice colored according to the average length of the three BN bonds. The equilibrium lattice constant of free-standing BN by employing our simulation set-up is 2.517 Å, which corresponds to BN bond length of 1.453 Å. In order to prepare the 13-on-12 interface, the equilibrium lattice constant of Rh has been used, i.e. $a = 3.801$ Å for the fcc lattice corresponding to 2.688 Å for the hexagonal lattice of the Rh(111) surface. The 13×13 overlayer is initially flat and the overall BN bond length needs to be slightly contracted, being 1.432 Å. This contraction on a flat free-standing BN layer costs 0.024 eV per BN pair. After the optimization of the h-BN/Rh interface, the overlayer is corrugated and the contraction is partially released, since in some regions the bonds get closer to the equilibrium length. On the other hand, the corrugation of the flat layer corresponds to an energy cost equal to 0.037 eV per BN pair.

the charge density due to the interaction are visible only directly below the pore. In the interstitial region we have accumulation of charge coming from the N lone pair and the interfacial Rh layer, thus indicating hybridization of the p states of N with the metallic d band. All over the rest of the systems

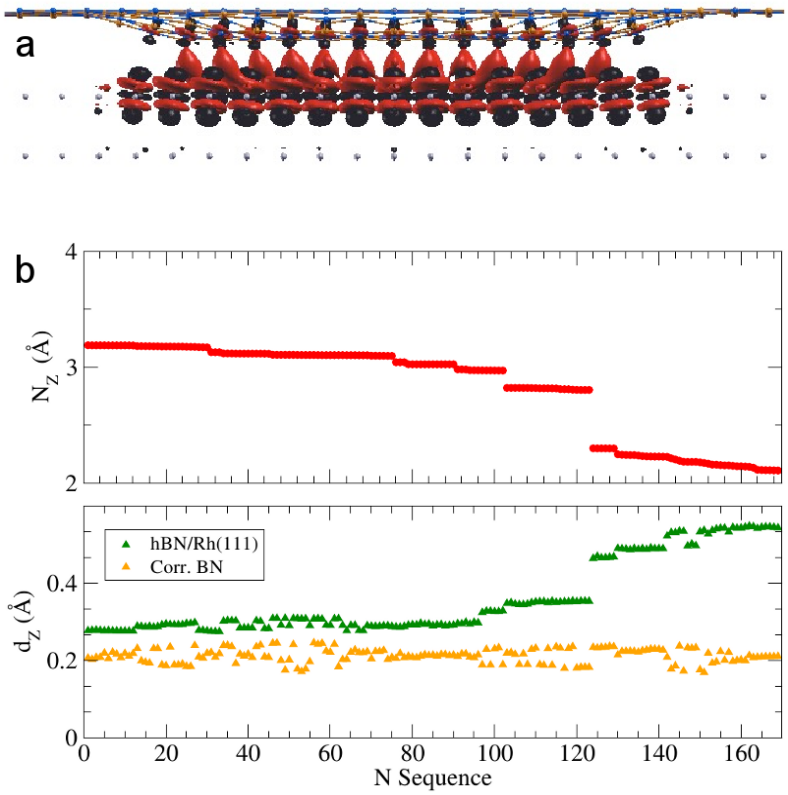

Figure 5.2: **a**. Computed adsorption induced charge density difference for the nanomesh on the 7-layer Rh(111) slab. The picture shows the electronic isosurface at 0.005 electrons/a_0^3, where red indicates accumulation of charge and black stands for depletion of charge. **b**. Distance of the N atoms from the top layer Rh projected along the z axis (upper panel) and corresponding projected distance of the MLWF centers associated to the N lone pair from the N itself. The green triangles indicate the distances computed for the nanomesh, whereas in orange are those computed for the free-standing corrugated BN (lower panel).

the electronic charge distribution remains unperturbed. Also the analysis through the MLWF confirms that strong polarization effects involve only the atoms of the pore. In particular, Figure 5.2**b** shows the projected distance d_z between the center of the lone-pair orbital and the corresponding N atom, as computed for the corrugated h-BN on the metal and for the same corrugated structure free-standing in vacuum. While for the free-standing layer, d_z is uniform all over the monolayer (≈ 0.2 Å), a clear increase is recorded for the full system, when N atoms that are closer to the slab, i.e. belonging to the pore. No significant variations have been observed, instead, in the position of

the centers of the orbitals along the BN bonds. Hence, the binding is provided by the interaction between N and Rh in the pore through the hybridization of the N lone pair orbitals, with charge polarization towards the metal.

The adsorption energy is computed as $E_{h\text{-BN/Rh(111)}} - E_{h\text{-BN}} - E_{Rh(111)}$, where $E_{h\text{-BN}}$ is the equilibrium energy of free-standing h-BN, and $E_{Rh(111)}$ is the energy of the relaxed metallic slab. For the large sample with seven layers, we get -0.33 eV per BN pair [2]. The interaction energy, i.e. $E_{h\text{-BN/Rh(111)}} - E'_{h\text{-BN}} - E'_{Rh(111)}$, where $E'_{h\text{-BN}}$ is the energy of the free-standing corrugated h-BN and $E'_{Rh(111)}$ is the energy of the corrugated Rh(111) slab, is -0.39 eV per pair. This latter quantity estimates the pure binding interaction of h-BN with the metal, since the energy costs associated with the contraction, 0.02 eV per BN pair, and the corrugation, 0.04 eV per BN pair, are not subtracted.

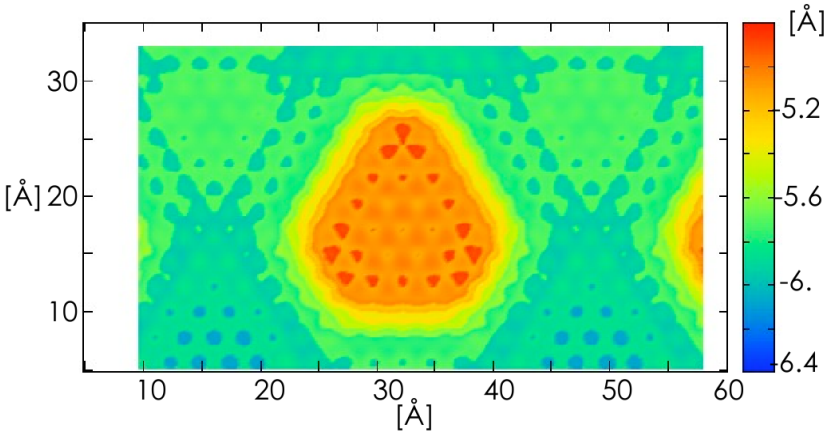

Figure 5.3: Calculated STM topography for nanomesh, using a bias potential equal to -0.1 eV and $R = 2$ Å.

In Figure 5.3 we report the STM topography, calculated as isocurrent surface (see expression 5.1), obtained with a bias potential of -0.1 eV and $R = 2$ Å. The pore appears as hexagonal depression, 5.2 Å above the slab, i.e. 3 Å above the N atoms. The STM corrugation between pore and wire

[2] It is interesting to notice that by displacing h-BN relative to Rh(111), we could optimize structures with slightly different geometries within the pore, even if the corresponding differences in adsorption energy are smaller than 0.01 eV per BN. In particular, the pore with N-top and B-fcc is lower in energy than the N-top and B-hcp configuration, while the structure with pore centered on three equivalent atop N atoms is 0.01 eV per BN pair lower in energy than the structure with pore centered on one N only. In all cases height distribution over Rh, the extension of the pore, as well as the electronic properties do not present significant differences.

is about 0.8 Å. From the map of the electrostatic potential computed on this same isocurrent surface, the work function variation between pore and wire is 0.5 eV (see Figure 5.4). This can be directly compared to the dI/dz maps reported in experimental work[21]. The modulation of the electrostatic potential, i.e. of the work function, is a direct consequence of the charge density polarization in the pore. Calculating the potential on a plane cutting through the nanomesh, and perpendicularly to the slab, the estimate of variation between higher values above the wire and lower values above the pore is of about 0.6 eV (Figure 5.5). This feature of the nanomesh is of particular interest, because such gradient in the electrostatic potential may act as a trapping well for adsorbed molecules. It is also worth to notice that a modulation of about the same amount is present above the corrugated, free-standing *h*-BN, but it is inverted, being the potential higher over the pore.

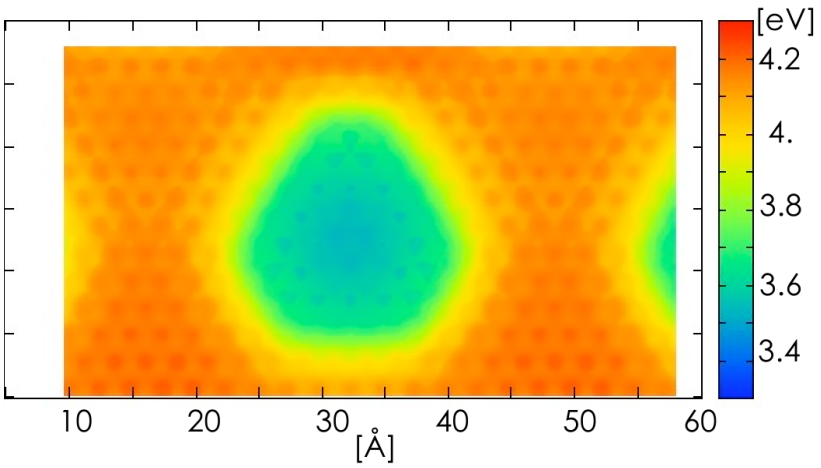

Figure 5.4: Work function map obtained from the electrostatic potential of the nanomesh as computed on the same isocurrent surface generated to reproduce the STM topography (see Figure 5.3).

Finally, the density of states projected on the N_{p_x} states presents clear features related to the presence of non-equivalent N atoms, i.e. atoms that bind directly to the metal and others only weakly interacting with the slab. Projecting the DOS only on the N atoms in the pore or only on the N atoms of the wire region, the specific features associated to each type can be identified. In particular, two bands about 6 eV below the Fermi energy and separated by about $\sim$1 eV are distinguished (see Figure 5.6), in agreement with experiment and previous calculations [11, 29, 30, 87].

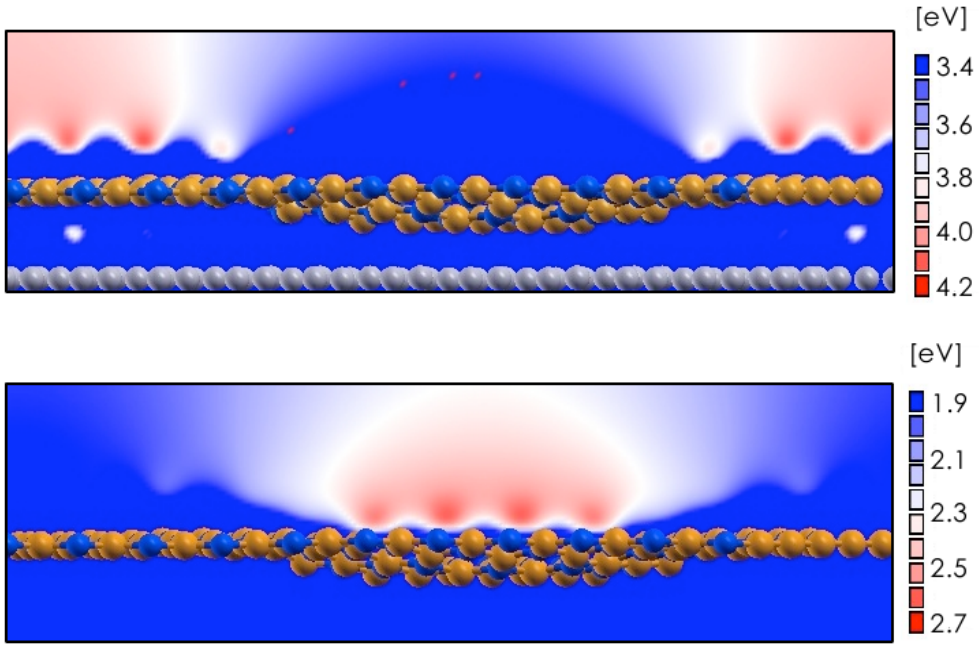

Figure 5.5: Cut of the electrostatic potential through the center of the pore. The top panel displays the cut taken from the nanomesh over the seven layer Rh(111) slab. The bottom panel shows the cut of electrostatic potential generated by the free-standing BN at the same geometry of the combined system.

5.3 Nanomesh with water deposition

5.3.1 Free BN

In order to identify the water aggregates that are observed in the experiment as three protrusions of the STM topography, several water clusters have been investigated.

First, the structures of water aggregates, from the monomer to different possible isomers of the hexamer, have been optimized on a flat, free-standing 8×8 BN monolayer, comparing different possible adsorption sites. In all the studied cases, we observe that the binding to BN is rather weak (on average less than -0.16 eV per molecule) and the H-bond interactions (OH$\cdots$O) between the molecules themselves are dominant.

The interaction with the substrate occurs mainly through H-bonds of the type OH$\cdots$N. In Table 5.1, the adsorption energy per H_2O molecule is given with respect to the same cluster (c_N) optimized in vacuum, $E_{ad} = (E_{tot} - E_{h\text{-BN/Rh(111)}} - E_{c_N})/N$. The remaining table columns report the

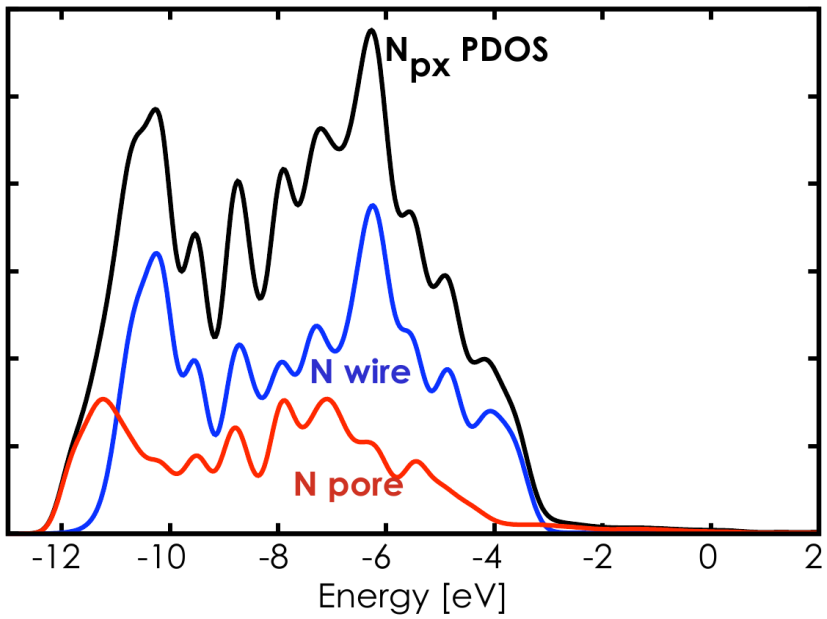

Figure 5.6: Projected Density of states(DOS) on N_{px} (black), only on the N atoms in the pore (red) and on the wire (blue).

number of H-bonds of type OH$\cdots$O and OH$\cdots$N, as well as their average length, for the most stable configurations of each cluster type.

This first set of calculations confirms that water molecules deposited on BN tend to pack in order to maximize the number of internal H-bonds. The resulting nearest OO distance is typically about 2.7 Å, i.e. much shorter than the distance measured between the STM protrusions. However, in the case of the regular hexamer, selecting every second molecule of the ring, the O atoms form an almost equilateral triangle, where the OO distance is ≈4.6 Å. This picture approximatively matches with the triangle formed by the three STM protrusions in the pore. The hexamer seems also to be the optimal building block for aggregation of water molecules on BN. Indeed, by adding one molecule close to the hexamer, it binds to the ring through a H-bond, but remaining only externally attached. The most stable structure of the hexamer on BN is the regular hexamer, placed parallel to the layer at a distance of about 3.3 Å. It is characterized by three molecules (position 1, 3, and 5 in the ring) forming one strong OH$\cdots$O H-bond (1.72 Å) with the next molecule in the ring and one weak OH$\cdots$N H-bond with the closest N atom (2.38 Å). The other three molecules form only one OH$\cdots$O H-bond, while their second hydrogen is dangling outward (with respect to BN). The O atoms with one dangling hydrogen are slightly higher over the BN plane (O buckling

Table 5.1: Water clusters[a] adsorbed on free-standing BN: adsorption energy, number and average length of hydrogen bonds

	E_{ad}	OH$\cdots$O		OH$\cdots$N	
	[eV/H_2O]	n	$\bar{d}$ [Å]	n	$\bar{d}$ [Å]
monomer[b]	-0.158	-	-	2	2.57
dimer[b]	-0.137	1	1.94	2	2.54
trimer	-0.108	3	1.95	2	2.45
tetramer	-0.093	4	1.77	2	2.57
pentamer	-0.096	5	1.73	3	2.50
hexamer	-0.086	6	1.71	3	2.38

[a] The energy gain due to the formation of the H-bonds within the cluster is defined by $E_{c_N}/N - E_{monomer}$, and corresponds to -0.10 eV/H_2O for the dimer, -0.21 eV/H_2O for the trimer, -0.29 eV/H_2O for the tetramer, -0.30 eV/H_2O for the pentamer, and -0.31 eV/H_2O for the hexamer.

[b] Other possible adsorption configurations for the water monomer and the water dimer involve the formation of only one OH$\cdots$N H-bond, with a length of 2.42 Å and 2.40 Å for monomer and dimer, respectively. The water molecules are about 0.1 Å closer to BN, and E_{ad} differ by only 0.001 eV/H_2O.

of 0.14 Å). It is worth noting that the regular hexamer also corresponds to the lowest dipole moment, since the molecular dipoles optimally compensate each other within the ring geometry. From the MLWF analysis, a total cluster dipole of 0.386 D has been calculated. By displacing the cluster parallel to the BN plane, it is possible to find alternative stable configurations, where the OH$\cdots$N are re-oriented by switching to a different neighboring N. Hence, several possible configurations of the hexamer can be optimized, which differ for the relative position with respect to the BN layer and for the length and orientation of OH$\cdots$N. These differences may induce small deformations of the hexamer, which can be quantified in terms of the chirality defined as

$$\xi = \frac{|(a-b)(b-c)(c-a)|}{(a+b+c)^3} \tag{5.2}$$

where a,b,c are the distances between two second neighbor oxygen atoms (i.e. those forming the triangle)[22]. The corresponding changes in adsorption energy are also small, i.e. less than 0.01 eV per H_2O. By running molecular dynamics (MD) simulations at relatively low temperature, 150 K, the easy

switching of the H-bond from one N to the next turns out to favor the free diffusion of the hexamer parallel to h-BN.[3]

We observe that the hexamer moves by undergoing structural distortions when one switching process occurs, but always keeping its two dimensional hexagonal form. Along the MD trajectory, the six OH$\cdots$O H-bonds are stable and prove to be quite rigid, allowing thermal fluctuations of OO distances of about 0.3 Å. The molecules binding to the substrate keep always the same orientation, i.e. with one H pointing to the layer and one to the next molecule of the ring. The dangling hydrogen of the other three molecules, instead, is free to rotate, taking outward, parallel, and inward positions.

5.3.2 *h*-BN/Rh(111)

Next we study some water aggregates on the nanomesh formed by the 13 $\times$ 13 BN on a 4-layer 12 $\times$ 12 Rh(111) slab, collocating a few water molecules in the pore or on the wire. As already described above, the BN electronic charge distribution in the pore is modified due to the binding interactions between N and Rh, making the N atoms more positively charged. On the other hand, the modulation of the electrostatic potential due to the corrugation may act as a trapping potential well. We want to understand how the corrugation may affect the properties of the adsorbed clusters, and compare the simulated STM images to the experimental data to give hints on the observed structures. In Table 5.2, we report the adsorption energy, the number and the average length of the H-bonds calculated for the optimized clusters.

The water monomer optimized in the pore does not form any OH$\cdots$N bonds. On the contrary, the negative charge of the O lone pair is attracted by electron-deficient B atoms and the OB distance is 3.02 Å. As a consequence, the two OH are one pointing outward and the other parallel to the surface. On the wire, the adsorption pattern of the water monomer is more similar to the binding on a flat BN surface. One of the proton is pointing to the N atom, forming a OH$\cdots$N bond 2.42 Å long. The other OH is parallel to the surface. Despite the two structure optimizations have been initiated from the same geometry, two different configurations are obtained. This difference can be explained considering the polarization of the lone pair of the nitrogen in the pore, thus leaving less negative charge on the BN surface, which could not stabilize the proton. The water monomer is stable also close to the rim of the nanomesh, where one proton points to the nearby nitrogen, forming a

[3]Ab initio MD simulations are performed in the canonical ensemble by applying the Nose-Hoover thermostat. The integration of the equations of motion is performed through a velocity Verlet algorithm. Between two MD steps, the density matrix is reinitialized using the älways stable predictor-correctorëxtrapolation scheme.

Table 5.2: Water clusters on nanomesh: adsorption energy, number and average lengths of hydrogen bonds

	E_{ad}	OH$\cdots$O		OH$\cdots$N	
	[eV/H_2O]	n	$\bar{d}$ [Å]	n	$\bar{d}$ [Å]
monomer(pore)	-0.146	-	-	-	-
monomer(wire)	-0.118	-	-	1	2.42
monomer(rim)	-0.196	-	-	1	2.35
dimer(pore)	-0.151	1	1.92	2	2.50
dimer(wire)	-0.142	1	1.93	2	2.53
trimer(pore)	-0.125	3	1.93	1	2.25
hexamer(pore)	-0.117	6	1.73	3	2.52
hexamer(wire)	-0.095	6	1.73	3	2.45
hexamer(rim)	-0.106	6	1.72	3	2.41

OH$\cdots$N H-bond 2.35 Å long. The other OH, instead, points outwards. The O atom is almost on top of the boron, and the OB distance is 3.14 Å. Because of the attractions between the oxygen and boron, and the formation of the OH$\cdots$N H-bond, this structure has a lower adsorption energy compared to the two other adsorption sites. Starting from an initial position exactly on the rim, where the electrostatic potential has a gradient, we observe that during the optimization the water monomer moves closer to the center of the pore. However, it could keep the H-bond to the same nitrogen during the optimization, and once the oxygen is on top of the boron atom, it stays there. The further sliding towards the pore would require an activation energy to break this H-bond. Being this a weak interaction, we expect that at finite temperature the molecule would easily move towards the center of pore, where the electrostatic potential has its minimum.

Things change for the water dimer in the pore. The H-bond donor oxygen is not forming H-bonds to the surface, i.e. its dangling H points outwards, while the negatively charged lone pair is closer to the surface. The other oxygen, instead, offers its lone pair to form the OH$\cdots$O H-bond, while the positively charged protons point to two different N, forming weak H-bonds with NH length of 2.49 and 2.51 Å. The water dimer adsorbed on the wire shows a very similar configuration as in the pore.

The STM topography calculated for the sample with the monomer in the pore and the one with the dimer in the pore shows that water molecules differently oriented with respect to the surface generate pretty dissimilar images. Namely, the STM simulations are carried out with a negative biasing

potential, i.e. we sample the occupied states close to the Fermi energy. Hence, the electronic cloud of the oxygen lone pair sticks out, when it is not hidden by other parts of the molecule. As a result, in the STM image generated for the water monomer (Figure 5.7**a**), where the lone pair is closer to the surface and the OH point outwards, no protrusion is appearing. In the case of the dimer, instead, we clearly distinguish one protrusion, as displayed in Figure 5.7**b**, corresponding to the oxygen of the acceptor molecule, i.e. the one forming the OH$\cdots$N H-bonds. According to this picture, the STM may provide more information than expected on the configuration of water aggregates, discriminating among molecules, depending on the position of the hydrogens. It also indicates that the three protrusions observed in the experiment should not be associated to three water monomers.

To rule out the possibility that three separated monomers, about 4.6 Å distant from each other, may be stabilized in the pore and generate the three protrusion image, three molecules have been placed in such configuration and then the structure has been optimized. The optimization brings the three molecules together, to form a trimer, where three OH$\cdots$O H-bonds are formed, and the average OO distance is 2.84 Å. In the final configuration, only one molecule forms a OH$\cdots$N H-bond to the surface, which is 2.25 Å long. The second H of the other two molecules, instead, is dangling and pointing outwards. Hence, while the dimer forms two OH$\cdots$N bonds, with distances of 2.50 Å, the trimer has only one of such interactions. That's the reason why the binding divided by the number of water molecules for the water trimer is much weaker as compared to the dimer. The STM topography calculated for the trimer shows only one protrusion, corresponding to the only molecule with no dangling H and with exposed lone pair (Figure 5.7**c**).

The hexamer optimized in the pore forms three OH$\cdots$N of length 2.46, 2.54 and 2.55 Å, while the average OH$\cdots$O distance is 1.73 Å. Although the hexamer is not perfectly symmetric after geometry optimization, the difference of the OO distance is relatively small. The atomic OO distances among the pointing-down water molecules are 4.68, 4.71 and 4.76 Å, corresponding to chirality $\xi = 4.97 \times 10^{-8}$. The distances between the other three molecules are 4.68, 4.71 and 4.77 Å. The corresponding STM image, as reported in Figure 5.8**a**, shows three protrusions at distances 4.95, 4.97, and 4.99 Å, i.e. with very little distortion with respect to an equilateral triangle. The chirality ξ_{STM}, as computed with respect to the centers of the three spots, is 4.93×10^{-9}, i.e. considerably smaller than the average chirality measured from the experimental STM images. The influence of the Rh layers on the electronic structure of the water hexamer is relatively small. In Table 5.3 we report the dipole values calculated for the water hexamer in the pore of the nanomesh, on the wire, and in the pore of free-standing,

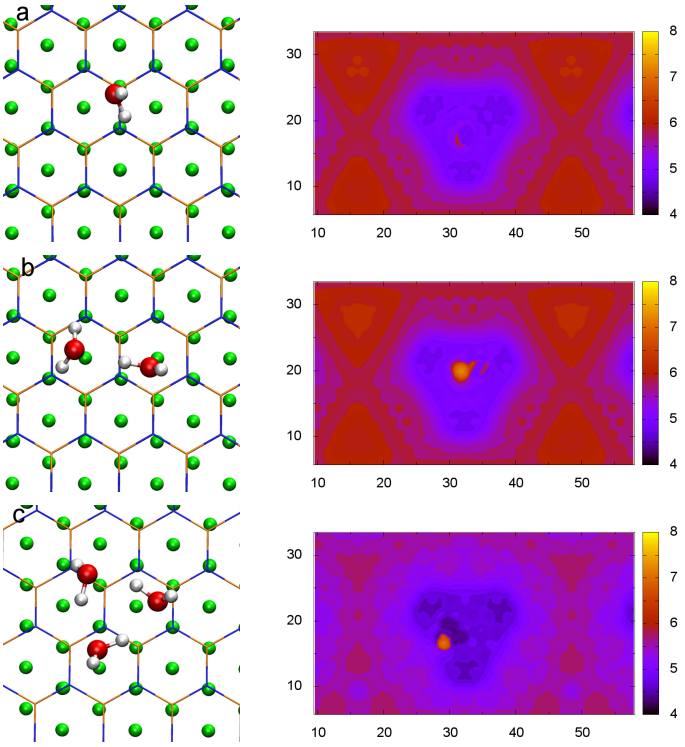

Figure 5.7: Top view of the water cluster structures within the pore of the nanomesh (left) and corresponding STM topography images (right). In the ball and stick representation of the structure, the red and white spheres are oxygen and hydrogen atoms, respectively, the BN monolayer is given by the thin lines forming the honey-comb lattice, where blue stands for nitrogen and orange for boron, the green spheres in the background are the Rh atoms of the slab. The STM images are generated using a bias potential of -0.1 eV and $R = 4$ Å; the units for both mesh and height are Å. **a**. water monomer; **b**. water dimer; **c**. water trimer.

corrugated BN. We find that without the metal the dipole is 0.118 Debye, i.e. smaller than the 0.724 Debye computed in the pore of h-BN/Rh(111). However, in all cases, the dipole moments are quite small in all directions.

The hexamer can be optimized in a stable configuration also on the wire. Here, it forms three OH$\cdots$N H-bonds of length 2.36, 2.45, and 2.54 Å, which are in average shorter than in the pore as the nitrogen atoms on the wire are more negatively charged. The average OO distance is 2.73 Å, i.e. very close to the value calculated for the water hexamer in the pore. The OO distances between the water molecules pointing down are 4.66, 4,71 and 4.85 Å, corresponding to chirality $\xi = 3.88 \times 10^{-7}$. The hexamer optimized on the

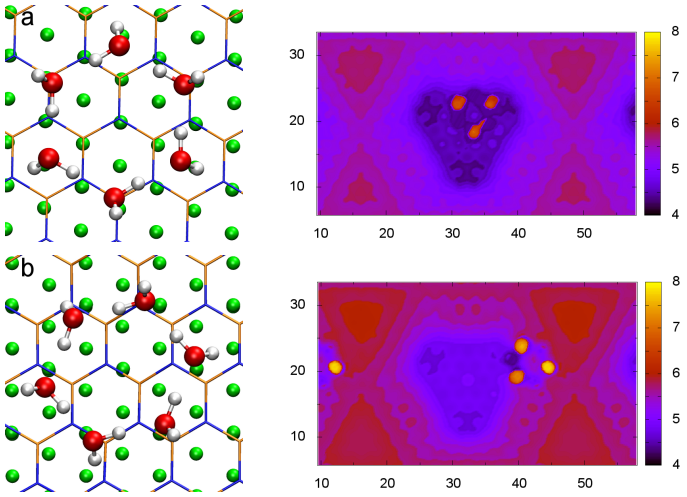

Figure 5.8: Top view of the water hexamer within the pore of the nanomesh (**a**) and at the rim (**b**). See caption of Figure 5.7

Table 5.3: Values of the dipole moment along the three Cartesian directions, computed for the water hexamer above the free-standing corrugated BN and above the nanomesh. The dipole moments are obtained from the positions of the atomic nuclei and of the centers of the MLWF

	Dipole Moment (Debye)			
	μ_x	μ_y	μ_z	$\lvert\mu\rvert$
hex_corrugated BN	0.038	-0.111	-0.011	0.118
hex_pore	-0.0105	-0.133	-0.712	0.724
hex_wire	0.027	-0.200	-0.133	0.242

wire is only 0.02 eV per water molecule less binding than in the pore, showing a preference of this cluster to be adsorbed in the pore. However, we already observed that such small variations in binding energy can be obtained by moving or distorting the hexamer just a little, so that the H-bond to the substrate switch from one to another N atom and are partially re-oriented.

According to these results, STM does not detect all the O present in the pore as protrusions. Our study suggests that the most frequently observed cluster could be the cyclic water hexamer, where every second molecule is oriented inward, i.e. H-bonded to the surface, and therefore can be seen as protrusion in the topography. However, most of the experimental three protrusion images are characterized by a quite larger chirality, with the magnitudes of 10^{-6} to 10^{-4}[22]. One possible origin of this distortion is the

presence in the pore of other molecules interacting with the hexamer, but not visible for the STM, or even the interaction of the tip of the microscope. We are not going to explore these possibilities in this work, but we consider the effect of the rim and of small displacements of the hexamer with respect to the substrate.

By placing the hexamer over the rim of the nanomesh, the optimized structure has still three molecules binding to the surface by OH$\cdots$N interactions, and the triangle formed by the three oxygens is indeed more distorted, with OO distances of 4.56, 4.84 and 4.70 Å, and $\xi = 2.06 \times 10^{-6}$. In contrast to the hexamer in the pore, on the rim the height of the molecules variates by about 1 Å, following the corrugation of the BN layer to better orient the OH and optimize the OH$\cdots$N binding. The resulting three OH$\cdots$N H-bonds have lengths of 3.24, 3.27 and 3.41 Å, i.e. tendentially shorter than in the pore, thus explaining the similar adsorption energy, -0.106 eV per water molecule, in spite of the distortion. The distortion is also visible in STM image (shown in Figure 5.8**b**), where the three protrusions are at distances 4.82, 5.02 and 5.24 Å, and ξ_{STM} is 5.37 $\times 10^{-6}$. The fact that the water hexamer might also be adsorbed at the rim of the nanomesh is consistent with experiment, where water aggregates generating three protrusions close to the rim have been observed. The chirality of the calculated geometry, however, is still smaller than the one resulting from the experimental image.

From the MD trajectory of the hexamer on flat BN, we selected two configurations of the cluster that turn out to be stable, in spite of the larger distortion of the ring. The distortion occurs when the cluster is diffusing over the monolayer and, in order to favor the formation of the OH$\cdots$N H-bond, one or two molecules of the ring are displaced to reach for nitrogens that are farther apart. This condition is also associated with a larger angle formed by the OH with respect to the normal of the BN plane. The two selected geometries optimized on the flat BN correspond to a chirality of 9.63 $\times 10^{-8}$ and 2.44 $\times 10^{-6}$, respectively. We expect that the same geometry should generate even more distorted STM images once located in the pore of the nanomesh, because the position of the protrusions depends also on the orientation of the OH bond pointing to the substrate. Then, we have tried to reproduce the same configurations on nanomesh, choosing a location that could preserve as much as possible the same distances between atoms of the cluster and atoms of the substrate. Without performing any structure optimization, we have computed the STM topography for the frozen configurations and, as expected, asymmetric STM images are obtained. As expected, the distortion given by the protrusions is significantly larger, corresponding to chirality 1.23 $\times 10^{-6}$ and 6.54 $\times 10^{-7}$. Further investigation of the interaction between water and the nanomesh should consider the dynamics of the clus-

ters on the full substrate, in order to address the formation of the aggregates and their diffusivity at finite temperature. In particular, we are interested in comparing the diffusivity in the pore and on the wire, because we believe that the fact that these structures are always observed in the pore is due to the trapping effect of the electrostatic potential well as determined by the corrugation. It is important to remark, that all these cluster lay quite high above the substrate, with the O atoms about 3 Å distant from the BN plane. This means that the water molecules above the pore are higher than the wire, and their movement cannot be hindered by the structural corrugation (only 1 Å). These and other aspects related to the dynamics of water on the nanomesh will be the subject of future work.

5.4 Conclusion

We presented a DFT study of the *h*-BN nanomesh, showing that our model for this complex interface system is in very good agreement with the experimental observation. Our simulations reproduce the corrugated BN on Rh(111) without the need of imposing any constraint to the system, giving values of the STM corrugation and of the variation of the work function very close to what is measured in experiment. Charge density differences and MLWF analysis show that binding between the *h*-BN and Rh(111) is present only within the pore region, elsewhere the interaction is dominated by dispersion forces. In particular, comparing the electronic structure and the modulation of the electrostatic potential of the nanomesh to what obtained for the corrugated free-standing BN suggests that the polarization effects induced by the interaction with the metal are crucial in determining the right environment to trap molecules in the pore.

Motivated by recent experimental results showing the formation of stable structures by dosing water to the nanomesh, we extended our investigation to the interaction of the nanomesh with water molecules and small water clusters. From our geometry optimization and the STM image calculations, we conclude that the frequently observed three protrusion images are related to the presence of hexamer clusters trapped in the pore. The distance between the protrusions and the fact that only certain molecules appear in the STM topography, leads us to exclude that these images could be associated to a water trimer. Since the STM topography highlights those molecules exposing the negatively charged O lone pair, we cannot rule out the existence of more water molecules in the pore. However, our results suggest that the smallest aggregate that can give rise to the characteristic three protrusion image is most probably the water hexamer. Besides, the geometry optimization of

a seventh water molecule added to the water hexamer on a flat BN surface didn't break the cyclic H-bond structure of the water hexamer. We cannot reproduce the strong distortion of the triangle formed by the three protrusions that is often observed in experimental STM images. Possible causes of the distortion that are not taken into account in the present study are the presence of more molecules in the pore, effects of the interaction with the tip, or even entropic contribution that might stabilize distorted structures. All the evidence, however, seems to indicate that when small amount of water is dosed to the nanomesh, the three spot image associated to the water hexamer is the most favorable pattern. This work provides important hints about the structure of the water clusters in the pore and on the interpretation of the STM images. As indicated by our MD simulations of the water hexamer over the free-standing flat BN, it's quite possible that weakly bonded molecules easily diffuse over the flat wire. In this case, their aggregation might be hindered, or anyway the detection by STM of moving aggregates is not possible. On the other hand, within the pore the diffusivity might be substantially reduced due to the trapping effect of the modulated electrostatic potential. Much is still to be understood about the properties and dynamics of water aggregates on the nanomesh. We plan to continue our research on this topic by extending our study to molecular dynamics simulations that reproduce the important processes associated with these systems.

Chapter 6

Nano-ice Models for the Water Aggregates Observed on the Nanomesh

When a large amount of water is deposited onto the bare h-BN/Rh(111) nanomesh, the formation of ordered and stable nano-ice crystals in the pores has been experimentally observed. The present chapter proposes different possible models for the structure of the observed clusters, based on density functional theory calculations of two dimensional water lattices adsorbed on free-standing hexagonal BN. Through the investigation of the electronic properties, the interaction with BN, and the distribution of the molecular dipoles, the most probable two-dimensional arrangement has been identified. Finally, a model is proposed for the nano-ice cluster trapped in the pore of the nanomesh, which is constituted of 38 molecules distributed according to the most probable two-dimensional arrangement on free-standing BN. Structural and electronic properties of the optimized nano-ice cluster are also reported, and it is shown that the model is consistent with the experimental observation.

6.1 Method

In this chapter, we propose different possible models for the two-dimensional water array, which can reproduce the structural features observed from experiment, and we investigate their properties and relative stability. As a first step, we consider simple systems constituted of a flat and free-standing h-BN layer fully covered by the water array. According to the experimental observation[21], the water lattice has to be honeycomb-like with two sublat-

tices, the O-O second neighbor distance has to be close to the one characteristic of hexagonal ice, i.e. 4.6 Å. The structural optimizations starting from different initial configurations have revealed quite a number of possible stable arrays, which differ in the location of the molecules over the substrate, the height of the overlayer, the corrugation defined as the height difference between the two sublattices, the relative orientation of the water molecules, and the distribution of the H-bonds. Finally, from the analysis of the optimized models, we could identify the best candidate to reproduce the nano-ice cluster observed by the STM experiments. We report results of the optimization of the selected water cluster constituted of 38 water molecules when it is located within the pore of the full nanomesh substrate. It is shown that the optimized structure agrees with the experimental findings.

All the calculations are carried out with the CP2K program package[75] applying the hybrid Gaussian and plane waves method[76]. We used revPBE[43, 44] for the exchange and correlation functional in all the DFT calculations, and an additional Grimme D2 potential[48] is added in order to include vdW dispersion corrections. GTH pseudopotentials[77, 78, 79] are used to approximate the interaction of the valence electrons with atomic cores. A large core pseudopotential and nine valence electrons with a [2s1p2d] basis set have been used for Rh. Double zeta short range molopt basis sets[80] are employed for B and N, while triple zeta basis sets are used for O and H. For the calculation with the nanomesh, we used a 13 × 13 BN layer with a four-layer 12 × 12 Rh slab, which represents the full unit cell of the nanomesh. Periodic boundary conditions are always applied in the calculations, and all the reported energy differences are corrected for the basis set superposition error (BSSE) using Boys and Bernardi counterpoise method[88]. STM simulations have been carried out within the Tersoff-Hamann approximation[53, 54], following the same procedure described in Ref.[19]. The molecular dipole moments are computed as

$$p = \sum_i q_i^n \mathbf{r}_i^n + \sum_k q_k^w \mathbf{r}_k^w, \tag{6.1}$$

where q^n and $\mathbf{r}^n$ are charge and position of the nuclei, whereas q^w and $\mathbf{r}^w$ are charge (-2e) and position of the center of the MLWF representing the electronic structure of the adsorbed molecules. The MLWF are obtained for each optimized geometry minimizing the total spread of the molecular orbitals[55]. For each water molecule, one MLWF center is located along every OH bond and represents the electron pair, while two more MLWF centers represent the position of the O lone pairs.

The energetics of the optimized structures are compared in terms of the adsorption energy per water molecule E_{ads}, the interaction energy per water

molecule E_{int}, and the hydrogen bonding contribution $E_{\text{H-bond}}$. E_{ads} is defined as the total energy of the optimized structure E_{M} minus the energy of the optimized free-standing BN layer and N-times the energy of one water molecule in gas phase, where N is the number of water molecules in the simulation box, and then divided by N, $E_{\text{ads}} = (E_{\text{M}} - (E_{\text{BN}} + N \times E_{\text{H}_2\text{O}}))/N$. E_{int} is defined as the total energy of the optimized structure minus the energy of the optimized free-standing BN layer and the energy of the optimized free-standing monolayer of water molecules, then divided by N, $E_{\text{int}} = (E_{\text{M}} - (E_{\text{BN}} + E_{\text{iceML}}))/N$. $E_{\text{H-bond}}$ is the difference between E_{ads} and E_{int} divided by $\frac{3}{2}$, since each molecule in the water monolayer forms three H-bonds with neighboring molecules and we need to cancel the double counting by times the factor $\frac{1}{2}$.

6.2 Structural Models on Flat BN

By considering the structural requirements suggested by the experimental analysis, three possible two dimensional arrangements of the water O atoms over the BN layer are proposed. The three resulting oxygen lattices are depicted in Figure 6.1, as model M1, model M2, and model M3. In the figure the red circles and the green diamonds indicate the sublattices A and B, respectively, while the black lines represent the vectors of the hexagonal unit cell.

Model M1 is a $\sqrt{13} \times \sqrt{13}$ structure with 8 atoms per unit cell. One every four O belonging to the sublattice A is located on top of the BN ring-center, whereas in the sublattice B, one every four O occupies a N-top site. The lattice constant is $a_0 = 9.2$ Å, which corresponds to a second neighbor O–O distance of 4.6 Å, while the closest distance is 2.66 Å. The O lattice is rotated with respect to the BN lattice by an angle of 13.9°.

Model M2 is a 2×2 structure, with lattice constant of 5.1 Å and two O per unit cell. It can also be represented by an orthogonal cell, indicated by the dashed magenta lines in Figure 6.1, and containing 4 O atoms. In this configuration, the O–O distances are a bit larger, being 2.95 Å for the first neighbors and 5.1 Å for the second neighbors. The M2 lattice has the same orientation as the BN lattice.

Model M3 is a $\sqrt{3} \times \sqrt{3}$ structure where all the O atoms occupy N-top sites. The unit cell contains two molecules and $a_0 = 4.42$ Å. The smallest orthogonal cell, instead, contains four molecules and is shown in the figure by the magenta lines. The O–O nearest neighbor distance is 2.55 Å and the rotation angle with respect to the BN lattice is of 30°.

The calculations starting from the M1 configuration have been carried

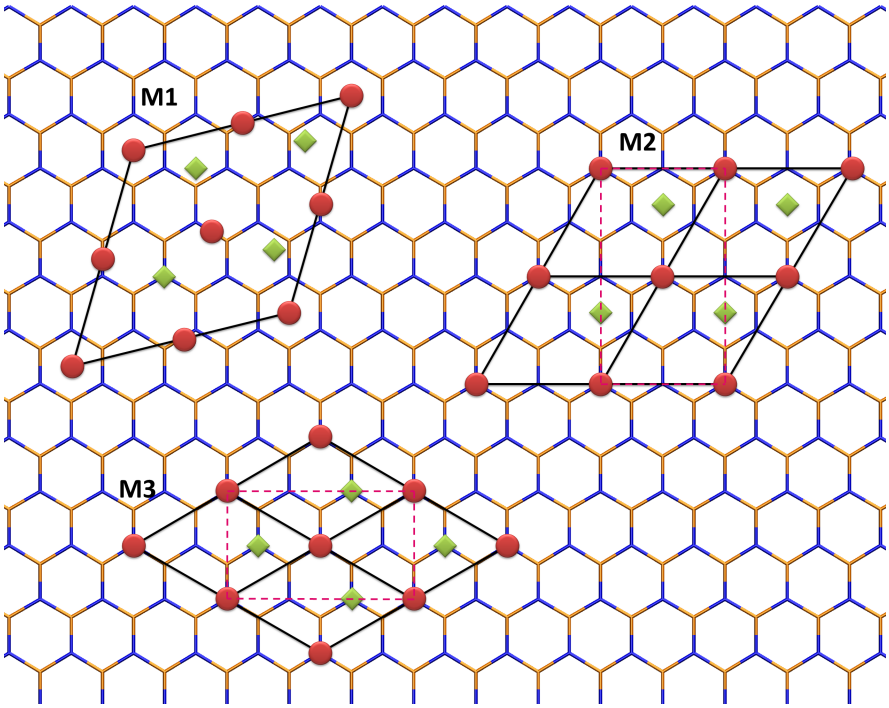

Figure 6.1: Different water cluster lattices. Only the position of the O atoms are considered here and the water molecules are represented by the red circles and green squares as in different water layer. The black lines give the unit cell in each model, while in M2 and M3 the hexagonal unit cells are converted to orthogonal ones as indicated by the magenta dash lines used in the calculations. The thin line in the background are BN monolayer, with B in orange and N in blue.

out using a 3×3 hexagonal supercell containing 72 water molecules. For the other two models, orthorhombic cells have been used. A 4×2 supercell for M2, containing 32 water molecules, and a 3×4 supercell for M3, containing 48 molecules.

The stability and the electronic properties of the water array are expected to be strongly affected by the network of H-bonds interconnecting the molecules. These interactions are by far stronger than the interactions with the substrate. In a three-dimensional water assembly, each molecule has the possibility to form four H-bonds, two as donor molecule, through its own hydrogen atoms, and two as acceptor molecule, providing the O lone pair. This is what happens in the ice hexagonal lattice, where each molecule is tetrahedrally coordinated through the four H-bonds. The network of H-bonds in a two-dimensional water array is such that each molecule is involved in the formation of three H-bonds, as donor and as acceptor. Those H atoms

not involved in inter-molecular bonding either remain dangling or interact with the substrate. How hydrogen and H-bonds are distributed depends on the relative orientation of the molecules and on the corrugation of the layer. In order to minimize the bias of the initial conditions on the final structure, in most of the cases a very unlikely starting orientation of the molecules has been selected, where all the molecules are perpendicular to the substrate, with one OH pointing to it and the second parallel. Afterwards, all the coordinates are relaxed, and the molecules rotate to maximize the intermolecular interaction and stabilize the structure.

For each model, in the initial configuration, the average height of the molecules over the substrate is 3 Å, but different initial height distributions have been tested: all O at the same height (h_0), sublattice A 0.3 Å higher (h_A), or sublattice B 0.3 Å higher (h_B).

6.3 Results and Discussions

6.3.1 Water Monolayer on Free-standing Hexagonal BN

The only stable and ordered 2D array of water molecules with the M1 lattice is obtained by starting from the configuration h_B. As displayed in Figure 6.2**a**, also in the optimized structure, the molecules of sublattice B are slightly higher (yellow O atoms in the figure). They are all parallel to the BN substrate, thus forming three H-bonds with two neighboring molecules of sublattice A. The A molecules are 0.73 Å closer to the substrate and have a different orientation, such that one proton can form a H-bond with a neighboring molecule, while the second H atom is pointing to the BN layer. Effective hydrogen bonding with the substrate is possible only when the molecule is positioned on top of a N atom, and in this case, the O atom is even slightly closer to the BN substrate, i.e. 0.015 Å if compared to molecules above the BN ring-center and 0.07 Å than molecules on top of a B atom. The average height of the O atoms of sublattice A over BN is 3.37 Å. The O–O nearest neighbor distances are 2.6 Å, when an A molecule is the donor in the H-bond, and 2.8 Å when it is the acceptor. In the final configuration, all molecules belonging to the same sublattice are equally oriented, thus the molecular dipoles sum up to a quite large in-plane value, i.e. 23.92 Debye per unit cell. The most relevant parameters characterizing this and the other optimized structures are reported in Tab. 1.

All the optimizations starting from the M2 model result in a quite flat water overlayer, with corrugation smaller than 0.05 Å. In particular, the

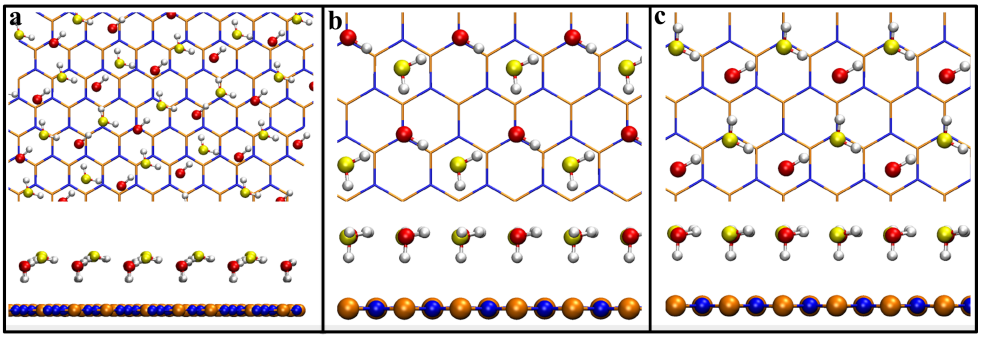

Figure 6.2: Top and side view of different water clusters adsorbed on a flat BN surface. In the ball and stick representation of the structure, the red and yellow spheres are oxygen atoms in different layer, while white for H, blue for N and orange for B, respectively. The BN monolayer is given by the thin lines forming the honey-comb lattice in the top view with the same color scheme. **a**. Model M1. **b**. Model M2_topN. **c**.Model M2_topC.

initial conditions h_0 and h_B give the same optimized structure, which is displayed in panel **b** of Figure 6.2, whereas the structure depicted in panel **c** is obtained when starting from h_A. In both cases, the molecules of one sublattice are parallel to the substrate and donate two hydrogen atoms to form H-bonds with two neighboring molecules. The molecules in the other sublattice employ only one H atom to form one H-bond with a neighboring molecule, while the second H atom is directed towards the substrate. In the first structure obtained from this model and named M2_topN, the molecules of sublattice A point to the N atoms of the BN layer and the corresponding O atoms are 3.27 Å above the substrate. In the second structure named M2_topC, the molecules pointing down are those of the B sublattice, which means that the H atom points to the center of the BN ring. The binding energy between water molecules and substrate is 0.015 eV stronger for the M2_topN than for the M2_topC, because in the former case the interaction is more effective. The M2 lattice is the least dense among those considered in this work, the overall intermolecular distance is quite large, around 2.9 Å. After the optimization, the O–O distances are distributed between values of 2.8 Å, when the molecule parallel to the substrate is the H-bond acceptor, and 3.0 Å, when it is the donor.

In order to rule out biasing effects of the initial orientation of the molecules on the final structure, one optimization run has been started positioning most of the molecules parallel to the substrate. The resulting most stable final structure is also in this case the M2_topN configuration.

The M3 arrangement gives rise only to two different structures when in

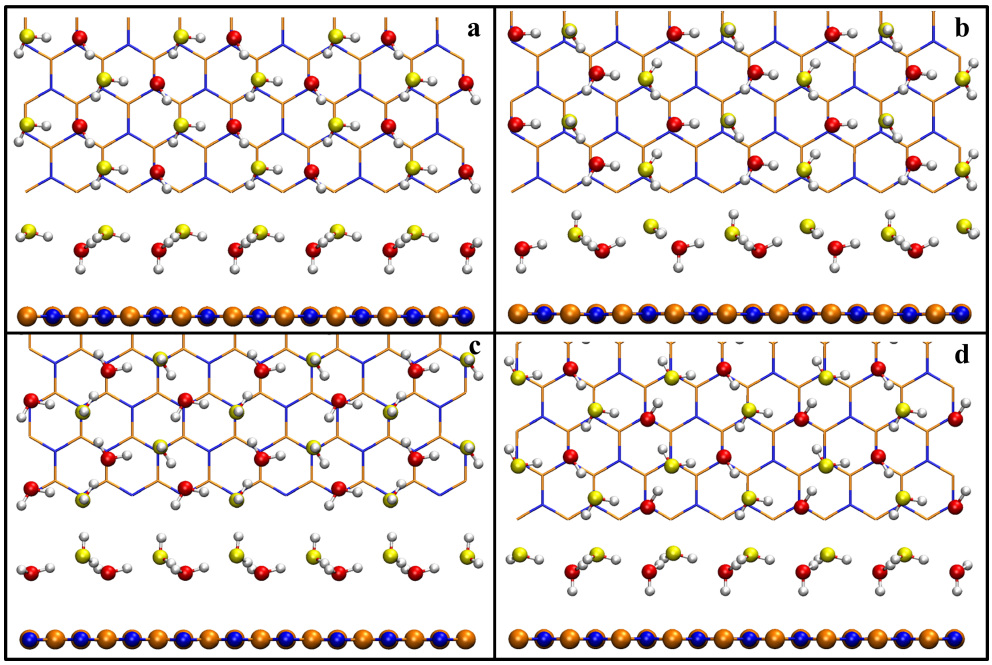

Figure 6.3: Top and side view of different water clusters adsorbed on a flat BN surface. **a**. Model M3_1. **b**. Model M3_2. **c**. Model M3_3. **d**. Model M3_4. See caption of Figure 6.2 for the representation of the molecules.

the initial configuration all the molecules are perpendicular to the surface. However, by selecting different orientations of the molecules that minimize the dipole moment, two more structures could be optimized. In Figure 6.3 the four different structures are reported. In all the analyzed structures, the two sublattices lay at different height over the substrate. The structure displayed in panel **a** of Figure 6.3, and named M3_1, is characterized by having all the molecules belonging to one sublattice equally oriented, as it is also the case for the M1 and M2 structures described above. The *A* molecules are perpendicular to the substrate, forming a H-bond with the closest N atom. The *B* molecules are parallel to BN (yellow in the figure), and both H atoms are employed in inter-molecular H-bonds to neighboring molecules. The sublattice *A* is closer to BN, with an average distance between O and N of 3.31 Å. The height difference between the two sublattices is on average 0.91 Å.

The water molecules in the second optimized structure, M3_2 (panel **b**), can have four different orientations. In sublattice *A*, which is higher over the substrate, half of the molecules are parallel to the substrate and half are perpendicular to it, with one dangling hydrogen pointing upwards. These latter are 0.4 Å lower than the parallel molecules of the same sublattice. The

molecules of sublattice B are closer to the substrate, at an average distance of 3.17 Å and are also distributed among two different kinds. Half of them is parallel to the substrate, but with the molecular dipole differently oriented with respect to the parallel A molecules, whereas the remaining molecules point towards the substrate and form H-bonds to N atoms. The resulting distribution of the molecular dipoles minimizes the total dipole per unit cell, even though the in plane component is still quite large. Moreover, the M3_2 structure turns out to be the lowest in energy among all the water layers adsorbed on free-standing h-BN considered in this work.

A third structure has been obtained from an initial configuration where all the molecules are pointing upwards with one OH, while the other OH bonds are parallel to the BN substrate. The resulting structure, M3_3, is reported in Figure 6.3**c**. It is also a bilayer, where the molecules of sublattice A are still perpendicular to the substrate and pointing upwards, while the B molecules are rotated to a parallel orientation with both hydrogen atoms forming H-bonds with the neighboring molecules. The shortest O-BN distances are about 3.08 Å and the corrugation of the bilayer is about 0.89 Å. Since there is no direct interaction through H-bonds to the substrate, the interaction energy computed for this structure is quite weak, around 0.03 eV lower per molecule.

The fourth structure based on model M3 is the M3_4, which is very similar to M3_1, but with different orientations of the molecular dipoles. The structure is reported in Figure 6.3**d**. Thanks to this redistribution of the molecular orientation a significant reduction of the y component of the dipole moment is obtained with respect to M3_1. Other important parameters like adsorption energy, binding energy and corrugation are very similar to what was already obtained for the M3_1 structure.

We are looking for the molecular arrangement that could best represent the nano-ice cluster observed in the pore of the nanomesh by STM imaging. From the binding energy computed for the described structures, it is not possible to identify an outstanding structure that is significantly more stable than the others. Excluding the M3_2 structure, which is the only one not forming any H-bond with the substrate, the adsorption energy differences are within 0.04 eV per water molecule. The adsorption energy is dominated by the intermolecular hydrogen bonding ($E_{\text{H-bond}}$). Each H-bond contributes more than the interaction with the BN surface (E_{int}). The H-bond energy is in most of the cases around -0.25 eV, with one exception for the M3_2 structure, for which the average hydrogen bonding is more effective with an average energy of -0.27 eV. Stronger H-bonds can be related to the presence of dangling H and a better height distribution of molecules with different orientation. This structure is overall also the lowest in energy and therefore

Table 6.1: Adsorption and Binding Energy for Different Water Model

	Energy (eV)			corrugation (Å)	d_{O-O} (Å)	Dipole moment (D)			
	E_{int}	E_{ads}	$E_{H\text{-}bond}$			μ_x	μ_y	μ_z	$\lvert\mu\rvert$
M1	-0.050	-0.434	-0.256	0.73	2.6, 2.8	155.32	149.05	-52.53	221.58
M2_topN	-0.070	-0.433	-0.242	0.03	2.8, 3.0	68.82	-40.66	-8.63	80.40
M2_topC	-0.055	-0.418	-0.242	0.05	2.8, 3.0	70.24	39.34	-9.82	81.11
M3_1	-0.053	-0.421	-0.245	0.91	2.6, 2.8	72.53	-130.98	-36.84	154.19
M3_2	-0.053	-0.458	-0.270	0.77, 1.15	2.6, 2.7, 2.8	102.81	-63.71	-2.96	120.99
M3_3	-0.023	-0.390	-0.245	0.80	2.6, 2.8	75.74	-2.72	-31.42	82.04
M3_4	-0.053	-0.418	-0.243	0.87	2.6, 2.8	73.45	-0.12	-36.44	82.00
M4	-0.062	-0.429	-0.245	0.90	2.6, 2.8	0.20	-0.49	-18.10	18.11

one of the best candidates for the nano-ice cluster. However, the experimental analysis seems to indicate that the O are distributed over two layers, which would exclude the M3_2, but also all the M2 structures, which show no corrugation at all. Also the other structures that have been described are not very probable due to the large in plane dipole moments (see the data in the table). Therefore a new model was generated which is still based on

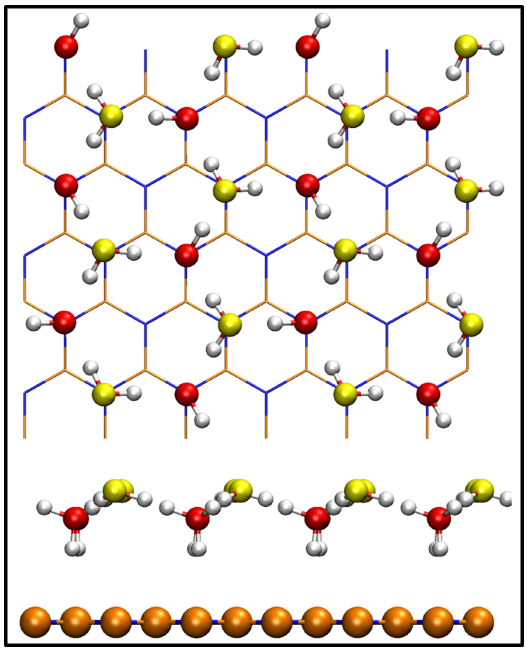

Figure 6.4: Top and side view of model M4 adsorbed on a flat BN surface. See caption of Figure 6.2 for the representation of the molecules.

the M3 distribution of the O atoms over the substrate, which looks to be the most stable since each molecule is approximately on top of one N atom. The unit cell of the new model is a 2×3 supercell containing 24 water molecules with six different orientations of the molecular dipoles, thus minimizing the total dipole moment. The resulting optimized structure M4 is reported in Figure 6.4. The molecules of the two sublattices are distributed over two layers, where the lowest molecules are perpendicular to the surface, with an average O-BN distance of 3.30 Å, each forming one H-bond with the N atom beneath. The other molecules are displaced 0.9 Å higher over the substrate and are parallel to the substrate, with both H atoms forming H-bonds with neighboring molecules. As expected, the x and y dipole components are almost zero, while there is still a contribution along z due to the downwards orientation of half of the molecules. Moreover, the adsorption energy is

one of the lowest among those computed on free-standing BN. Therefore, we consider this low-dipole structure as our best candidate to represent the nano-ice cluster reported from experiment.

6.3.2 Water Cluster on the Nanomesh

The optimization and characterization of the nanomesh superstructure with our computational set up has been already described in previous works[19]. Here we use a slab of four 12 × 12 Rh layers surmounted by a 13 × 13 BN overlayer. By standard structure optimization, the overlayer corrugates and forms the characteristic pore and wire regions, where the pore is a hexagonal-shaped depression of about 2 nm of diameter. 38 molecules have been extracted from the optimized M4 overlayer and have been collocated over the nanomesh, thus covering the whole pore. The initial average height of the O with respect to the topmost Rh layer is about 5.5 Å. The atomic configurations before and after the optimization are reported in Figure 6.5**a** and **b**, respectively. It is observed that the structure optimization induces the reorientation of some water molecules close to the rim of the nanomesh. Indeed, the molecules at the edge of the cluster have dangling H. It is then energetically favorable to redirect the corresponding OH towards the substrate and form additional H-bonds. On the other hand, the rearrangement

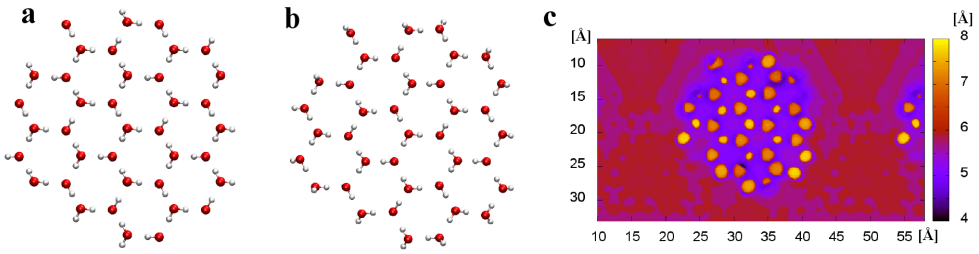

Figure 6.5: Top view of the 38 water molecules optimized in the pore of the nanomesh (**a**. before geometry optimization; **b**. after geometry optimization) and the corresponding STM topography images (**c**) for the optimized structure. The ball and stick representations are used for the water molecule, with the oxygen in red and hydrogen in white, respectively.

induces a neat increase of the total dipole of the cluster, which in the final configuration is 7.95, 17.16, and 12.42 D in x, y and z directions, respectively. The total interaction energy and the adsorption energy are -0.112 and -0.482 eV. The molecules at the border of the cluster typically are single acceptor and single donor in terms of the interaction with the neighboring

molecules. The second OH not involved in water-water hydrogen bonding is free to rotate. When the condition are such that the formation of a H-bond with a N of the substrate is possible, the molecule gets closer to the substrate and the typical N–H distance is around 2.5 Å, corresponding to a quite weak interaction. Being these interactions with the substrate quite weak, several molecules remain with a dangling hydrogen. The potential energy surface along the rotation angle of these molecules is quite flat, therefore the optimization algorithm may have some difficulties in finding a global minimum. The two dimensional cluster is anyway stabilized by the interaction with the substrate. The same cluster in gas phase is, indeed, not stable and tends to a three dimensional aggregate, where each molecule has the possibility to be three or four coordinated with other molecules.

The actual number of water molecules in the pore might also affect the final structure. From the experimental data we know that there should be (20±5) per layer[21], therefore 38 molecules is in the right range. It is even possible that molecules move fast from the cluster to the wire and in the opposite direction, thus changing the conditions at the rim. The presence of molecules on the wire is quite probable, and they could play a role in stabilizing the cluster in the pore. However, these molecule could never be imaged by STM, which is perfectly consistent with fast motion of molecules, weakly interacting with the substrate.

As already observed for the water arrays on free-standing BN, the O–O distances are not all the same. In the center of the cluster, the O–O distance is 2.62 Å if the H-bond acceptor is a molecule parallel to the substrate, whereas it is longer, 2.83 Å, if the acceptor is a molecule interacting with the substrate through its second H, and therefore shifted downwards. Namely, the O atoms of the perpendicular molecule is at about 5.5 Å from the topmost Rh layer, while the other molecules are about 0.8 Å higher. For the molecules at the rim the differences in the O–O distance are smaller, 2.68 Å and 2.79 Å, respectively. The optimized structure reproduces the corrugation of the bilayer nano-ice cluster observed in the experiment. The height difference between the water molecules of the two sublattices is appearing in the STM images as difference in brightness, which is consistent with the interpretation from the experimental analysis. The contrast modulation is more evident in the center of the cluster, whereas, at border where some molecules are rotated, the image becomes more blurred. When the orientation of the molecule is such that the O lone pair is not completely accessible from above, the STM imaging cannot clearly detect the molecular density, and the corresponding area becomes darker. Therefore, at the rim, some of the molecules appear as darker smaller spots or become even invisible.

6.4 Conclusion

In this work, we investigated different models of water molecule assembly adsorbed on BN, which could reproduce the atomic structure of the experimentally observed nano-ice cluster. The proposed initial configurations present similar characteristics in terms of number of molecules per unit, type and number of intermolecular interactions, distance from the substrate, and 2D hexagonal arrangement. The geometry optimizations carried out on flat BN surface lead to structures that are all consistent with a bilayer water lattice as observed in experiment. The intermolecular distances and the adsorption energy do not provide strong arguments to prefer one structure over the others, making one exception for the model M2, which has to be discarded due to the too large intermolecular distance. The distribution of molecular dipole, however, changes significantly from cluster to cluster. We then conclude that the M4 cluster should be the most probable arrangement of water molecules on BN, since by orienting the six molecules forming the hexagonal units in six different ways, the total dipole is minimized. In ref. [21], we already showed that 42 water molecules extracted from the M4 model, without any relaxation, generate a local modulation of the electrostatic potential which closely resembles the experimental observation. Here, 38 M4 water molecules are optimized in the pore of the nanomesh, and the simulated STM image are in agreement with the experiment, where spots of different brightness identify molecules at different height.

Chapter 7

Phthalocyanine on the Nanomesh

H_2Pc and CuPc are large conjugated molecules with 2-fold or 4-fold symmetry respectively. As they are planar molecules in gas phase, they could be used as neutral and apolar molecules in the study of adsorption behavior of molecules on *h*-BN nanomesh. In experiment, after deposition onto the bare nanomesh, it is found that they have very similar adsorption behaviors, but H_2Pc has higher mobility on surface. The molecules prefer the off-center adsorption site along the [21] direction of the nanomesh as already shown in Figure 2.4. In this chapter, electronic structures and properties of the two molecules at different adsorption sites have been investigated. The potential energy surface on which the molecules can move above the nanomesh appears to be quite corrugated, presenting several minima corresponding to slight structural variations. For a better understanding of the dominant contributions to the interaction energy, a simplified model is also proposed, which has been obtained from the mapping of the bare nanomesh electrostatic potential at different heights above the surface as corrected by the vdW interaction between molecule and nanomesh.

In the following, some more details on the computational methods are given. Next the molecules are considered first in gas phase, then on free-standing BN and finally on the nanomesh. At the end of the chapter, the results of interaction energies are mapped with the simplified model, and the nature of the interaction between molecule and nanomesh is discussed.

7.1 Method

All the calculations are performed with the CP2K package[75] with the hybrid Gaussian and plane wave scheme[76]. The model for nanomesh is constituted of a 13 × 13 BN layer and a four-layer 12 × 12 Rh slab, which is corresponding to the full unit cell of the nanomesh. An extra H_2Pc or CuPc molecule is adsorbed to the nanomesh, thus there would be almost 1000 atoms in the investigated system. To reduce the computational cost, GTH pseudopotentials[77, 78, 79] are employed to represent the atomic cores, and especially for the Rh atoms, only 9 valence electrons rather than 17 electrons are considered. Moreover, a [2s1p2d] molopt basis set[80] instead of double zeta basis set is used to match with the large core q9 pseudopotential of Rh. The influence of different pseudopotentials together with the matching basis sets for Rh atoms has been studied in the following for the bare nanomesh system. Double zeta short range basis sets are used for other atomic kinds. revPBE functional is used for the exchange and correlation functional[43, 44]. In order to estimate the effect of the vdW correction calculated according to the formalism of Grimme, for both bare nanomesh and one specific adsorption site, the geometries have been optimized with both Grimme D2[48] and Grimme D3[49], and the results have been compared. For all other calculations, unless otherwise specified, the Grimme D3 scheme has been adopted. STM and work function images are also generated for the optimized structures at different adsorption sites based on the Tersoff-Hamann approximation[53, 54] at the isocurrent surface, and details could be found in chapter 5. To evaluate the adsorption strength, the binding energy is calculated for each adsorption site, by using the total energy of the system, minus the sum of the energies of nanomesh and adsorbate optimized in free-standing state, i.e. $\Delta E_b = E_{total} - E_{NM} - E_{ad}$. BSSE corrections using Boys and Bernardi counterpoise method[88] are considered for all the energies reported here, except mentioned otherwise.

The interaction between nanomesh and H_2Pc has been characterized using a simplified model, where the optimized structure of the bare nanomesh and of the isolated molecule in gas phase are considered. The interaction is then given by two terms, one electrostatic contribution and one dispersion (vdW) contribution. For the electrostatic contribution, the electrostatic potential generated by the nanomesh is computed on a given grid filling the whole simulation cell, V_{ES}^{NM}. On the same grid, also the total density of the isolated molecule, n, is computed. By changing the position of the molecule's center R_0^{mol} in the simulation cell, and providing that the molecule lays always at the same height, different values of the electrostatic contribution to the

interaction energy are obtained as

$$E_{ES}(i) = dV_{grid} \sum_{k=1}^{N_{grid}} V_{ES}^{NM}(k) n(R_{0,i}^{mol}, k). \tag{7.1}$$

where dV_{grid} is the volume element of the grid, N_{grid} is the number of grid points, $V_{ES}^{NM}(k)$ is the value of the electrostatic potential due to the bare nanomesh at the grid point k and $n(R_{0,i}^{mol}, k)$ is the value of the total density of the molecule at point k, when the molecule is centered in $R_{0,i}^{mol}$. By changing $R_{0,i}^{mol}$, the interaction is mapped for many different positions of the molecule. The electrostatic interaction is then corrected by the vdW contribution, computed with the Grimme D3 potential for the specific position $R_{0,i}^{mol}$ of the molecule on the nanomesh.

7.2 H_2Pc and CuPc in gas phase

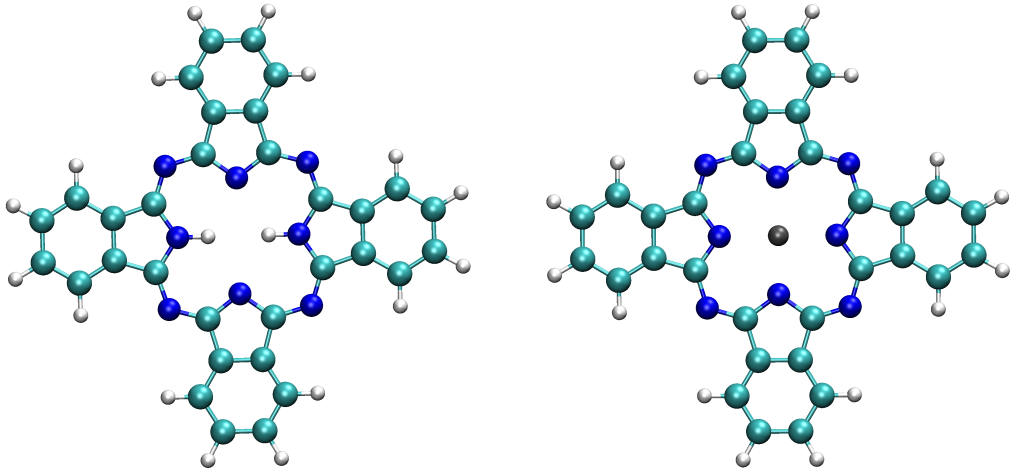

Figure 7.1: Ball and stick representation of H_2Pc and CuPc optimized in gas phase. The color of N, C ,H and Cu atoms are in blue, cyan, white and gray respectively.

The H_2Pc and CuPc molecules are first optimized in gas phase with Grimme's D2 correction[48]. Because all the C and N atoms are of sp^2 hybridization, the molecules tend to be flat after relaxation (Figure 7.1). In H_2Pc, the N-H distance is 1.02 Å, while in CuPc, the N atoms in the isoindole group is coordinated with the Cu atom, with a Cu-N distance of 1.97 Å. The

neighboring distance between the N atom in the isoindole group is 2.82 Å and 2.80 Å for H_2Pc and CuPc respectively, while the distance between the N atoms connecting the isoindole groups is around 4.8 Å for both structures. The C-H distances are all equal to 1.09 Å. Different C-C bond length are also reported. For the C atoms belonging to the phenyl group, they are about 1.40 Å, and for C-C bonds outside the phenyl group, they are around 1.46 Å. Although different atoms (H or Cu) are bound in the center of the Pc molecule, the difference in the structure is not very significant. The most important difference could be that CuPc has an unpaired electron, which makes the calculations extremely difficult when adsorbed on nanomesh. For single CuPc molecule, the spin density is mostly localized on the Cu and on the four closest N atoms of the isoindole group. From the Mulliken population analysis, a spin moment of $0.54e$ turns out to be located on the Cu atom, while $0.11e$ is found on each of the four N atoms. From the Mulliken charge analysis, it turns out that the largest difference between the two molecules is located outside the phenyl groups. The Mulliken charge assigned to Cu atom is $0.10e$, and the charges on the closest N are all -$0.10e$ in CuPc, while in H_2Pc, the N atoms bonded with H atoms are more positively charged, $0.13e$, and the other two N atoms are more negatively charged, -$0.26e$. For the connecting N atoms, the difference is much smaller, -$0.13e$ in CuPc and -$0.17e$ in H_2Pc.

7.3 NM q9 setup versus NM q17 setup

Previously, the nanomesh model was generated with Rh atoms calculated in double zeta short range basis set together with the q17 pseudopotential (NM q17 setup), i.e. 17 valence electrons are considered explicitely. But here, the investigated system contains almost 1000 atoms, so in order to reduce the computational cost and sample more adsorption sites, [2s1p2d] basis set together with the q9 pseudopotential (NM q9 setup) are employed for the Rh atoms, which means that only 9 valence electrons are treated explicitely for each Rh atom. In order to validate this new setup, the geometry optimization of the nanomesh has been carried out for both q9 and q17 setup with Grimme's D2 dispersion correction[48] and some properties are reported in Table 7.1. The simulated STM and work function images generated for both optimized structures are reported in Figure 7.2. All images are generated at the bias potential of -0.5 eV and the electron density of 1×10^{-6} e/a_0^3. The STM images for both structures are very similar, and they both give the characteristic hexagonal shape of the nanomesh pore. The only difference is that, at the isocurrent surface, the absolute height for q17 setup is a little

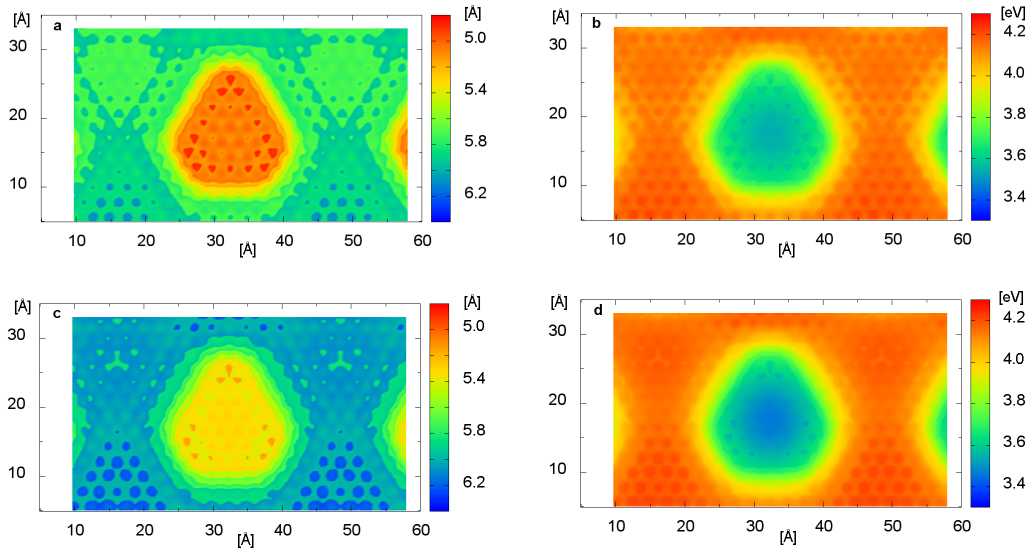

Figure 7.2: The simulated STM topography (**a** and **c**) and work function (**b** and **d**) images for nanomesh optimized with q17 (**a** and **b**) and q9 setup (**c** and **d**) respectively.

bit lower, where the height value is corresponding the the topmost Rh layer. For example, the height of the pore for q17 setup is around 5.0 Å, and the height of the wire is around 5.8 Å, which gives a corrugation of 0.8 Å, while in the STM image generated from q9 setup, the pore is at the height of 5.4 Å, 0.4 Å higher than the one in q17, and the height of the wire is also 0.4 Å higher, at about 6.2 Å above the Rh slab. The corrugation of about 0.8 Å is the same. The difference in the work function images are much smaller, and the two images are practically identical. As we use four layers of 12 × 12 Rh atoms for the metal slab, which corresponds to 576 atoms, hence when we consider only 9 valence electrons instead of 17, together with a smaller basis set, it largely reduces the computational cost. For NM q9 setup, one self-consistent field (SCF) iteration takes about 45 s on 128 processors of Sun Blade X6275 cluster, while for NM q17, 100 s is required. If we look closer to the structural changes, the differences in the height of the first and second Rh layers are less than 0.1 Å, on average 0.07 Å and 0.03 Å, respectively, while the last two Rh layers are kept fixed in their bulk structure during the geometry optimization. The change in the distances between the layers are even smaller, less than 0.05 Å. The definition of the pore and wire is quite arbitrary. Here, we define the B or N atoms with a distance to the Rh slab less than 2.6 Å as the pore, and larger than 2.9 Å as the wire. The atoms in-between are considered belonging to the rim. The percentage of

the pore is almost unchanged, with 31.9% for q9 setup compared to 32.2% for q17, while the wire region in q9 increases a little bit, by about 3.6%, but only very few atoms are involved. The MLWFs are also located for both optimized structures, and Figure 7.3 shows the z value of the N atoms and the corresponding distance of the lone pairs to their nuclei. The polarization of the N lone pairs in the presence of the metal slab is a quite important feature, and it's considered as the evidence of covalent bond formation in the pore region. With q9 setup, the polarization of the N lone pairs could be reproduced as q17, and in the pore the distances of MLWF centers to their nuclei are drastically increased due to the formation of the covalent bond between N and the Rh atom right beneath.

7.4 Grimme's D2 versus D3 dispersion correction

Both Grimme's D2 and D3 vdW correction have been employed for the geometry optimizations of the bare nanomesh, and also one specific adsorption site of H_2Pc on nanomesh starting from the same initial structure. Here, the calculations are only carried out with the q9 setup for Rh atoms. The average height of Rh layers, the distance between Rh layers, the percentage of the pore and the wire region, as well as the vdW contributions are shown in Table 7.2. The effects of different vdW corrections on the structure of the Rh slab are almost invisible, as we could see from Table 7.2, the average Rh layer height, the distance between layers are identical for the nanomesh

Table 7.1: Comparison for nanomesh optimized in q9 setup and q17 setup

	NM q9	NM q17
SCF iteration (s)	∼45	∼100
electrons	6536	11144
basis functions	13034	19370
$z_{Rh}^{1^{st}layer}$ (Å)	-0.01	0.06
$z_{Rh}^{2^{nd}layer}$ (Å)	2.22	2.25
d_z ($Rh^{1^{st}}$-$Rh^{2^{nd}}$) (Å)	2.23	2.18
d_z ($Rh^{2^{nd}}$-$Rh^{3^{rd}}$) (Å)	2.19	2.15
pore%	31.9%	32.2%
wire%	59.8%	56.2%

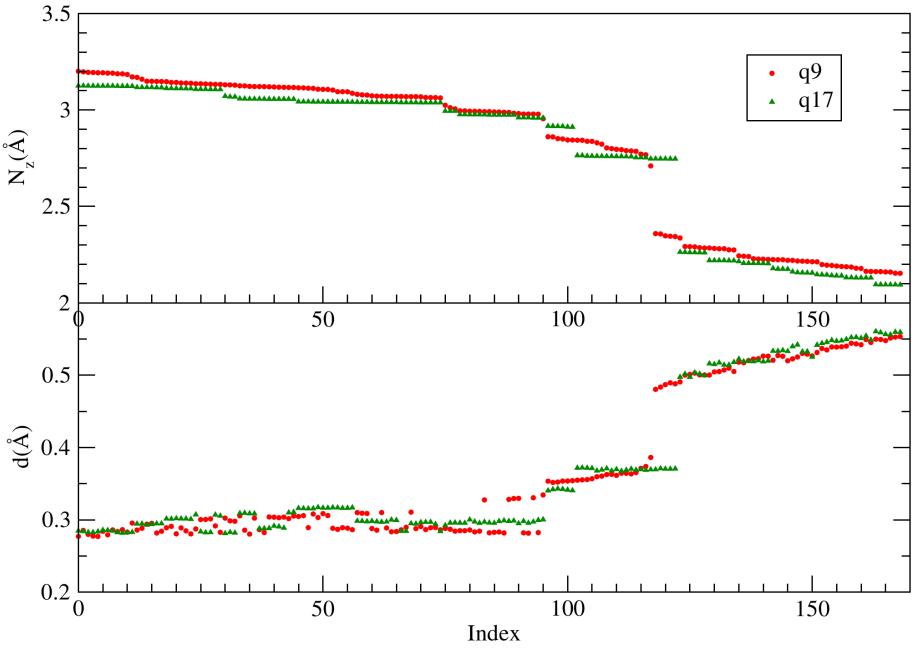

Figure 7.3: Distance of the N atoms from the topmost Rh layer projected along the z axis (**Upper Panel**) and projected distance of MLWF centers of N lone pairs from the corresponding atomic centers (**Lower Panel**). The red solid circles are obtained for the nanomesh optimized with the q9 setup, while the green solid triangles are for the structure optimized with q17.

with or without adsorbate. However, from the percentage of the pore and wire regions, with the D3 correction, the pore region becomes smaller, by less than 2% in the bare nanomesh, which is mainly due to the B atoms. If we define the percentage of the pore based purely on the height of the N atoms, then it's 30.2% for both D2 and D3 corrections. The interaction between the wire and the metal slab mainly comes from the vdW interactions, therefore, the influence of different dispersion corrections is more significant in the wire region, with the wire region increased by almost 6% in D3 correction compared to D2. As it is generally considered that in D2 correction, the vdW interaction is largely overestimated[49], thus with D3 dispersion correction, the interaction between the wire and the Rh layers is weaker, hence, the BN layer is slightly farther away from the Rh slab beneath, resulting more atoms belonging to the wire. This overestimation of the D2 dispersion correction could also be observed from the E_{vdw} in Table 7.2, which is the vdW dispersion correction energies. In both case, the D2 dispersion energies are around 5.6% larger than the D3 dispersion correction. Because of this overestimation

in D2 correction, in the following investigations involving different adsorption sites, we have only employed Grimme's D3 dispersion correction.

Table 7.2: Comparison for nanomesh and H_2Pc/nanomesh optimized in Grimme's D2 and D3 dispersion corrections

	h-BN/Rh		H_2Pc/*h*-BN/Rh	
	D2	D3	D2	D3
$z_{Rh}^{1^{st}layer}$ (Å)	-0.01	-0.01	-0.01	-0.01
$z_{Rh}^{2^{nd}layer}$ (Å)	2.22	2.22	2.22	2.22
d_z ($Rh^{1^{st}}$-$Rh^{2^{nd}}$) (Å)	2.23	2.23	2.23	2.23
d_z ($Rh^{2^{nd}}$-$Rh^{3^{rd}}$) (Å)	2.18	2.18	2.18	2.18
pore%	31.9%	30.2%	34.3%	31.1%
wire%	59.8%	65.4%	56.5%	63.9%
E_{vdw} (eV)	-493.74	-467.78	-502.89	-475.92

When an H_2Pc molecule is adsorbed on the bare nanomesh, the change of the nanomesh pore and wire region is not only affected by different dispersion corrections, but also the adsorbed molecule. As the molecule is adsorbed on the off-center site, and due to the large size of the molecule, except the phenyl ring centered on the nanomesh center, the other three are partially above the wire region, thus the distance between the molecule and the substrate underneath is closer. Therefore, the interaction is more repulsive, and this repulsive force pushes the wire region underneath towards the metal slab. As a result, extra bounding between the N and Rh atoms are formed, which is evident from the total charge density difference of the whole system compared to free-standing *h*-BN and Rh slab as displayed in Figure 7.4, where the hexagon formed by red lines indicates the original pore shape before structure optimization. In both structures optimized with D2 and D3 correction, extra densities, indicated by red and blue clouds (red indicates the accumulation of the charge density, while blue indicates the depletion of the charge density), could be observed outside the red hexagon. With D3 correction, the pore is more likely shifted, as the bounding between five N atoms to the Rh underneath inside the hexagon disappears, which could be a compensation of the extra bounding formed outside the hexagon. Due to this change of pore shape, the pore size in the STM images looks smaller compared to the STM image generated from D2 correction (Figure 7.5).

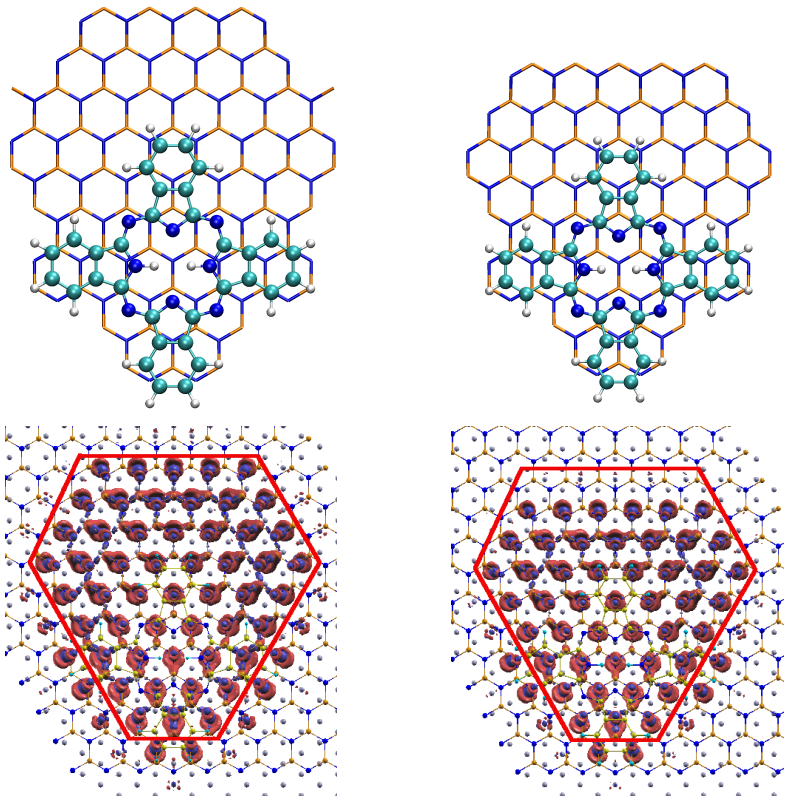

Figure 7.4: The structure and the total charge density difference for structures optimized with Grimme's D2 (left column) and D3 (right column) dispersion correction. The B and N atoms in the pore are represented with sticks, while the H_2Pc molecule is in ball and stick representation. And the color scheme is: B: orange; N: blue; C: cyan; H: white. In the total charge density difference, the colors of red and blue are used for the accumulation and depletion of the charge densities. And the original shape of the pore is indicated by the red hexagon.

7.5 H_2Pc on a Free-standing BN Surface

The adsorption behavior of H_2Pc is first studied on a flat free-standing 13 $\times$ 13 *h*-BN surface. Three different BN lattices are employed corresponding to the BN bond length in the pore of the nanomesh (2.520 Å), experimental BN lattice (2.504 Å) and the nanomesh unit cell (2.481 Å). The optimized structures are shown in Figure 7.6, while the energy and corrugation properties are reported in Table 7.3. In the initial structure, the H_2Pc molecule is placed along the [21] direction of the unit cell, i.e. perpendicular to the zigzag N lattice. In all three cases, when the H_2Pc is approaching the BN

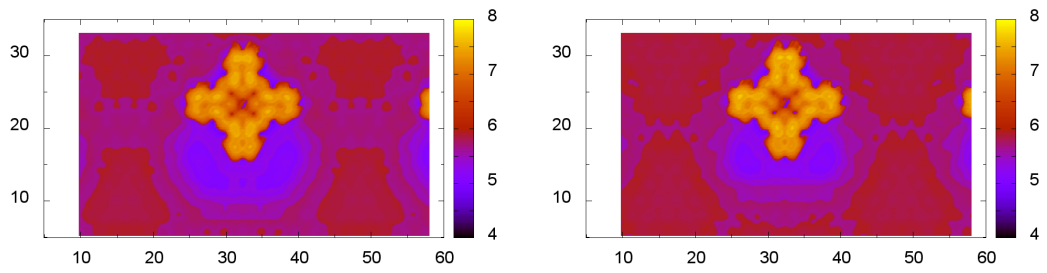

Figure 7.5: Simulated STM topographies for H_2Pc adsorbed on the nanomesh optimized in Grimme's D2 (**Left**) and D3 (**right**) dispersion correction respectively. The isocurrent surfaces are generated at the bias potential of -0.2 eV and with the density of 1.0×10^{-6} e/a_0^3. All the scales are in Å.

surface during the geometry optimization, BN atoms at the adsorption site tend to move upwards due to the attraction between the H_2Pc molecule and the surface, however, when the adsorbate continuing approaching the surface, the tendency of moving back in order to sustain the flat surface could be observed at the lattice constance of 2.520 Å and 2.504 Å as further stretching of the BN bonds is not favored. Thus in the final structure, the deviation of the BN atoms in z direction is only 0.14 Å at lattice constance of 2.520 Å, while at the experimental lattice constant of 2.504 Å, the deviation is a little bit larger, around 0.33 Å. When the BN surface are constrained with the lattice constant of 2.481 Å, only the moving up of the BN atoms underneath the adsorbate could be observed, while the BN atoms elsewhere even get concave. The significant corrugation is induced by the interaction between the molecule and the surface, as BN surface alone could stay flat at the same lattice constant, and this corrugation could also compensate to the lattice constrain. The deviation for the optimized structure compared to the average height in this case reaches 0.68 Å in z direction. This is also the only case, where the DFT contribution to the binding energy is negative, i.e. attraction between H_2Pc and BN substrate. Although the Grimme's vdW correction in this structure is the weakest, it still has the strongest binding energy. This could be explained by the fact that the distance between H_2Pc and the substrate is around 3 Å in all cases, but with larger corrugation of the BN, the distance between H_2Pc and BN atoms in other region despite the topmost ones increases. Therefore, the vdW dispersion correction is the weakest among all lattice constants, which is compensated by the attractive DFT energy.

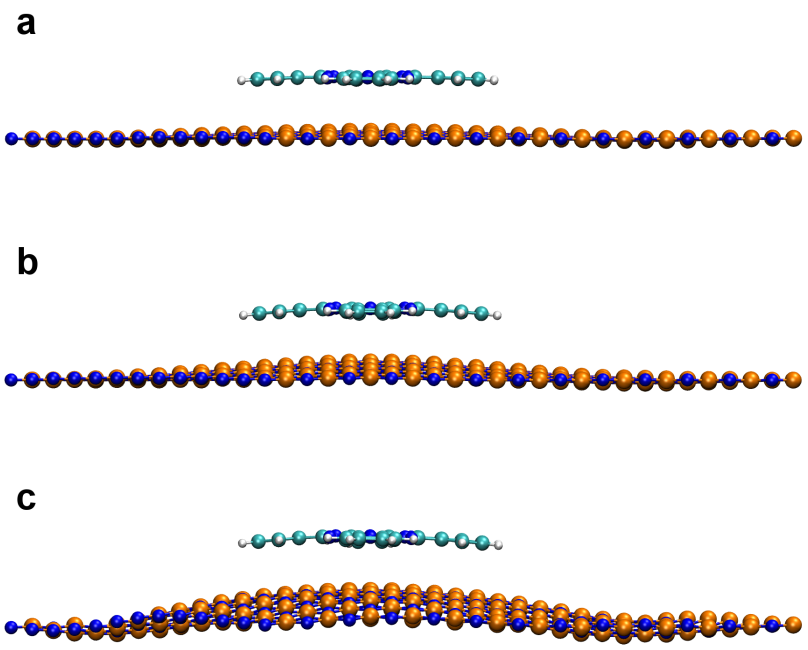

Figure 7.6: Side view of optimized H_2Pc on BN with different BN lattices. **a**. a_0=2.520 Å. **b**. a_0=2.504 Å **c**. a_0=2.481 Å

7.6 H_2Pc or CuPc on the nanomesh

As indicated by the black hexagon in Figure 7.7, the nanomesh pore is hexagonal shaped. Three possible [21] directions exist and are named [21]_1, [21]_2, and [21]_3 respectively (see Figure 7.7). Thus, six possible [21] off-center adsorption sites are investigated for the H_2Pc molecule. For each [21] direction, the molecule is located with two opposite isoindole groups along the [21] direction, of which, one of the isoindole group is centered in the very center of the pore, in that case, it would result in two different adsorption sites, denoted by "_h" or "_l" according to the higher or lower position of

Table 7.3: Binding energy of H_2Pc on a free-standing BN Surface

Lattice Constant (Å)	Energy (eV)			δ_z (Å)
	ΔE_b	ΔE_{DFT}	ΔE_{vdW}	
2.481	-4.32	-0.37	-3.95	0.68
2.504	-2.51	1.72	-4.23	0.33
2.520	-2.38	1.84	-4.22	0.14

the molecule along the [21] direction. Besides, the adsorption sites with the molecules on the very center of the pore (along [21]_1 direction), and on the wire are also investigated. For CuPc, as we have already mentioned before, the calculations are extremely expensive and it converges very slowly due to the unpaired electron, so only two adsorption sites, with the CuPc molecule adsorbed on the center of the nanomesh pore and the [21]_1 off-center position, are considered here. In H_2Pc molecule, two H atoms are bound to

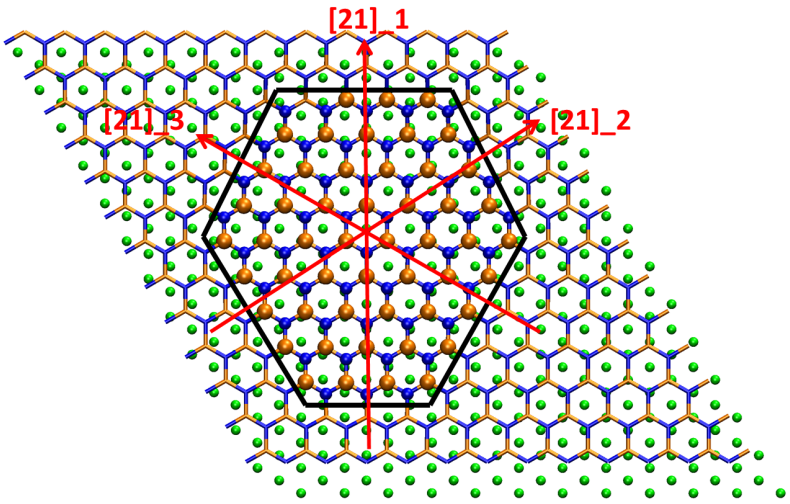

Figure 7.7: Top view of nanomesh. The B and N atoms in the pore are represented by ball and stick, while the rest is represented by line. The color of B and N atoms are orange and blue, respectively. The green sphere in the background is the Rh atom. The shape of the pore is indicated by the black hexagon. Three [21] directions of the nanomesh are suggested by the red arrow, labeled by [21]_1, [21]_2, and [21]_3 respectively.

the N atoms, when adsorbed on the nanomesh, two different configurations are possible due to the position of these two H atoms. One is with the N-H bonds along the [21] direction, the other is with them perpendicular to the [21] direction. The influence of the H position to the adsorption is first evaluated by structure optimization with the H_2Pc molecule adsorbed to the same position of the nanomesh, but with different N-H orientations. It turns out the effect of the N-H position is negligible as the energy difference for the optimized structures is less than 0.4 meV. Thus, all the calculations carried out afterwards are with the N-H bonds perpendicular to the [21] direction.

The energetic profiles for all the investigated adsorption sites are listed in table 7.4. For adsorption sites of [21]_1_l and [21]_1_l_d, the only difference of

Table 7.4: Binding energy and energy components for different adsorption sites of H_2Pc and CuPc (All in eV)

	ΔE_b	ΔE_{DFT}	ΔE_{vdW}	ΔE_{NM}	ΔE_{Pc}	$\Delta E_{NM}+\Delta E_{Pc}$
H_2Pc						
[21]_1_h	-2.71	2.37	-5.08	0.091	0.020	0.111
[21]_1_l	-2.92	2.75	-5.67	0.224	0.021	0.245
[21]_1_l_d	-2.70	2.35	-5.05	0.124	0.044	0.168
[21]_2_h	-2.75	2.80	-5.55	0.257	0.027	0.284
[21]_2_l	-2.94	2.38	-5.32	0.053	0.028	0.081
[21]_3_h	-2.66	2.81	-5.47	0.270	0.036	0.306
[21]_3_l	-2.87	2.41	-5.28	0.108	0.038	0.146
center	-3.03	2.38	-5.41	0.077	0.015	0.092
wire	-2.29	2.55	-4.84	0.051	0.017	0.068
CuPc						
[21]_1_l	-2.53	2.81	-5.34	0.645	0.056	0.701
center	-2.73	2.77	-5.50	0.648	0.019	0.667

the initial structure is the height of the H_2Pc molecule above the nanomesh. Generally, the molecule is placed about 3 Å above the nanomesh, but in the structure of [21]_1_l_d, the molecule is 1 Å farther apart from the substrate. The optimized height of the molecule is always around 3.2 Å above the substrate underneath. In the off-center adsorption sites, the molecule is not completely above the pore of the nanomesh, but partially above the wire, so after optimization, the bending upwards of the initially almost flat H_2Pc or CuPc molecule is observed above the wire region due to the fact that the adsorbed molecule is trying to adapt the corrugation of the nanomesh. This could be significantly observed in the [21] direction of the nanomesh, while for the [10] direction, it's still almost flat, as only the outmost phenyl ring along the [21] direction is largely affected (see Figure 7.8). The height difference in H_2Pc could even reach 1 Å in [21]_1_h adsorption site, which is exactly the structural corrugation in the nanomesh model employed here. While in the center adsorption sites, as the molecule is solely above the pore region, it stays flat. Moreover, in the wire adsorption site, the phenyl ring close to the pore is partially above the rim of the nanomesh, thus, the C, H atoms bending towards the nanomesh could be observed during the structure optimization, which gives a corrugation around 0.3 Å. This corrugation of H_2Pc molecule is also evident from the simulated STM image generated with a bias potential

of -0.2 eV and at the density of 1.0×10^{-6} e/a_0^3 (Figure 7.8). However, it's not so obvious from the experimental STM image. The explanation could be that in experiment, the STM tip is several Å away from the sample, while in the simulation, we take the isocurrent surface very close to the studied system. In that case, we could pick up some extra informations compared to the experiment. The change of the pore shape of the nanomesh could also be observed for different adsorption sites, which is reflected in the corresponding STM images. However, because only one or two rows of atoms are involved, it is within the experimental error bar and thus not evident experimentally. Indeed, the simulated STM image matches with the experimental one when adsorbed in the off-center position. Unfortunately from the energetic profile, the center adsorption site is the most stable one for both H_2Pc and CuPc adsorption as we could see from Table 7.4. However, the adsorption sites [21]_1_l and [21]_2_l are only 0.1 eV higher in binding energy, which could be considered the same as the center site due to the limitation of the method accuracy.

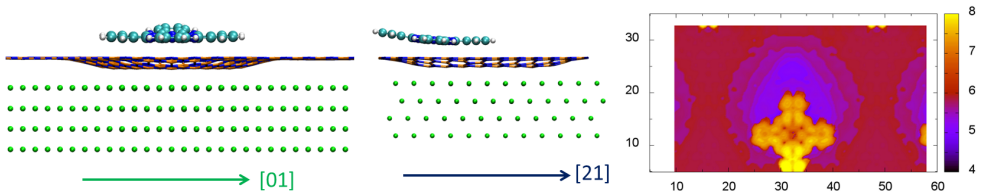

Figure 7.8: Side view of H_2Pc molecule adsorbed on [21]_1_h site along [01] and [21] direction of the nanomesh.*h*-BN layer is represented in thin lines with B in orange and N in blue, while ball and stick representations are used for H_2Pc and Rh slab with C in cyan, N in blue, Rh in green and H in white. The corresponding STM image is also generated at the bias potential of -0.2 eV and with the density of 1.0×10^{-6} e/a_0^3. All the scales are in Å.

If we look at the components of the adsorption energy, the binding is purely contributed by the vdW correction, and the DFT contribution is repulsive, which could be due to the fact that the distance between the adsorbate and the substrate is closer compared to the pure DFT optimization. Since the binding energy totally relies on the vdW correction, the accuracy of which is of high importance. However, it's very possible that the vdW correction is overestimated when all the pair contributions are included, especially for large systems such as the case studied here. The vdW contribution of the *h*-BN layer to the binding energy is around 88%, while the rest 12% comes from the metal slab. The energy cost for the nanomesh and adsorbed

molecule compared to the structure optimized in free-standing is relatively small, especially for the adsorbate. But if we look at [21]_1_l and center adsorption sites, almost 0.23 eV is paid to constrain the nanomesh in [21]_1_l position, while in center site it only costs 0.077 eV, and this difference is also reflected in the DFT and total binding energies. Although from the vdW correction, the [21]_1_l site is 0.25 eV more favored, it turns out the center site has a lower binding energy because of the less repulsion in DFT contribution.

Table 7.5: Binding energy and energy components for different adsorption sites of H_2Pc along [21]_1 direction (All in eV)

	ΔE_b	ΔE_{DFT}	ΔE_{vdW}	ΔE_{NM}	ΔE_{Pc}	ΔE_{NM}+ΔE_{Pc}
1([21]_1_h)	-2.71	2.37	-5.08	0.091	0.020	0.111
2	-2.92	2.57	-5.49	0.202	0.011	0.213
3(center)	-3.03	2.38	-5.41	0.077	0.015	0.092
4	-2.85	2.26	-5.11	0.090	0.023	0.113
5([21]_1_l)	-2.92	2.75	-5.67	0.224	0.021	0.245

Different adsorption sites are also chosen along one specific [21] direction, the [21]_1 direction of the nanomesh and all the data are listed on Table 7.5. Here five different adsorption sites are considered and position 1, 3 and 5 correspond to [21]_1_h, center and [21]_1_l adsorption sites, while position 2 and 4 is taking the middle point of position 1, 3 and 3, 5 respectively. All the binding energies are very close to each other except for position 1. Both position 2 and 5 are only 0.1 eV higher in energy than position 3. And for position 2 and 5, more energy is paid to constrain the nanomesh from the optimized structure, like what we already discussed before. The binding of H_2Pc molecule to the nanomesh is pretty weak, and the energetic profile here indicates that the potential energy surface could be quite shallow, so that during the geometry optimization, the molecules could always stay at the initial position, without any rotation or significant translation in xy plane. The largest displacement here is for position 2, which moves towards position 1 for about 0.4 Å.

Tests on benzene monomer adsorbed on a flat free-standing 13 × 13 BN surface at three different lattice constant (a_0=2.481, 2.504 and 2.52 Å respectively) are performed, which reveal that the most stable adsorption site would be that the benzene monomer is parallel to the BN surface, with the same orientation of the BN hexagon, and centered on a N atom (in this case, half of the C atoms will be on top of B atoms in the substrate). It

is more than 0.05 eV lower in energy compared to the site that benzene is centered on a B atom instead. Even with the same adsorption site, the adsorption energy is slightly stronger at a smaller BN lattice constant. When the lattice constant is 2.481 Å, which is corresponding to the BN in the wire region, the binding of benzene centered above a N atom is -0.65 eV. It is -0.56 eV when the lattice constant is 2.52 Å, which corresponds to the BN in the pore region. This could explain why the H_2Pc or CuPc molecules prefer the off-center position, partially above the wire, as the C-C bond length fits better with the BN lattice on the wire, resulting stronger binding. When the benzene molecule is rotated 90°, the same as the orientation of phenyl group in H_2Pc along the [21] direction, the most favored site is still when the molecule is centered above a N atom, but the adsorption energy is about 0.015 eV weaker compared to the configuration without any rotation. The distance between the centers of the phenyl group in H_2Pc along the molecular axis is around 10.8 Å, while the most suitable NN distance along the [01] direction of the nanomesh (the zigzag N lattice) is about 10.1 Å, so both the phenyl groups along the [01] direction could be centered above N atoms, but slightly shifted, and this orientation of the phenyl group is more preferred. However, along the [21] direction, the NN distance is either too short (around 8.7 Å) or two long (about 13.0 Å), in this case, only one phenyl group could be centered on a N atom. Meanwhile, only the phenyl group in one molecular axis could be centered above N atoms at once. Further geometry optimization with both phenyl groups along [01] direction almost centered above N atoms give a pretty strong binding configuration, about -2.94 eV, and for the same adsorption site, starting from only one phenyl group along the [01] direction right centered above one N, the molecule slightly shifts along the [01] direction, tends to have both phenyl groups centered above N atoms, in which, the binding energy is -2.95 eV. So both structures give very close binding energies compared to the center adsorption site, 3.03 eV. If only the phenyl group on the wire is centered above N atom, the optimized structure is a little bit less stable, with a binding energy of 2.81 eV. Furthermore, when the phenyl group above the center of the nanomesh is centered on a N atom, during the geometry optimization, it tends to move towards the center of the nanomesh, so that the benzene rings along the [01] direction could achieve their most favorable position, with N atoms underneath the center of BN ring. Other tested structures with benzene ring centered on B atoms, or N atoms in the H_2Pc molecule right above B atoms in the initial structure don't give any strong binding configurations. Thus, the most significant contribution should come from the attraction between C and B atoms.

7.7 Simplified Model

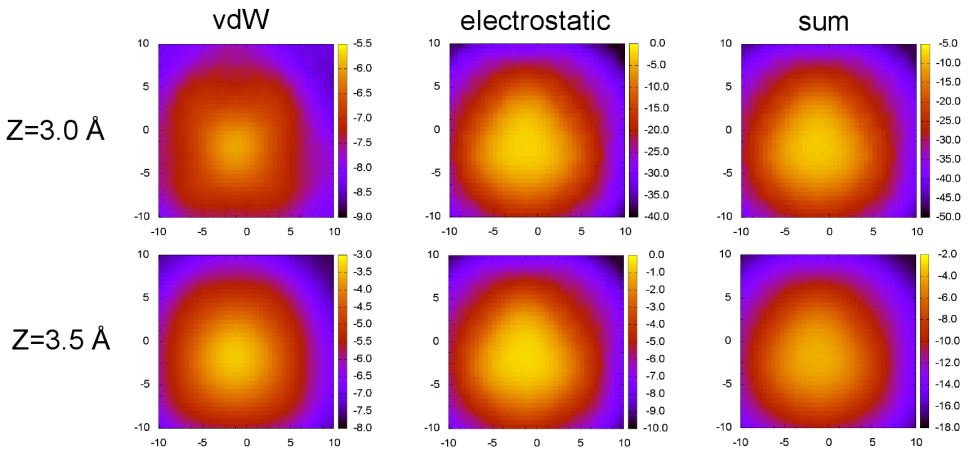

Figure 7.9: Color contour of the vdW interaction, electrostatic interaction, and the sum of them for H_2Pc molecule adsorbed on different position of the nanomesh on the xy plane at z=3.0 and 3.5 Å, respectively. The unit for x, y axes are in Å, while the color scale is in eV.

A simplified model based on only electrostatic and vdW dispersion correction are also applied for H_2Pc adsorbed on the nanomesh in order to interpret the experimental findings. The optimized structure of nanomesh in free-standing is used and the center of 3N atoms are set to (0,0,0). After that, the free-standing H_2Pc optimized in gas phase is added parallel to the nanomesh, with the center of the molecule moving in x and y directions at the grid of 0.1 Å at a chosen height. The electrostatic, vdW interaction map together with the sum of these two are displace in Figure 7.9 at height of 3 Å and 3.5 Å respectively for H_2Pc molecule. For both electrostatic and vdW interactions, the binding is the weakest in the center of the nanomesh, and the strongest while on the wire, which could be due to the fact that the molecule is set at the same height. Because of the corrugation of the nanomesh, when the molecule is on the wire, it's closer to the nanomesh, and as both the electrostatic and vdW interactions highly depend on the distance, it gives stronger binding on the wire. However, if we compare the images at height of 3 Å and 3.5 Å, we could see that these interactions decrease fast when the distance is increasing, especially for electrostatic potentials. Hence, the sum value on the wire of height 3.5 Å is larger than the sum on the pore of heigh 3 Å, indicating a weaker binding. In reality, the molecule always like to be around 3 Å above the substrate, so the height of the molecule on the wire

would be even around 4 Å, which could give a weaker interaction compared to height of 3.5 Å. Thus, the strongest binding would be appear when the molecule is adsorbed on the rim of the nanomesh, which is consistent with the experiment. But this cannot give any exact direction of adsorption, and the bending of the molecule in order to adapt the height difference on the substrate is also not considered.

7.8 Conclusion

In this chapter, we have investigated the adsorption behavior of H_2Pc and CuPc on the *h*-BN nanomesh, and mainly focus on the H_2Pc molecule due to the expensive computational cost of unpaired electron in CuPc. The findings based on DFT calculations are not quite consistent with the experiment, as the adsorption energies are pretty weak for the system and it seems that the molecule could stay in all the positions investigated. But the binding energies for certain experimentally indicated adsorption sites are within the DFT accuracy limit if compared to the most favored adsorption site, i.e. above the very center of the nanomesh. As indicated from the adsorption of benzene monomer on a free-standing BN surface, the lattice difference between the wire and the pore of the nanomesh might be the reason of the off-center adsorption site. But this is less evident in the nanomesh system we investigated, it could be because that the adsorbate is relatively small compared to the substrate size and the interaction are mainly described by vdW corrections. Thus more accurate dispersion correction is needed for this kind of metallic weak interaction system, especially when contains thousands of atoms. Although it's already shown that Grimme's D3 correction works well for weak interaction systems in small molecular size, still little is known about the accuracy on large scale metallic system and unfortunately, higher level quantum mechanical calculations such as MP2 could not be employed to validate the efficiency. A simplified model considering only the vdW and electrostatic interaction indicates that the molecule would prefer to adsorb on the rim of the nanomesh. However, in this model, the molecule is kept flat all the time, while quantum calculations suggest that the molecule will adapt to the corrugation of the nanomesh when gradient exits on the substrate. Further step of molecular dynamics might help to better explain the experimental findings, but right now, we can only afford geometry optimizations due to system size.

Chapter 8

Conclusion and Outlook

All the work reported in this thesis is in close collaboration with experimentalists. Theoretical simulations are intent to help better interprete the experimental findings, as less is known from the experimental STM images, especially for the water clusters. Our work shows that the most spotted triple protrusion images formed in the pore of the nanomesh in experiment are most probably cyclic water hexamers. As from our simulated STM calculations, the STM tip picks the density of the lone pair of the O atoms in each water molecule. Thus when the dangling H atom points to the vacuum, the density of the lone pairs is hidden underneath. In this case, the water molecules become invisible to the STM tips, which explains the triple protrusion pattern at a distance close to the second neighbor distance in ice. Although we still could not explain the chirality of water hexamer observed in the experiment, a molecular dynamics run might help to explain which we cannot afford right now due to the expensive computational cost and slow convergence caused by the metal slab. There might also be other water molecules externally attached to the hexamer or moving on the wire, which is not spotted by the STM imaging, but could distort the water hexamer.

When larger amount of water is deposited to the bare nanomesh, the nano-ice clusters are observed in all the pores of the nanomesh. Different nano-ice models based on water lattice and also the rotation angle with respect to the substrate are proposed. The calculations are first performed on a flat BN layer in order to reduce the computational cost. Because the binding between the water cluster and the BN layer is much weaker compared to the water cluster themselves, the binding energies for different models didn't give much hint on which is the most favored model due to the small difference in energy. But the most probable structure is proposed considering to minimize the dipole moment distribution, which has a mirror symmetry in xy plane. After that, 38 water molecules are extracted from such model to fill

the entire nanomesh pore. Although the water molecules on the edge have more freedom to rotate during the geometry optimization due to less H-bond constrain, the simulated STM image is consistent with the experimental one.

The last part of the work involves understanding why the [21] off-center adsorption site is the most favorable for H_2Pc and CuPc adsorbed on nanomesh. But in this case, the most favored adsorption site according to the DFT calculations is when the molecule is right in the center of the pore, and certain [21] off-center adsorption sites show very close adsorption energies compared to the center site, less than 0.1 eV, which could be within the limit of the method accuracy. The binding energies also indicate that for such kind of weak interaction systems, the vdW dispersion correction is of extreme importance, as all the attractive contribution comes from the dispersion correction, while the pure DFT calculations only give repulsive results. The dispersion correction scheme employed here is the popular Grimme's D3 dispersion correction, although it is shown that it works well with some typical weak interaction systems, still less is known for the large scale metallic systems, especially considering that all the pairwise contributions are included. Our simplified model based only on the vdW correction and the electrostatic interaction indicates that the rim is the most possible adsorption site for H_2Pc. However, it didn't give any specific adsorption direction and when adsorbed on the rim, the molecule tends to be distorted in order to adapt the corrugation in the substrate, while we only employ the structure of H_2Pc from gas phase in this model.

The next step of this work would involve the *ab initio* molecular dynamics simulations, as still much is unknown about the system, like the chirality of the water hexamer, the nucleation of the nano-ice cluster, why the nano-ice is only observed in the pore, and the adsorption site of H_2Pc and CuPc. The only way to perform molecular dynamics simulations would require to largely reduce the computational cost by the metal slab, while the polarization effect of the metal slab still exists, which is attributed to the lower electrostatic potential above the pore rather than the wire. The approach we are going to employ would be a multi-scale one: using the electrostatic potential of the bare nanomesh and the rest part except for the nanomesh will be treated with DFT.

Bibliography

[1] S. Iijima. Helical microtubules of graphitic carbon. *Nature*, 354(6348):56–58, 1991.

[2] T. W. Ebbesen and P. M. Ajayan. Large-scale synthesis of carbon nanotubes. *Nature*, 358(6383):220–222, 1992.

[3] D. S. Bethune, C. H. Kiang, M. S. De Vries, G. Gorman, R. Savoy, J. Vazquez, and R. Beyers. Cobalt-catalysed growth of carbon nanotubes with single-atomic-layer walls. *Nature*, 363(6430):605–607, 1993.

[4] S. Iijima and T. Ichihashi. Single-shell carbon nanotubes of 1-nm diameter. *Nature*, 363(6430):603–605, 1993.

[5] H. W. Kroto, J. R. Heath, S. C. O'brien, R. F. Curl, and R. E. Smalley. C_{60}: Buckminsterfullerene. *Nature*, 318(6042):162–163, 1985.

[6] N. G. Chopra, R. J. Luyken, K. Cherrey, V. H. Crespi, M. L. Cohen, S. G. Louie, and A. Zettl. Boron-nitride nanotubes. *Science*, 269(5226):966–967, 1995.

[7] E. Bengu and L. D. Marks. Single-walled BN nanostructures. *Phys. Rev. Lett.*, 86(11):2385–2387, 2001.

[8] F. Banhart, M. Zwanger, and H. J. Muhr. The formation of curled concentric-shell clusters in boron nitride under electron irradiation. *Chem. Phys. Lett.*, 231(1):98–104, 1994.

[9] A. Nagashima, N. Tejima, Y. Gamou, T. Kawai, and C. Oshima. Electronic dispersion relations of monolayer hexagonal boron nitride formed on the Ni(111) surface. *Phys. Rev. B*, 51(7):4606–4613, 1995.

[10] A. B. Preobrajenski, A. S. Vinogradov, and N. Mårtensson. Monolayer of h-BN chemisorbed on Cu(111) and Ni(111): The role of the transition metal 3d states. *Surf. Sci.*, 582(1-3):21–30, 2005.

[11] M. Corso, W. Auwärter, M. Muntwiler, A. Tamai, T. Greber, and J. Osterwalder. Boron nitride nanomesh. *Science*, 303(5655):217–220, 2004.

[12] A. B. Preobrajenski, A. S. Vinogradov, M. L. Ng, E. Ćavar, R. Westerström, A. Mikkelsen, E. Lundgren, and N. Mårtensson. Influence of chemical interaction at the lattice-mismatched h-BN/Rh(111) and h-BN/Pt(111) interfaces on the overlayer morphology. *Phys. Rev. B*, 75(24):245412, 2007.

[13] A. B. Preobrajenski, M. A. Nesterov, M. L. Ng, A. S. Vinogradov, and N. Mårtensson. Monolayer h-BN on lattice-mismatched metal surfaces: On the formation of the nanomesh. *Chem. Phys. Lett.*, 446(1-3):119–123, 2007.

[14] A. B. Preobrajenski, S. A. Krasnikov, A. S. Vinogradov, M. L. Ng, T. Käämbre, A. A. Cafolla, and N. Mårtensson. Adsorption-induced gap states of h-BN on metal surfaces. *Phys. Rev. B*, 77(8):085421, 2008.

[15] F. Müller, S. Hüfner, H. Sachdev, R. Laskowski, P. Blaha, and K. Schwarz. Epitaxial growth of hexagonal boron nitride on Ag(111). *Phys. Rev. B*, 82(11), 2010.

[16] D. Martoccia, S. A. Pauli, T. Brugger, T. Greber, B. D. Patterson, and P. R. Willmott. *h*-BN on Rh(111): Persistence of a commensurate 13-on-12 superstructure up to high temperatures. *Surf. Sci.*, 604(5-6):L9–L11, 2010.

[17] D. Martoccia, T. Brugger, M. Björck, C. M. Schlepütz, S. A. Pauli, T. Greber, B. D. Patterson, and P. R. Willmott. *h*-BN/Ru(0001) nanomesh: A 14-on-13 superstructure with 3.5 nm periodicity. *Surf. Sci.*, 604(5-6):L16–L19, 2010.

[18] N. A. Vinogradov, A. A. Zakharov, M. L. Ng, A. Mikkelsen, E. Lundgren, N. Mårtensson, and A. B. Preobrajenski. One-dimensional corrugation of the *h*-BN monolayer on Fe(110). *Langmuir*, 28(3):1775–1781, 2012.

[19] Y. Ding, M. Iannuzzi, and J. Hutter. Investigation of boron nitride nanomesh interacting with water. *J. Phys. Chem. C*, 115(28):13685–13692, 2011.

[20] S. Berner, M. Corso, R. Widmer, O. Groening, R. Laskowski, P. Blaha, K. Schwarz, A. Goriachko, H. Over, S. Gsell, M. Schreck, H. Sachdev, T. Greber, and J. Osterwalder. Boron nitride nanomesh: Functionality

from a corrugated monolayer. *Angew. Chem. Int. Ed.*, 46(27):5115–5119, 2007.

[21] H. F. Ma, T. Brugger, S. Berner, Y. Ding, M. Iannuzzi, J. Hutter, J. Osterwalder, and T. Greber. Nano-ice on boron nitride nanomesh: Accessing proton disorder. *ChemPhysChem*, 11(2):399–403, 2010.

[22] H. F. Ma, Y. Ding, M. Iannuzzi, T. Brugger, S. Berner, J. Hutter, J. Osterwalder, and T. Greber. Chiral distortions of confined ice hexamers. Submitted.

[23] O. Gröning, R. Wimder, and T. Dienel. Private Communication.

[24] Y. Ding, M. Iannuzzi, and J. Hutter. Investigation of *h*-BN/Rh(111) nanomesh interacting with water and atomic hydrogen. *Chimia*, 65(4):256–259, 2011.

[25] M. Morscher, M. Corso, T. Greber, and J. Osterwalder. Formation of single layer h-BN on Pd(111). *Surf. Sci.*, 600(16):3280–3284, 2006.

[26] M. Corso, T. Greber, and J. Osterwalder. *h*-BN on Pd(110): a tunable system for self-assembled nanostructures? *Surf. Sci.*, 577(2-3):L78–L84, 2005.

[27] E. Rokuta, Y. Hasegawa, K. Suzuki, Y. Gamou, C. Oshima, and A. Nagashima. Phonon dispersion of an epitaxial monolayer film of hexagonal boron nitride on Ni(111). *Phys. Rev. Lett.*, 79(23):4609–4612, 1997.

[28] A. Goriachko, Y. B. He, M. Knapp, H. Over, M. Corso, T. Brugger, S. Berner, J. Osterwalder, and T. Greber. Self-assembly of a hexagonal boron nitride nanomesh on Ru(0001). *Langmuir*, 23(6):2928–2931, 2007.

[29] R. Laskowski, P. Blaha, T. Gallauner, and K. Schwarz. Single-layer model of the hexagonal boron nitride nanomesh on the Rh(111) surface. *Phys. Rev. Lett.*, 98(10):106802, 2007.

[30] R. Laskowski and P. Blaha. Unraveling the structure of the h-BN/Rh(111) nanomesh with *ab initio* calculations. *J. Phys.: Condens. Matter*, 20(6):064207, 2008.

[31] G. B. Grad, P. Blaha, K. Schwarz, W. Auwärter, and T. Greber. Density functional theory investigation of the geometric and spintronic structure of *h*-BN/Ni(111) in view of photoemission and STM experiments. *Phys. Rev. B*, 68(8):085404, 2003.

[32] O. Bunk, M. Corso, D. Martoccia, R. Herger, P. R. Willmott, B. D. Patterson, J. Osterwalder, J. F. van der Veen, and T. Greber. Surface X-ray diffraction study of boron-nitride nanomesh in air. *Surf. Sci.*, 601(2):L7–L10, 2007.

[33] R. Widmer, S. Berner, O. Gröning, T. Brugger, J. Osterwalder, and T. Greber. Electrolytic in situ STM investigation of h-BN-nanomesh. *Electrochem. Commun.*, 9(10):2484–2488, 2007.

[34] H. Dil, J. Lobo-Checa, R. Laskowski, P. Blaha, S. Berner, J. Osterwalder, and T. Greber. Surface trapping of atoms and molecules with dipole rings. *Science*, 319(5871):1824–1826, 2008.

[35] G. A. Kimmel, J. Matthiesen, M. Baer, C. J. Mundy, N. G. Petrik, R. S. Smith, Z. Dohnalek, and B. D. Kay. No confinement needed: Observation of a metastable hydrophobic wetting two-layer ice on graphene. *J. Am. Chem. Soc.*, 131(35):12838–12844, 2009.

[36] S. H. Chang, S. Kuck, J. Brede, L. Lichtenstein, G. Hoffmann, and R. Wiesendanger. Symmetry reduction of metal phthalocyanines on metals. *Phys. Rev. B*, 78(23):233409, 2008.

[37] B. W. Heinrich, C. Iacovita, T. Brumme, D. J. Choi, L. Limot, M. V. Rastei, W. A. Hofer, J. Kortus, and J. P. Bucher. Direct observation of the tunneling channels of a chemisorbed molecule. *J. Phys. Chem. Lett.*, 1(10):1517–1523, 2010.

[38] A. Sperl, J. Kröger, and R. Berndt. Controlled metalation of a single adsorbed phthalocyanine. *Angew. Chem. Int. Ed.*, 50(23):5294–5297, 2011.

[39] R. Cuadrado, J. I. Cerdá, Y. F. Wang, G. Xin, R. Berndt, and H. Tang. CoPc adsorption on Cu(111): Origin of the C4 to C2 symmetry reduction. *J. Chem. Phys.*, 133(15):154701, 2010.

[40] P. Hohenberg and W. Kohn. Inhomogeneous electron gas. *Phys. Rev.*, 136(3B):B864–B871, 1964.

[41] W. Kohn and L. J. Sham. Self-consistent equations including exchange and correlation effects. *Phys. Rev.*, 140(4A):A1133–A1138, 1965.

[42] A. D. Becke. Density-functional exchange-energy approximation with correct asymptotic behavior. *Phys. Rev. A*, 38(6):3098–3100, 1988.

[43] J. P. Perdew, K. Burke, and M. Ernzerhof. Generalized gradient approximation made simple. *Phys. Rev. Lett.*, 77(18):3865–3868, 1996.

[44] Y. K. Zhang and W. T. Yang. Comment on "generalized gradient approximation made simple". *Phys. Rev. Lett.*, 80(4):890–890, 1998.

[45] Y. Andersson, D. C. Langreth, and B. I. Lundqvist. van der waals interactions in density-functional theory. *Phys. Rev. Lett.*, 76(1):102–105, 1996.

[46] M. Dion, H. Rydberg, E. Schröder, D. C. Langreth, and B. I. Lundqvist. Van der waals density functional for general geometries. *Phys. Rev. Lett.*, 92(24):246401, 2004.

[47] D. C. Langreth, B. I. Lundqvist, S. D. Chakarova-Käck, V. R. Cooper, M. Dion, P. Hyldgaard, A. Kelkkanen, J. Kleis, L. Z. Kong, S. Li, P. G. Moses, E. Murray, A. Puzder, H. Rydberg, E. Schröder, and T. Thonhauser. A density functional for sparse matter. *J. Phys.: Condens. Matter*, 21(8):084203, 2009.

[48] S. Grimme. Semiempirical GGA-type density functional constructed with a long-range dispersion correction. *J. Comput. Chem.*, 27(15):1787–1799, 2006.

[49] S. Grimme, J. Antony, S. Ehrlich, and H. Krieg. A consistent and accurate *ab initio* parametrization of density functional dispersion correction (DFT-D) for the 94 elements H-Pu. *J. Chem. Phys.*, 132(15):154104, 2010.

[50] P. Jurečka, J. Šponer, J. Černý, and P. Hobza. Benchmark database of accurate (MP2 and CCSD(T) complete basis set limit) interaction energies of small model complexes, DNA base pairs, and amino acid pairs. *Phys. Chem. Chem. Phys.*, 8(17):1985–1993, 2006.

[51] P. Jurečka, J. Černý, P. Hobza, and D. R. Salahub. Density functional theory augmented with an empirical dispersion term. Interaction energies and geometries of 80 noncovalent complexes compared with *ab initio* quantum mechanics calculations. *J. Comput. Chem.*, 28(2):555–569, 2007.

[52] G. Binnig and H. Rohrer. Scanning tunneling microscopy. *IBM J. Res. Dev.*, 30(4):355–369, 1986.

[53] J. Tersoff and D. R. Hamann. Theory and application for the scanning tunneling microscope. *Phys. Rev. Lett.*, 50(25):1998–2001, 1983.

[54] J. Tersoff and D. R. Hamann. Theory of the scanning tunneling microscope. *Phys. Rev. B*, 31(2):805–813, 1985.

[55] N. Marzari and D. Vanderbilt. Maximally localized generalized Wannier functions for composite energy bands. *Phys. Rev. B*, 56(20):12847–12865, 1997.

[56] N. Pugliano and R. J. Saykally. Measurement of quantum tunneling between chiral isomers of the cyclic water trimer. *Science*, 257(5078):1937–1940, 1992.

[57] K. Liu, J. D. Cruzan, and R. J. Saykally. Water clusters. *Science*, 271(5251):929–933, 1996.

[58] K. Liu, M. G. Brown, J. D. Cruzan, and R. J. Saykally. Vibration-rotation tunneling spectra of the water pentamer: Structure and dynamics. *Science*, 271(5245):62–64, 1996.

[59] K. Liu, M. G. Brown, C. Carter, R. J. Saykally, J. K. Gregory, and D. C. Clary. Characterization of a cage form of the water hexamer. *Nature*, 381(6582):501–503, 1996.

[60] K. Liu, J. G. Loeser, M. J. Elrod, B. C. Host, J. A. Rzepiela, N. Pugliano, and R. J. Saykally. Dynamics of structural rearrangements in the water trimer. *J. Am. Chem. Soc.*, 116(8):3507–3512, 1994.

[61] F. N. Keutsch and R. J. Saykally. Water clusters: Untangling the mysteries of the liquid, one molecule at a time. *Proc. Natl. Acad. Sci. USA*, 98(19):10533–10540, 2001.

[62] N. Goldman, C. Leforestier, and R. J. Saykally. Water dimers in the atmosphere II: Results from the VRT(ASP-W)III potential surface. *J. Phys. Chem. A*, 108(5):787–794, 2004.

[63] J. D. Cruzan, M. R. Viant, M. G. Brown, and R. J. Saykally. Terahertz laser vibration-rotation tunneling spectroscopy of the water tetramer. *J. Phys. Chem. A*, 101(48):9022–9031, 1997.

[64] J. D. Cruzan, L. B. Braly, K. Liu, M. G. Brown, J. G. Loeser, and R. J. Saykally. Quantifying hydrogen bond cooperativity in water: VRT spectroscopy of the water tetramer. *Science*, 271(5245):59–62, 1996.

[65] S. S. Xantheas and T. H. Dunning. *Ab Initio* studies of cyclic water clusters $(H_2O)_n$, n=1-6. I. Optimal structures and vibrational-spectra. *J. Chem. Phys.*, 99(11):8774–8792, 1993.

[66] S. S. Xantheas. *Ab Initio* studies of cyclic water clusters $(H_2O)_n$, n=1-6. II. Analysis of many-body interactions. *J. Chem. Phys.*, 100(10):7523–7534, 1994.

[67] D. A. Estrin, L. Paglieri, G. Corongiu, and E. Clementi. Small clusters of water molecules using density functional theory. *J. Phys. Chem.*, 100(21):8701–8711, 1996.

[68] D. J. Wales and T. R. Walsh. Theoretical study of the water pentamer. *J. Chem. Phys.*, 105(16):6957–6971, 1996.

[69] I. M. B. Nielsen, E. T. Seidl, and C. L. Janssen. Accurate structures and binding energies for small water clusters: The water trimer. *J. Chem. Phys.*, 110(19):9435–9442, 1999.

[70] S. S. Xantheas. Cooperativity and hydrogen bonding network in water clusters. *Chem. Phys.*, 258(2-3):225–231, 2000.

[71] S. S. Xantheas, C. J. Burnham, and R. J. Harrison. Development of transferable interaction models for water. II. Accurate energetics of the first few water clusters from first principles. *J. Chem. Phys.*, 116(4):1493–1499, 2002.

[72] E. E. Dahlke, R. M. Olson, H. R. Leverentz, and D. G. Truhlar. Assessment of the accuracy of density functionals for prediction of relative energies and geometries of low-lying isomers of water hexamers. *J. Phys. Chem. A*, 112(17):3976–3984, 2008.

[73] J. F. Pérez, C. Z. Hadad, and A. Restrepo. Structural studies of the water tetramer. *Int. J. Quantum Chem.*, 108(10):1653–1659, 2008.

[74] D. M. Bates and G. S. Tschumper. CCSD(T) complete basis set limit relative energies for low-lying water hexamer structures. *J. Phys. Chem. A*, 113(15):3555–3559, 2009.

[75] CP2K version 2.2.426 (Release Version), the CP2K developers group (2012). CP2K is freely available from http://www.cp2k.org.

[76] G. Lippert, J. Hutter, and M. Parrinello. A hybrid Gaussian and plane wave density functional scheme. *Mol. Phys.*, 92(3):477–487, 1997.

[77] S. Goedecker, M. Teter, and J. Hutter. Separable dual-space Gaussian pseudopotentials. *Phys. Rev. B*, 54(3):1703–1710, 1996.

[78] C. Hartwigsen, S. Goedecker, and J. Hutter. Relativistic separable dual-space Gaussian pseudopotentials from H to Rn. *Phys. Rev. B*, 58(7):3641–3662, 1998.

[79] M. Krack. Pseudopotentials for H to Kr optimized for gradient-corrected exchange-correlation functionals. *Theor. Chem. Acc.*, 114(1-3):145–152, 2005.

[80] J. VandeVondele and J. Hutter. Gaussian basis sets for accurate calculations on molecular systems in gas and condensed phases. *J. Chem. Phys.*, 127(11):114105, 2007.

[81] C. G. Broyden. The convergence of single-rank quasi-Newton methods. *Math. Comput.*, 24(110):365–382, 1970.

[82] R. Fletcher. A new approach to variable metric algorithms. *Comput. J.*, 13(3):317–322, 1970.

[83] D. Goldfarb. A family of variable-metric methods derived by variational means. *Math. Comput.*, 24(109):23–26, 1970.

[84] D. F. Shanno. Conditioning of quasi-Newton methods for function minimization. *Math. Comput.*, 24(111):647–656, 1970.

[85] J. VandeVondele and J. Hutter. An efficient orbital transformation method for electronic structure calculations. *J. Chem. Phys.*, 118(10):4365–4369, 2003.

[86] P. Pulay. Convergence acceleration of iterative sequences. the case of scf iteration. *Chem. Phys. Lett.*, 73(2):393–398, 1980.

[87] R. Laskowski and P. Blaha. *Ab initio* study of h-BN nanomeshes on Ru(001), Rh(111), and Pt(111). *Phys. Rev. B*, 81(7):075418, 2010.

[88] S. F. Boys and F. Bernardi. The calculation of small molecular interactions by differences of separate total energies. Some procedures with reduced errors. *Mol. Phys.*, 19(4):553–566, 1970.